平成 27 年度－平成 28 年度

光コムレーザによる 3 次元絶対位置測定報告書

平成 29 年 3 月 31 日

東京大学大学院工学系研究科

精密工学専攻

高増研究室

目　　次

1. 光コムレーザによる長さ測定の原理	1
1.1　光コム（光周波数コム）による長さの定義	1
1.2　光コムのパルス干渉による絶対距離計測	3
2. 光コムレーザによる長さ測定手法の実験的検証	8
2.1　光コムレーザによるパルス干渉技術の確立および装置仕様の決定	8
2.2　ボールレンズをターゲットとしたパルス干渉法	9
2.3　光コムレーザ用光ファイバー干渉測定システムの試作	11
2.4　光コムレーザ用光ファイバー干渉測定システムの基礎的評価	13
3. 光コムレーザの三次元測定機の精度評価への適用	16
3.1　三次元測定機の受入検査	16
3.2　三次元測定機の精度評価用パルス干渉計	19
4. マルチビームオートコリメータシステムの試作および基本動作確認	22
5. まとめ	23
6. 関連論文リスト（平成 27 年度および平成 28 年度発表分）	24
6.1　雑誌論文	25
6.2　国際会議発表	27
関連雑誌論文を添付	29

光コムレーザによる３次元絶対位置測定報告書

1. 光コムレーザによる長さ測定の原理

1.1　光コム（光周波数コム）による長さの定義

三次元空間内で，絶対的な距離を測定する手法としては多くの方法が使われている．その中で，光コムを利用した方法および三次元測定機の検査への応用について説明する．長さの定義は，「1秒の 299 792 458分の1の時間に光が真空中を伝わる行程の長さ」となっている．これは，真空中の光の速度を定数として，時間によって長さを定義する方法である．この方法では，時間の測定精度が物理量の中で最も優れていることを利用することで，長さも時間と同じ精度で定義が行えることになっている．しかし，実際の長さを測定する場合には，適当な物差しが必要で，物差しとしてはレーザの波長が使われている．日本では2009年までは，「よう素安定化ヘリウム・ネオンレーザの真空中での波長（632.9908 nm）」が，トレーサビリティの最上位である国家標準（特定標準器）として使われていた．

光コム（光周波数コム：optical frequency comb）は，フェムト秒のパルス幅を持つパルスレーザで，パルスの繰り返し周波数は時間標準に同期されている．図1-1 (a) は，100 MHzの繰り返し周波数 f_{rep} を 持つ光コムレーザ波形の時間領域での模式図で，パルス幅は150 fs（長さで45 μm），パルスの繰り返し間隔は10 ns（長さで3 m）となっている．図1-1 (b) に，パルスレーザの周波数領域でのパワースペクトラムを示す．繰り返し周波数に相当する間隔で，スペクトラムが櫛の歯状（Comb状）に生じている．この周波数は，時間標準に同期されているため，非常に高精度である．また，よう素安定化ヘリウム・ネオンレーザは，特定の波長しか校正できなかったことなどにより，2009年から長さの特定標準器は，「協定世界時に同期した光周波数コム装置」に変更された．この変更により，長さの基準が300倍高精度化された．

光コムは，長さの定義としてだけでなく，直接的に長さの絶対計測に利用することができる．光コムを利用した絶対計測は，直接的にトレーサビリティを確保することができ，標準としても優れている．これまでにも，パルスレーザの特性を生かした絶対計測の研究が行われている．3 mのパルス間隔を持つ光コムを利用して，400 mの非常に長い距離を10 μm程度の精度で絶対測定を行っている例がある．この章では，光コムを利用したパルス干渉計の原理を説明する．

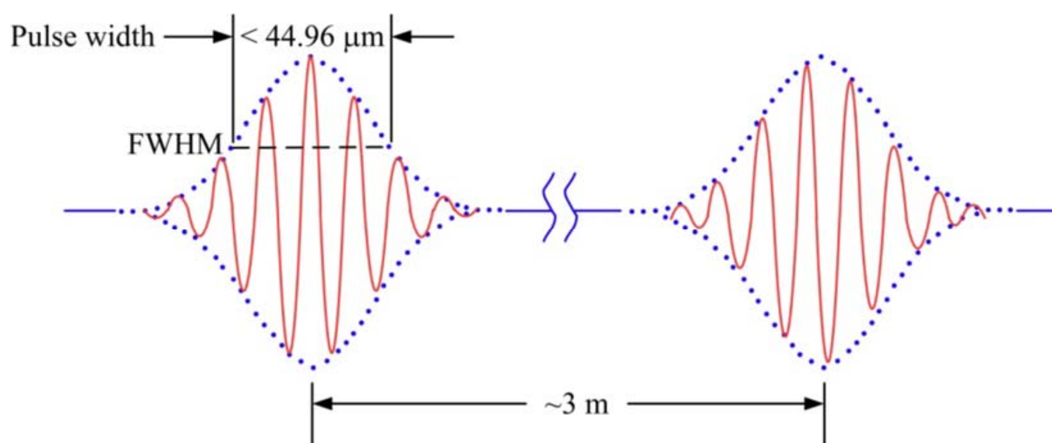

(a) 時間領域のパルス波形

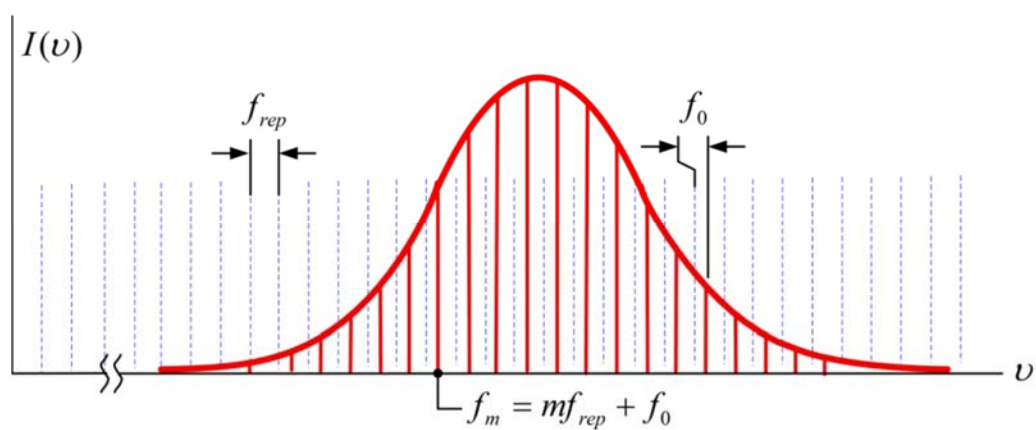

(b) 周波数領域の櫛の歯状のパワースペクトラム

図1-1　光コムレーザのパルス波形およびパワースペクトラム

1.2　光コムのパルス干渉による絶対距離計測

（1）パルス干渉計の原理

光コムを利用したパルス干渉計では，パルスが干渉することにより干渉縞が生じる．白色干渉では，参照ミラーと測定対象までの光路長が等しい場合のみ干渉縞が生じるが，パルス干渉ではパルス間隔の整数倍だけ光路長がずれた場合にも干渉縞が生じる．図1-2 (a) に，光コムによるパルス干渉の原理を示す．参照ミラーM1と測定対象M2までの距離の差が，パルス間隔の半分の整数倍の時に干渉縞が観察できる．測定対象として基準位置にハーフミラーM0を設置し，参照ミラーM1を走査すると，図1-2 (b) のようにM0からの干渉縞とM1からの干渉縞を観察できる．

図1-2 (b) の横軸はM1の走査における時間であるが，走査速度から2つの干渉縞の距離ΔLを求めることができる．基準位置M0と測定対象M2の絶対距離Lは，式(1)で計算することができる．ここで，mはパルス間隔の整数倍を表す整数で，l_d はパルス間隔である．パルス間隔は，繰り返し周波数 f_{rep}，光速c および空気の屈折率n を利用して式(2)で計算される．例えば繰り返し周波数が100 MHzの場合，パルス間隔は約3 mとなるため約1.5 mの整数倍の距離の差で干渉波形を得ることになる．小型の三次元測定機や工作機械などの精度評価に適用する場合には，このパルス間隔は長すぎるため，パルス間隔を短くすることが必要になる．

$$L = \frac{ml_d}{2} + \Delta L \tag{1}$$

$$l_d = \frac{c}{nf_{\mathrm{rep}}} \tag{2}$$

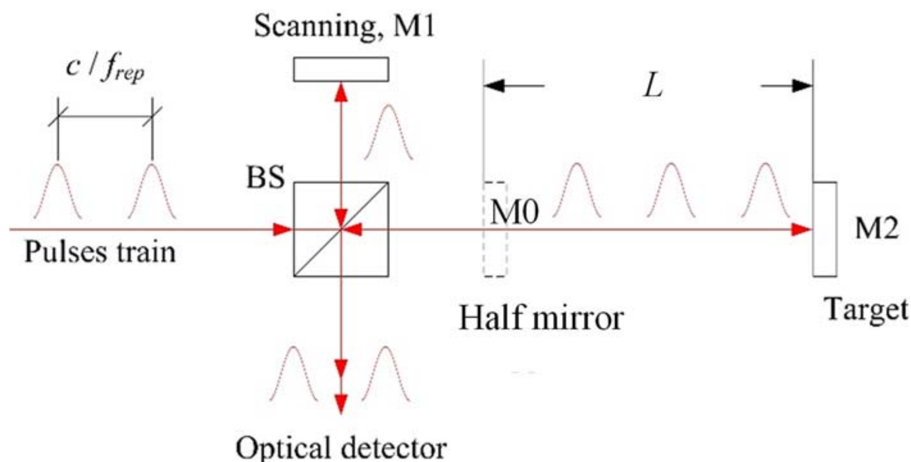

(a) パルス干渉計の基本構成

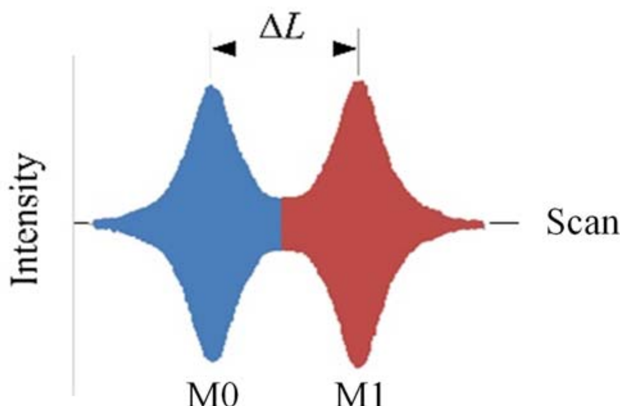

(b) M0およびM1から得られる干渉信号

図1-2　光コムによるパルス干渉計の原理

（2）エタロンによるパルス間隔の短縮

光コムのパルス間隔を，エタロンを利用して短くする方法を説明する．まず，図1-3 (a) に2つのミラーを間隔l で設置したエタロンの模式図を示した．エタロンの間隔l, 光速c およびエタロン内の屈折率n により決定される特定の周波数だけが，エタロンを透過する．図1-3 (b) は，オプティカルファイバーの両面にコーティングをすることで作ったファイバーエタロンである．一般的なミラーエタロンは，調整が難しく安定性に問題がある．一方，ファイバーエタロンは，簡単に利用でき調整が不要である．

エタロンを透過する周波数が，光コムのf_{rep} の整数倍（k倍）の間隔となっているとき，光周波数コムレーザがエタロンを通過すると，周波数スペクトラムは図1-4 (a) のように特定の周波数だけが透過することになる．この関係を，時間領域で見ると，図1-4 (b) のようにパルス間隔がk 分の1に短くなる．このように，エタロンを利用して光コムのパルス間隔を短くすることができる．

今回の実験では，ファイバーエタロンを利用してパルス間隔が短くするシステムを構築した．100 MHzの繰り返し周波数を持つ光コムから，ファイバーエタロンにより1 GHzの繰り返し周波数だけを透過することができた（$k = 10$）．結果として，パルス間隔が300 mmとなり，150 mmの整数倍の位置で干渉信号が得られるパルス干渉計が構成でき，小型の三次元測定機などへの適用が可能となった．図1-5に試作したファイバーエタロンとその特性評価（スペクトラム）を示す．

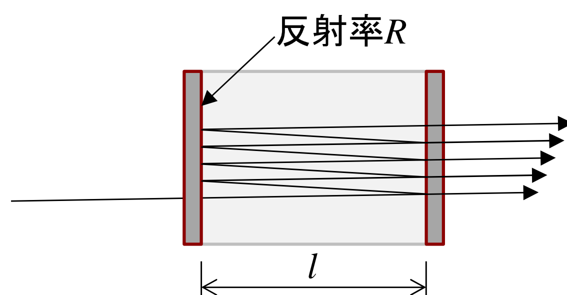

(a) エタロンの原理

(b) ファイバーエタロンの例

図1-3　エタロンの原理とファイバーエタロン

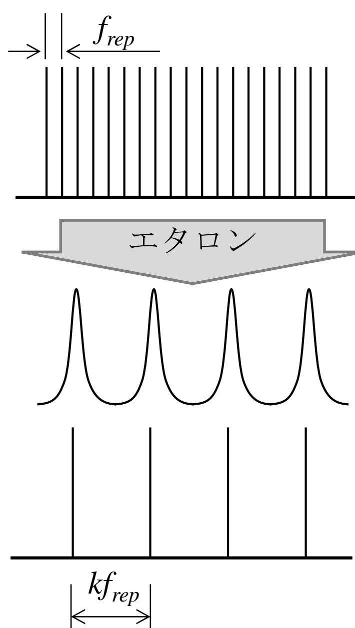

(a) 周波数領域

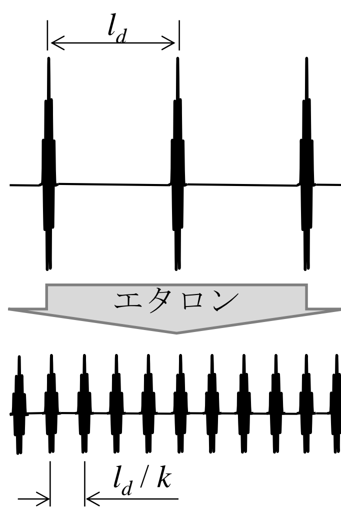

(b) 時間領域

図1-4　光周波数コムレーザがエタロンを透過した場合

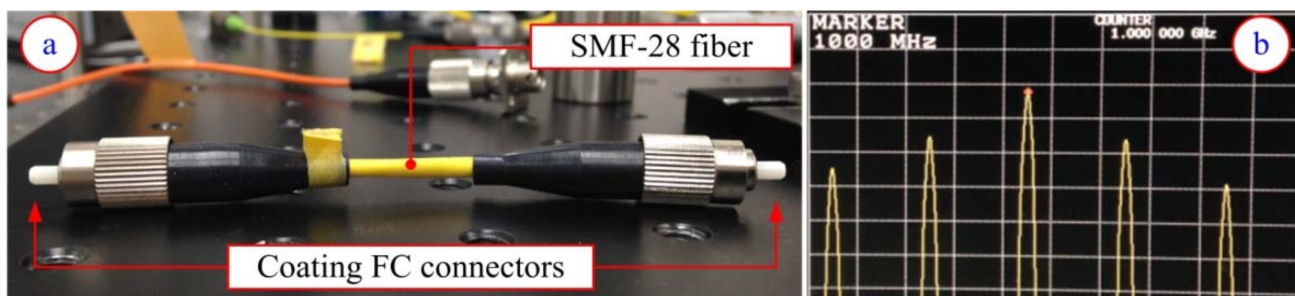

図1-5　試作したファイバーエタロンとその特性評価

2. 光コムレーザによる長さ測定手法の実験的検証

2.1 光コムレーザによるパルス干渉技術の確立および装置仕様の決定

光コムレーザによるパルス干渉技術について，基礎的な実験を行った．実験は，図2-1の写真に示すように光学素子を個別に並べることで実施した．この基礎実験によって，開発する装置仕様を決定することができた．

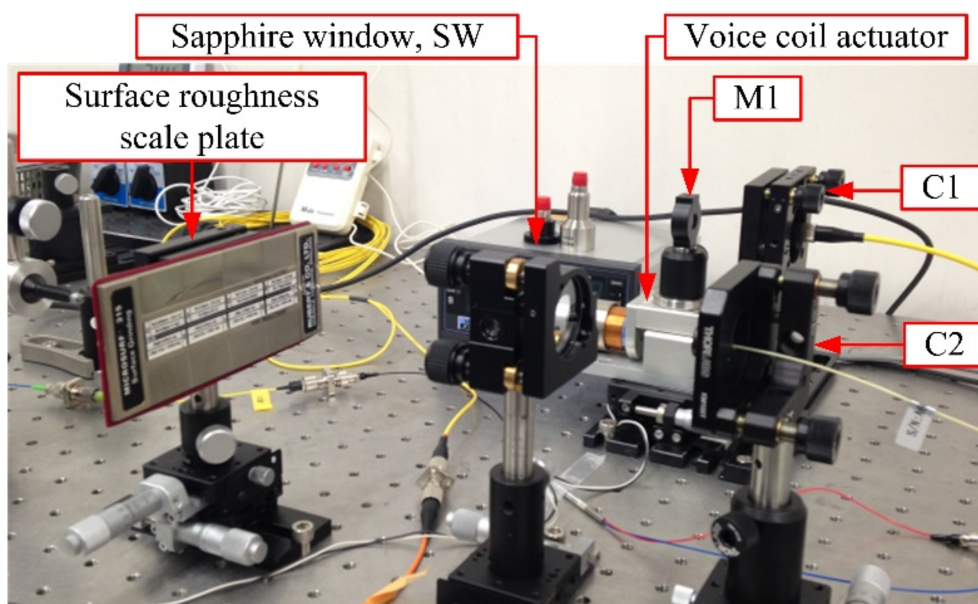

図2-1 光コムレーザによるパルス干渉技術の基礎的な実験

2.2　ボールレンズをターゲットとしたパルス干渉法

図2-2は，ボールレンズとコーナーキューブの反射の特性を示している．屈折率が2.0のボールレンズは，どの方向からの光を反射できるため，干渉計のアライメントが容易になる．実験では，10 mの距離で十分な干渉信号が取得できている．

基礎実験では，まず，鏡面，コーナーキューブプリズム，平面などをターゲットとして実験を行った．次に，図2-3は，前章の原理を利用した光コムパルス干渉計のターゲットを，ボールレンズとした場合の干渉計である．光コムの信号は，ファイバーエタロンによって1 GHzの繰り返しパルスとなり，パルス干渉計へ入力される．パルス干渉計では，まず光信号を2つに分岐する．1つの信号は，コリメータを通して三次元測定機のプロービングシステムの位置に設置されたボールレンズにより反射される．もう一つの光信号は，コリメータからボイスコイルステージに設置されたミラーで反射され，この2つの信号が干渉する．この場合は，2つの光信号の距離の差が150 mmの整数倍になった場合に光信号が得られる．

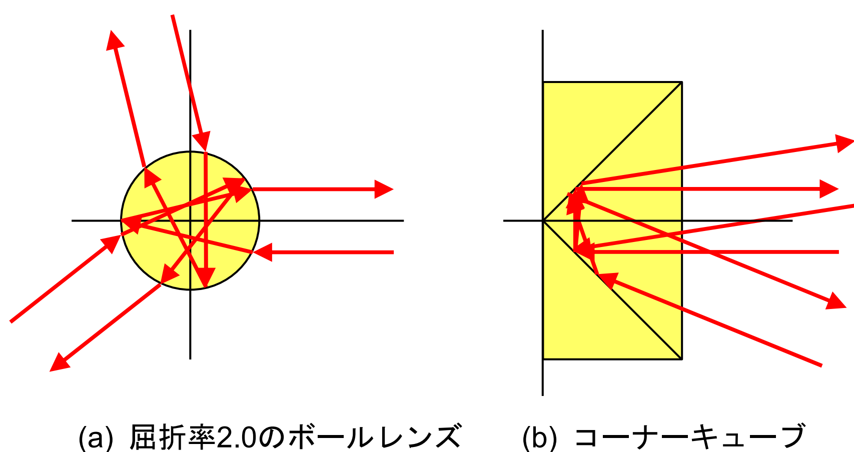

(a) 屈折率2.0のボールレンズ　　(b) コーナーキューブ

図2-2　ボールレンズとコーナーキューブ：ボールレンズはどの方向からの光も反射できる

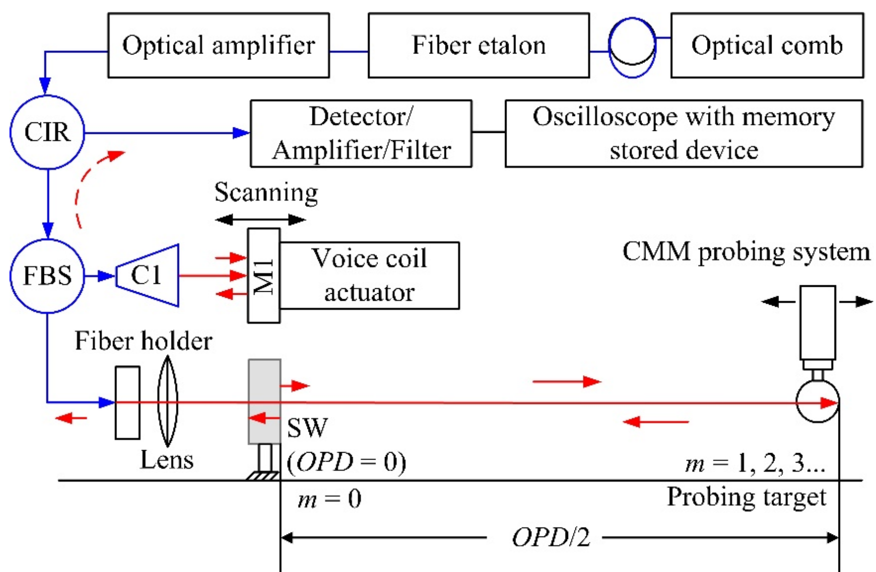

図2-3　ボールレンズをターゲットとした光コムレーザ用測定システム

2.3　光コムレーザ用光ファイバー干渉測定システムの試作

図2-4は，基礎実験によって決定した仕様に基づき，開発する光コムレーザ用ファイバー干渉測定システムの構成図である．この図の上の部分の干渉システム部分について，試作を行った．図2-5に製作した干渉計を示す．

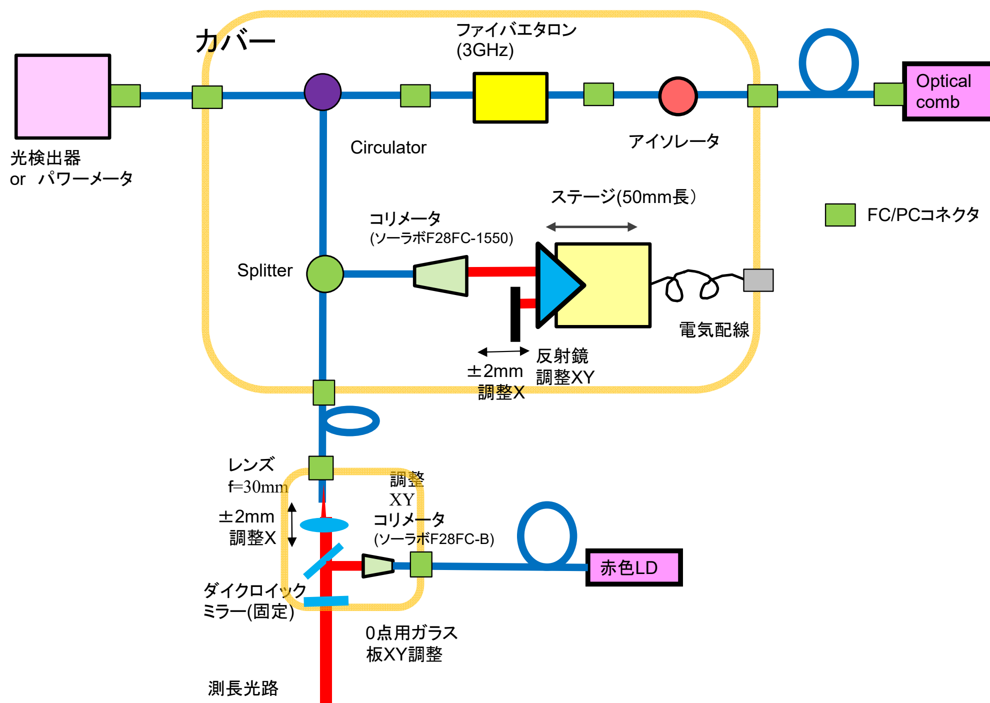

図2-4　光コムレーザ用ファイバー干渉測定システムの構成図

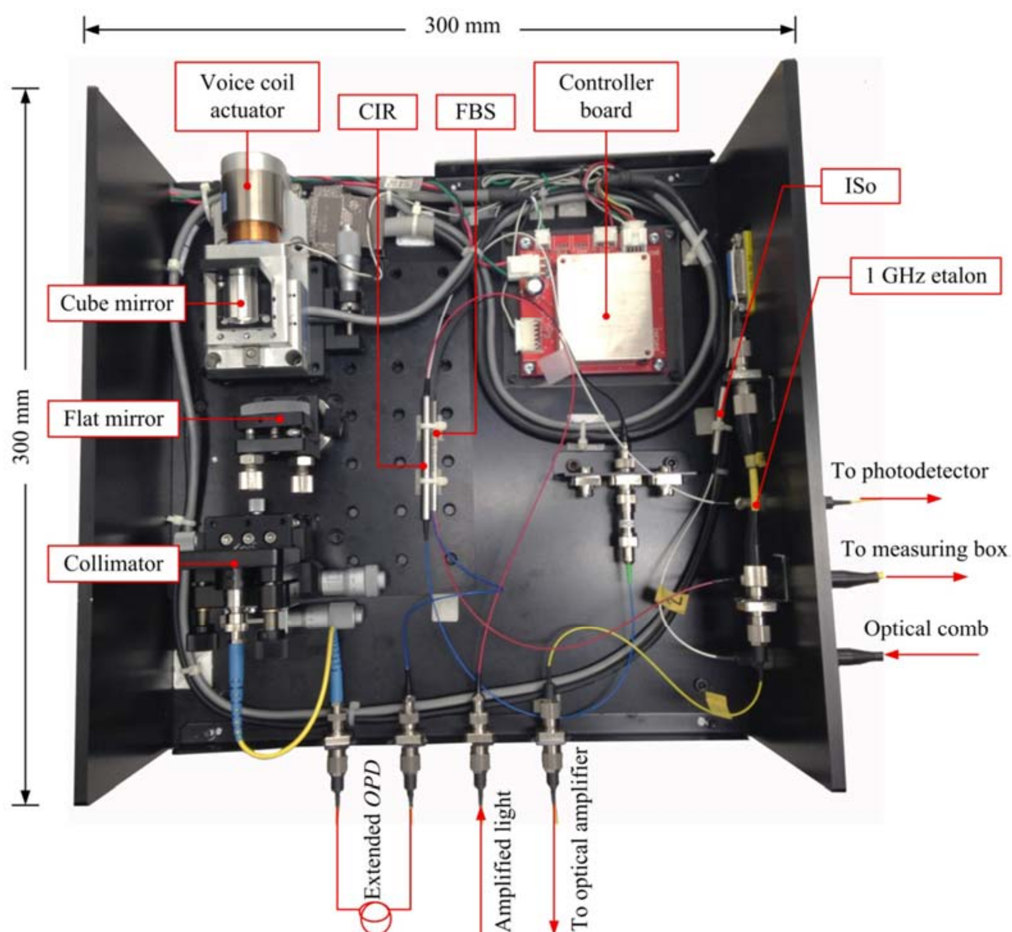

図2-5　製作した光コムレーザ用ファイバー干渉測定システム

2.4　光コムレーザ用光ファイバー干渉測定システムの基礎的評価

図2-5は，開発したデータ処理システムである．パルス干渉計の干渉縞から絶対距離を自動検出するために，ソフトウェアを開発した．このシステムでは，A/D変換した干渉縞の信号の絶対値を取り，その後ローパスフィルターを通した後に，微分することでピークを検出している．

作成しデータ処理システムを利用して，ファイバー干渉測定システムの評価を行った．図2-6は，ブロックゲージを用いた評価手法の模式図であり，図2-7は実験システムの写真である．このシステムを利用して，絶対距離測定の評価を行った．150 mmのブロックゲージの長さ測定を，100 nmの精度で測定できることを確認した（図2-8）．

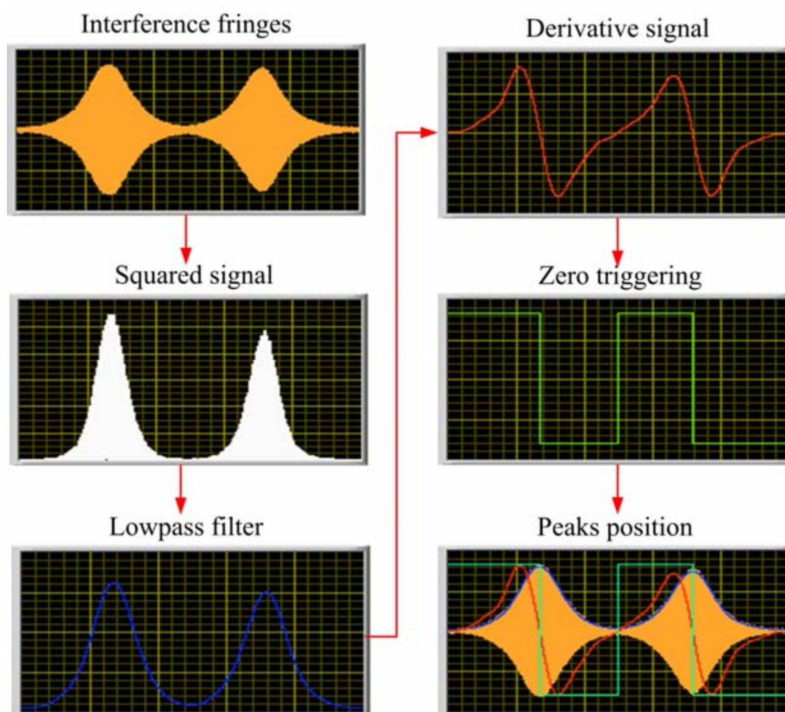

図2-5　干渉縞信号のデータ処理：ピークの検出手法

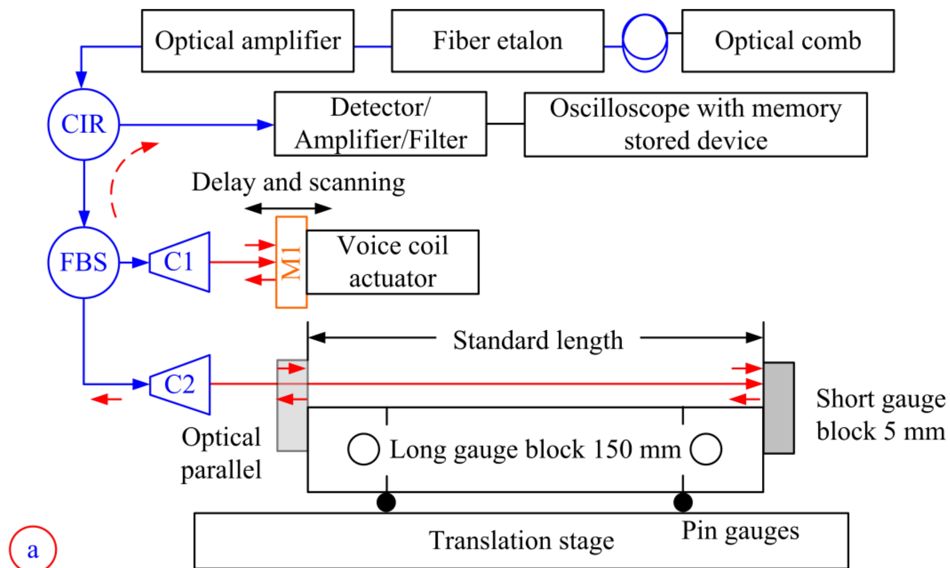

図2-6　パルス干渉計の精度評価のためのシステムの構成図

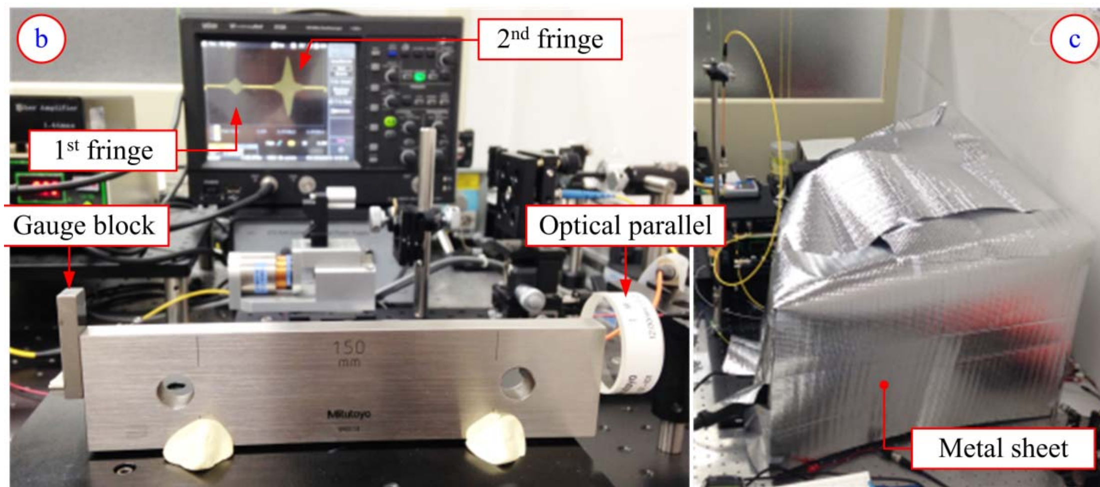

図2-7　パルス干渉計の精度評価のためのシステムの写真

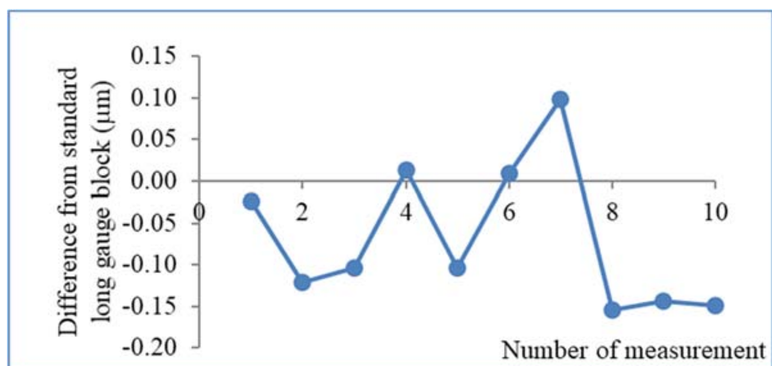

図2-8　パルス干渉計の精度評価例

3. 光コムレーザの三次元測定機の精度評価への適用

3.1 三次元測定機の受入検査

三次元測定機の受入検査における精度評価の方法は，JIS B7440シリーズ（ISO 10360シリーズ）で規定されている．寸法計測における基本的な寸法精度は，値付けられたアーティファクト（ステップゲージ，ブロックゲージなど）の寸法と寸法測定の差によって評価する．評価する位置としては，測定範囲内の7つの位置方向において，5つの寸法測定をそれぞれ3回繰り返し行うことが決められている（図3-1）. 7つの位置方向のうち，4つについては測定範囲の対角4方向と定められている．寸法誤差の最大値が，三次元測定機の最大許容誤差（MPE: Maximum Permissible Error）以内であることで，その三次元測定機の精度が保証されたことになる. この検査の実施には, アーティファクトの設定, 温度慣らしなど時間と手間がかかる.

測定に利用するアーティファクトとしては，従来から図3-2 (a) および図3-2 (b) で示すようにブロックゲージおよびステップゲージが利用され, 双方向測定によって精度評価を行っていた．しかし，三次元測定機の高精度化により，より高精度な測定方法としてレーザ測定機が使われている（図3-2 (c)）．さらに大型の三次元測定機に対しては，1.5 m以上の長さのブロックゲージやステップゲージがないことから，レーザ測長機を使うことが必須となっている．しかし，従来のレーザ測定機はインクリメンタルな測定のためアライメントなどが難しいこと，レーザ光路を遮ると測定がやり直しになること，波長校正を介してトレーサビリティを確保していることなどが問題となっている. そこで，トレーサビリティが直接確保でき，絶対的な測定が可能な光コムの利用が期待されている.

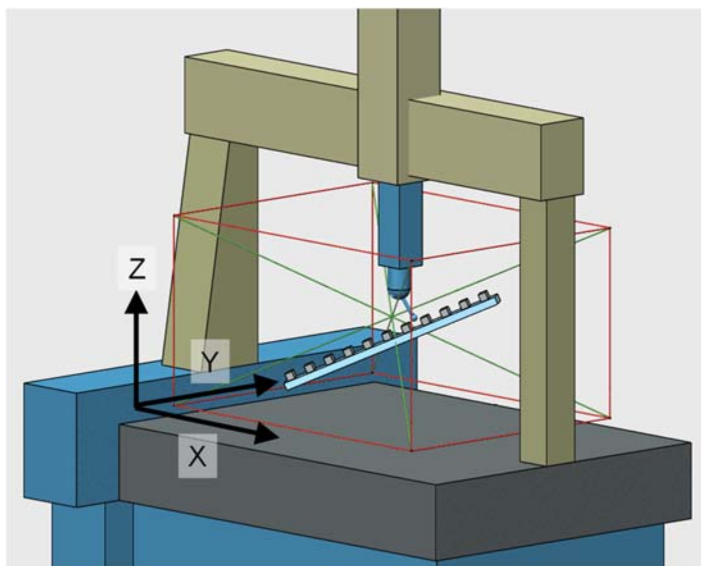

(a) 7つの位置方向のうち4方向は測定範囲の対角方向

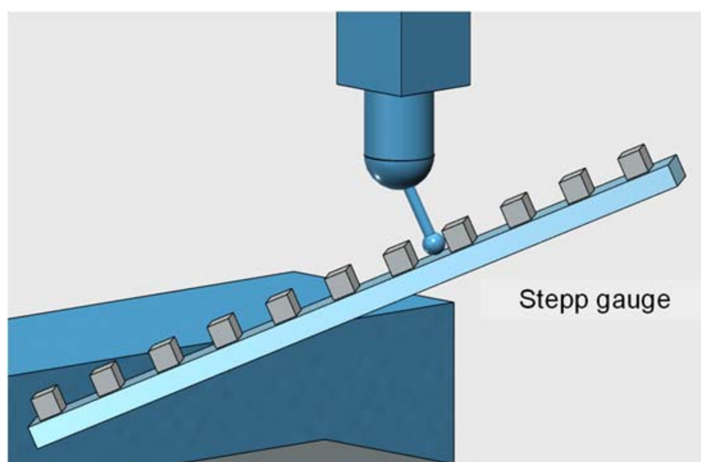

(b) ステップゲージの測定

図3-1　JIS B7440-2の検査：測定範囲内の7つの位置方向において5つの寸法測定をそれぞれ3回測定する

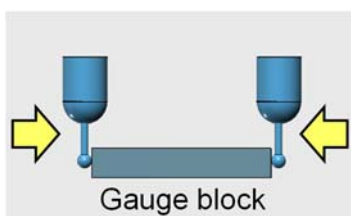

(a) ブロックゲージ

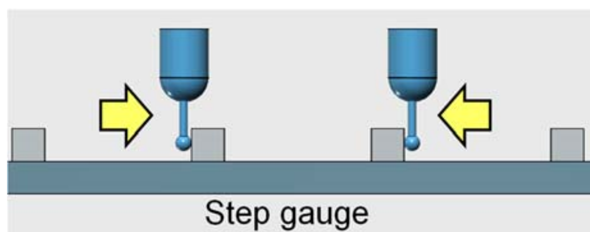

(b) ステップゲージ

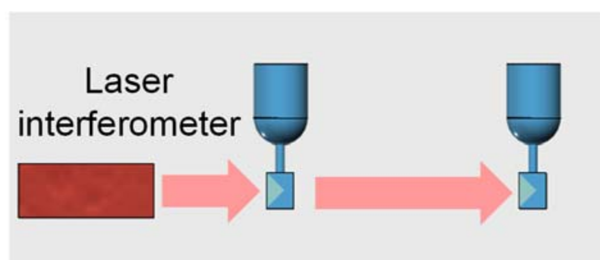

(c) レーザ測長機

図3-2　ブロックゲージ，ステップゲージおよびレーザ測長機による寸法測定精度評価

3.2　三次元測定機の精度評価用パルス干渉計

JIS B7440-2に基づく，レーザ測長機による三次元測定機（特に大型）の精度評価の効率を考えると，前述したようなレーザ測長機の作業およびアライメントの効率が大きな問題となる．光コムによるパルス干渉では，測定中にレーザを遮ってもいいことで作業が簡単になり，ボールレンズをターゲットとすることでアライメントが容易になった．

この干渉計を三次元測定機に適用した．このシステムでは，ボールレンズを三次元測定機のプローブ位置に取り付け，干渉計のターゲットとした．ボールレンズが使えるためアライメントが簡単であり，絶対距離測定のため測定中にレーザが遮られても測定に影響がでない．さらに，ファイバーによってトレーサブルな基準が供給できるなどのメリットがあった．光コムにより高精度な光基準はファイバーで供給できるため，この実験では，光コム用のレーザは建物の10階に設置し，地下の恒温室に設置された三次元測定機まで光ファイバーで信号を供給することで実験が行えた．

図3-3は，対角の寸法精度を評価した例である．使用した三次元測定機は，最大許容誤差（MPE）が±（1.9 μm + 3L/1000）μmのものである．ステップゲージによる従来の手法と，提案した光コムによる手法による評価はほぼ一致している（図3-4）．1つの対角の測定に必要な時間は，ステップゲージの場合は温度ならしを含めて3時間以上かかるが，光コムによる方法では30分以内に行うことができた．また，不確かさも提案手法のほうが小さく見積もられている．

図3-5は，将来的な展望である．光コムレーザとスキャナーを組み合わせることで，直接的に三次元絶対座標の測定が可能と考えられる．

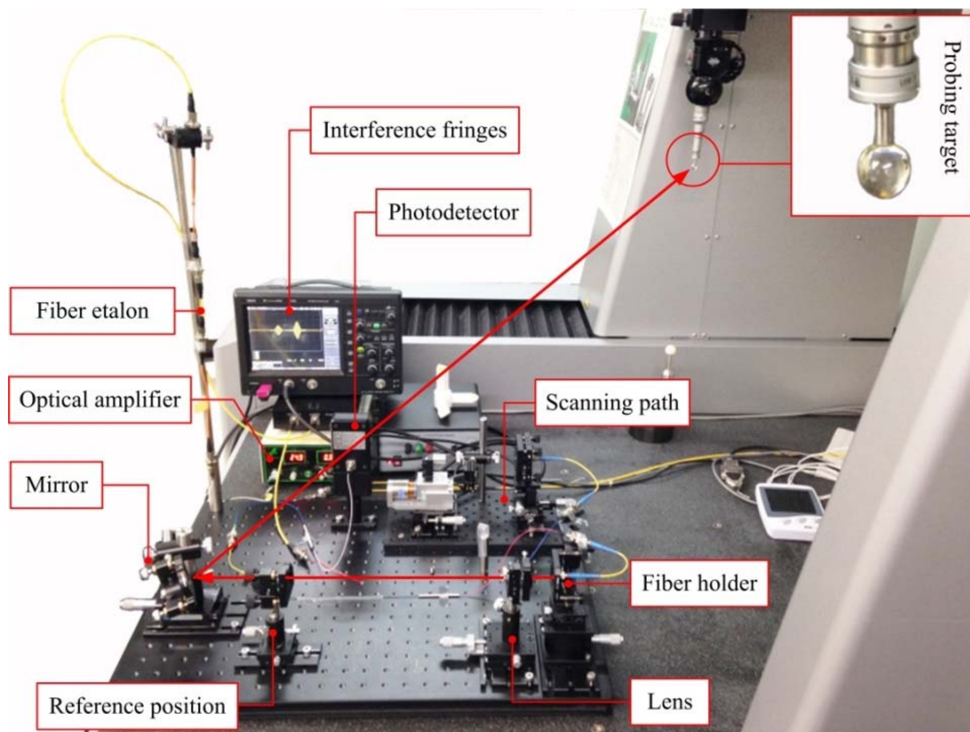

図3-3　三次元測定機の対角測定の精度評価の例

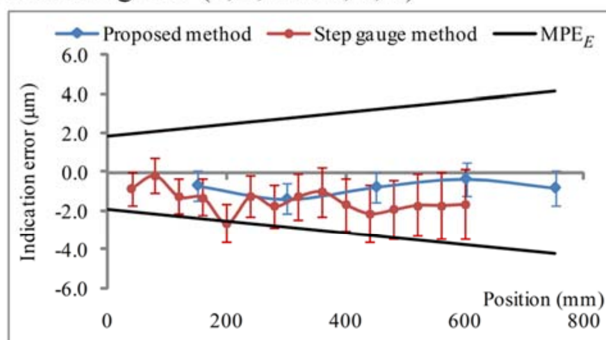

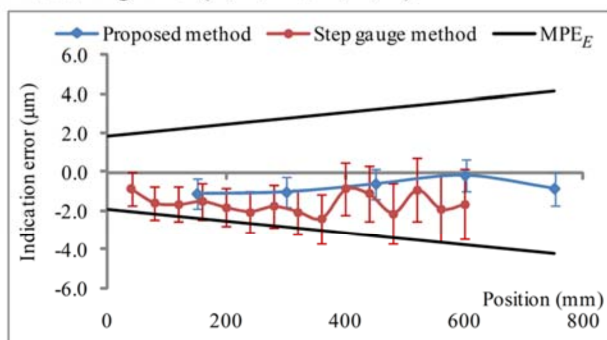

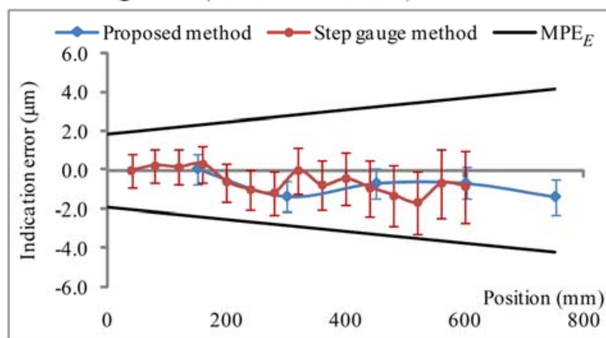

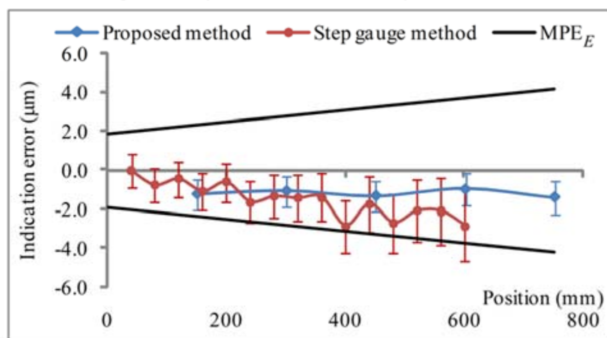

図3-4　提案手法とステップゲージによる方法との比較

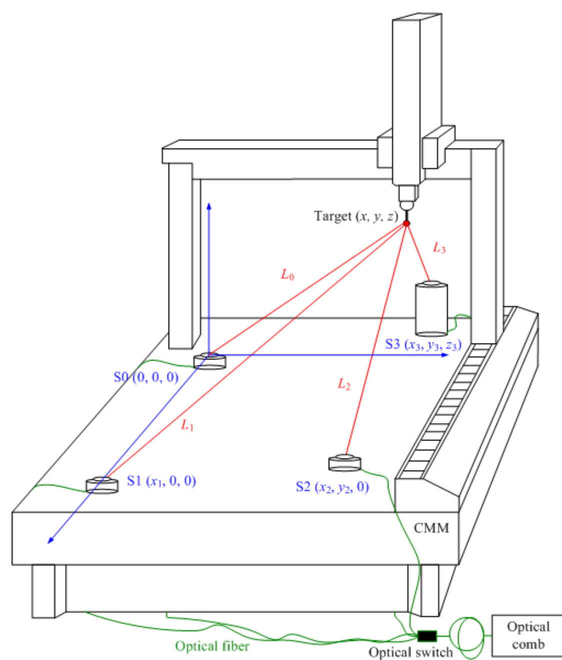

図3-5　スキャナーシステムを利用した三次元絶対位置測定の構成図

4. マルチビームオートコリメータシステムの試作および基本動作確認

図4-1は，ボールレンズを対象としたパルス干渉の精度評価を行うためのマルチビームオートコリメータシステムの構成図である．この図に基づくシステムの試作を行った．図4-2に製作したマルチビームオートコリメータを示す．基本動作の確認は終了したが，精度評価は今後の課題となっている．

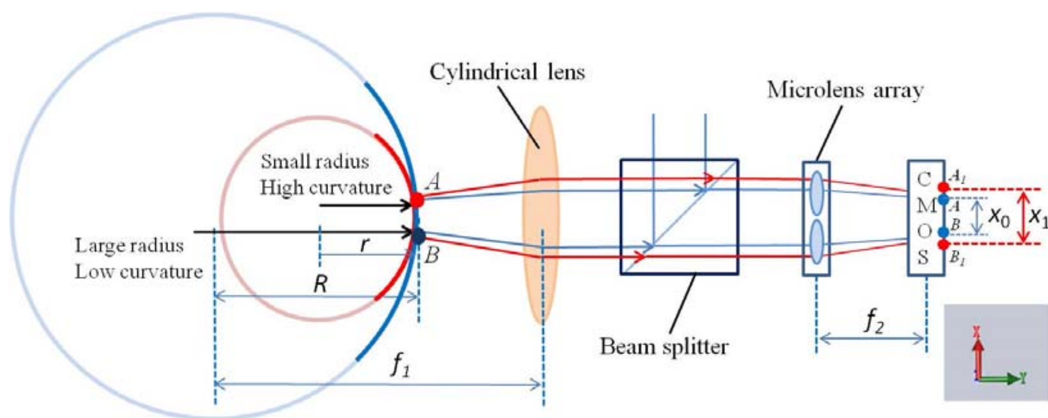

図4-1　マルチビームオートコリメータシステムの構成図

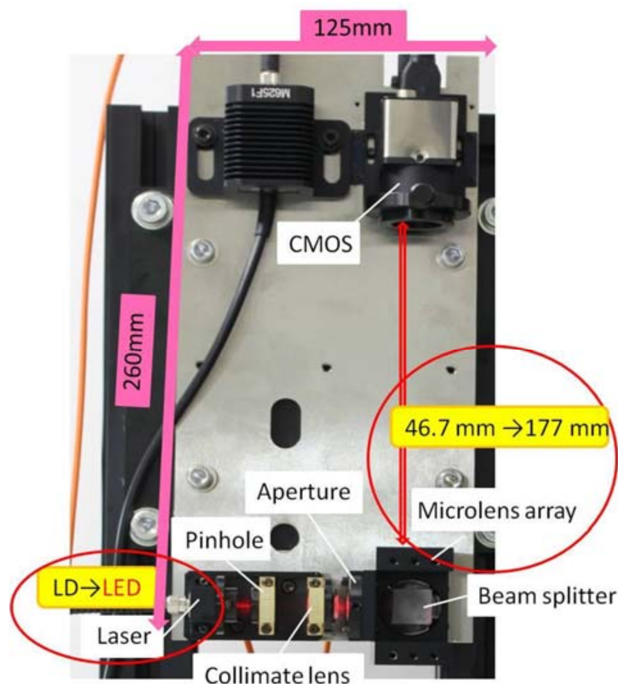

図4-2　製作したマルチビームオートコリメータ

5. まとめ

光コムレーザによる３次元絶対位置測定システムの開発を行った．光コムレーザを利用したパルス干渉計を構築した．光コムレーザは，周波数基準によって直接ロックされているため安定性は10^{-9} 以上あり，測定では測定精度は，干渉信号から光路差の計測および環境による空気の屈折率の補正によって決定する．今回開発したパルス干渉計では，長さ測定の拡張不確かさは1 mの測長に対して0.26 μm，10 mの測長に対して1 μm程度と推定されるので，一般的な大型な三次元測定機および三次元構造物の寸法精度評価に十分な精度が達成できている．実際の測定精度は，温度の分布による環境の影響および三次元測定機の位置決め精度の影響が支配的となる．

光コムのパルス干渉計を，ファイバーエタロンを利用してパルス間隔を短くすることで，三次元測定機の精度評価へ応用した．光コムは，光ファイバーによりトレーサブルな長さ標準をどこにでも供給することができ，今後の長さ測定の校正では，最も有力がツールとなると考えられる．今回の実験では，ボールレンズをターゲットとしたため，効率的な精度評価が可能となった．また，ステップゲージでの精度評価と比較して，作業時間および測定不確かさで提案手法のほうが優れていることが確認できた．

今回説明したシステムが，大型工作機械，大型構造物，ロボットなどの多くの三次元機器の測定へ適用することを期待している．

本研究の成果を以下の示す．

- 光コムレーザによるパルス干渉計を構築し，絶対距離を高精度（拡張不確かさは1 mの測長に対して0.26 μm，10 mの測長に対して1 μm程度）で測定できることを示した．
- パルス干渉計において，ボールレンズをターゲットとすることで，自由度が高くアライメントが容易な3次元的な測定が可能となることを示した．
- パルス干渉計にファイバーエタロンを導入することで，パルス間隔を短くし，短い距離間隔で絶対測定が可能となった．
- パルス干渉計を3次元測定機に適用し，従来の方法より高精度で短時間で3次元測定機の精度評価が行えることを示した．
- 今回開発したシステムが，大型工作機械，大型構造物，ロボットなどの多くの三次

元機器の測定へ適用する可能性を示した.

6. 関連論文リスト（平成27年度および平成28年度発表分）

6.1　雑誌論文（添付）

- Wiroj Sudatham, Hirokazu Matsumoto, Satoru Takahashi, Kiyoshi Takamasu: Verification of the positioning accuracy of industrial coordinate measuring machine using optical-comb pulsed interferometer with a rough metal ball target, Precision Engineering 41, 2015, 63-67
- Meiyun Chen, Satoru Takahashi, Kiyoshi Takamasu: Development of high-precision micro-roundness measuring machine using a high-sensitivity and compact multi-beam angle sensor, Precision Engineering 42, 2015, 276-282
- Hirokazu Matsumoto, Kiyoshi Takamasu: Automatic Recording Absolute Length-Measuring System with Fast Optical-Comb Fiber Interferometer, International Journal of Automation Technology 9 (5), 2015, 482-486
- Wiroj Sudatham, Hirokazu Matsumoto, Satoru Takahashi, Kiyoshi Takamasu: Non-contact measurement technique for dimensional metrology using optical comb, Measurement 78, 2016, 381-387
- Wiroj Sudatham, Hirokazu Matsumoto, Satoru Takahashi, Kiyoshi Takamasu: Diagonal in space of coordinate measuring machine verification using an optical-comb pulsed interferometer with a ball-lens target, Precision Engineering 43, 2016, 486-492
- Chen Meiyun, Takahashi Satoru, Takamasu Kiyoshi: Calibration for the sensitivity of multi-beam angle sensor using cylindrical plano-convex lens, Precision Engineering 46, 2016, 254-262
- Dong Wei, Kiyoshi Takamasu, Hirokazu Matsumoto: Is the Two-Color Method Superior to Empirical Equations in Refractive Index Compensation?, Optics and Photonics Journal,

2016 (6), 8-13

- Chen Meiyun, Satoru Takahashi, Kiyoshi Takamasu: Precise flatness measurements using an optical multi-beam angle sensor, International Journal of Precision Engineering and Manufacturing 17 (9), 2016, 1093-1099

- Taro Onoe, Satoru Takahashi, Kiyoshi Takamasu, Hirokazu Matsumoto: Non-contact precision profile measurement to rough-surface objects with optical frequency combs, Measurement Science Technology 27, 2016, 124002-1-7

6.2 国際会議発表

- Wiroj Sudatham, Hirokazu Matsumoto, Satoru Takahashi, Kiyoshi Takamasu: Absolute precision measurement for space coordinates metrology using an optical-comb pulsed interferometer with a ball lens target, 15th euspen International Conference (euspen2015), Leuven, Belgium, 2015, 109-110

- Chen Meiyun, Genki Miyazaki, Satoru Takahashi, Kiyoshi Takamasu: Roundness measurement machine using multi-beam angle sensor - experimental verification of multi-beam angle sensor, 15th euspen International Conference (euspen2015), Leuven, Belgium, 2015, 125-126

- Taro Onoe, Satoru Takahashi, Kiyoshi Takamasu, Hirokazu Matsumoto: (Invited Paper) Non-contact precision profile measurement to rough surface objects with optical frequency combs, 12th International Symposium on Measurement Technology and Intelligent Instruments (ISMTII 2015), Taipei, Taiwan, 2015, 1079 1-5

- Yumi Iwago, Tomohiko Takamura, Yohan Kondo, Youichi Bitou, Satoru Takahashi, Kiyoshi Takamasu: Self Calibration Method for Nanometer Profile Measurement on Large Aspheric Optical Surface, 12th International Symposium on Measurement Technology and Intelligent Instruments (ISMTII 2015), Taipei, Taiwan, 2015, 1097 1-6

- Fuminori Kimura, Taro Onoe, Satoru Takahashi, Kiyoshi Takamasu, Hirokazu Matsumoto: Precision absolute distance measurement technique onto rough surface object using self-beat signals of optical frequency comb, euspen’s 16th International Conference & Exhibition, Nottingham, UK, P1.25

- Fuminori Kimura, Taro Onoe, Satoru Takahashi, Kiyoshi Takamasu, Hirokazu Matsumoto: Non-contact Precision Profile Measurement to Rough Surface Objects with Optical Frequency Combs, ICPE2016, 16th International Conference on Precision Engineering, Hamamatsu, Shizuoka, Japan, 2016, A312-8209

- Winarno Agustinus, Shusei Masuda, Satoru Takahashi, Hirokazu Matsumoto, Kiyoshi Takamasu, Takao Kitayama, Ryota Kudo, Katsuyoshi Endo: Non-Contact Remote Measurement of Internal Distance Between Two Plane Mirrors by Using a Tandem Low-Coherence Interferometer, ASPEN/ASPE 2017 Spring Topical Meeting Manufacture and Metrology of Structured and Freeform Surfaces for Functional Applications, Hong Kong, China, 2017

- Kiyoshi Takamasu: Keynote: High-Accuracy Absolute Length Measurement Using Optical-Comb Pulsed Interferometer and Its Application for Verification of Coordinate Measuring Machines, ASPEN/ASPE 2017 Spring Topical Meeting Manufacture and Metrology of Structured and Freeform Surfaces for Functional Applications, Hong Kong, China, 2017

謝　　辞

本研究は公益財団法人JKAの平成27年度自転車等機械工業振興事業に関する補助事業により実施した．ここに謝意を表する．

Precision Engineering 41 (2015) 63–67

Contents lists available at ScienceDirect

Precision Engineering

journal homepage: www.elsevier.com/locate/precision

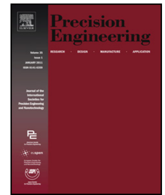

Verification of the positioning accuracy of industrial coordinate measuring machine using optical-comb pulsed interferometer with a rough metal ball target

Wiroj Sudatham [a,*], Hirokazu Matsumoto [a], Satoru Takahashi [b], Kiyoshi Takamasu [a]

[a] *Department of Precision Engineering, The University of Tokyo, Hongko 7-3-1, Bunkyo-ku, Tokyo 113-8656, Japan*
[b] *Research Center for Advanced Science and Technology, The University of Tokyo, Komaba 4-6-1, Meguro, Tokyo 153-8904, Japan*

ARTICLE INFO

Article history:
Received 29 October 2014
Received in revised form
21 December 2014
Accepted 19 January 2015
Available online 7 February 2015

Keywords:
Optical comb
Pulsed interferometer
Length measurement
Coordinate measuring machine
CMM

ABSTRACT

An optical-comb pulsed interferometer was developed for the positioning measurements of the industrial coordinate measuring machine (CMM); a rough metal ball was used as the target of the single-mode optical fiber interferometer. The measurement system is connected through a single-mode fiber more than 100 m long. It is used to connect a laser source from the 10th floor of a building to the proposed measuring system inside a CMM room in the basement of the building. The repetition frequency of a general optical comb is transferred to 1 GHz by an optical fiber-type Fabry–Pérot etalon. Then, a compact absolute position-measuring system is realized for practical non-contact use with a high accuracy of measurement. The measurement uncertainty is approximately 0.6 μm with a confidence level of 95%.

© 2015 Elsevier Inc. All rights reserved.

1. Introduction

A coordinate measuring machine (CMM) is defined by ISO 10360-1 as a measuring system with the means to move a probing system and the capability of determining spatial coordinates on a workpiece surface [1]. CMMs are widely used to measure the three-dimensional sizes, forms, and positions of manufactured parts. However, CMM measurement inaccuracy occurs when there is an error in the relative position between the measured points and the probing points. The errors affecting a CMM have a systematic and a random component. They also directly influence the quality of production inspection [2]. Therefore, CMMs must be calibrated on installation and verified periodically during their operation. The standards and guidelines for CMM verification are based on sampling the length-measurement capability of a CMM to decide whether its performance conforms to the specification [3,4]. Many methods and artifacts are developed to verify CMMs [2–10]. Most standards prefer to use end standards such as a series of gauge blocks, a step gauge, and a ball plate or laser interferometer. However, there is no one perfect method for CMMs, mainly because of the complicated constructions and the three-dimensional positions of many measured points that are necessary in coordinate metrology. In addition, the range of positioning verification is limited by the length of end standards [11,12]. Although a continuous-wave (cw) laser interferometer can measure for the long length, the measuring path cannot be interrupted during the measurement period because it is operated by a cw laser and interference fringe counting method.

Recently, an optical frequency comb has been considered as a useful tool for dimensional metrology, because of their high frequency-stability and direct traceability to SI unit [13]. Several methods for length measurement with an optical frequency comb have been proposed [14–17]. This paper proposes a new technique for the verification of the positioning accuracy of CMMs using an optical-comb pulsed interferometer. A rough metal ball is used as the target of a single-mode fiber interferometer. Because the sphere ball provides 3D targets, the measuring system can be constructed at any location on the surface of a CMM. In addition, the proposed measuring system can be installed on more than one system to measure many positions at the same time with a target as shown in Fig. 1.

A single-mode optical fiber more than 100 m long is used to connect a laser source from a 10th floor of a building to the proposed measuring system inside a CMM room in the basement of the building. The repetition frequency of a general optical comb is transferred to 1 GHz by an optical fiber-type Fabry–Pérot etalon.

* Corresponding author. Tel.: +81 3 5841 6472; fax: +81 3 5841 6472.
E-mail address: wiroj@nanolab.t.u-tokyo.ac.jp (W. Sudatham).

http://dx.doi.org/10.1016/j.precisioneng.2015.01.007
0141-6359/© 2015 Elsevier Inc. All rights reserved.

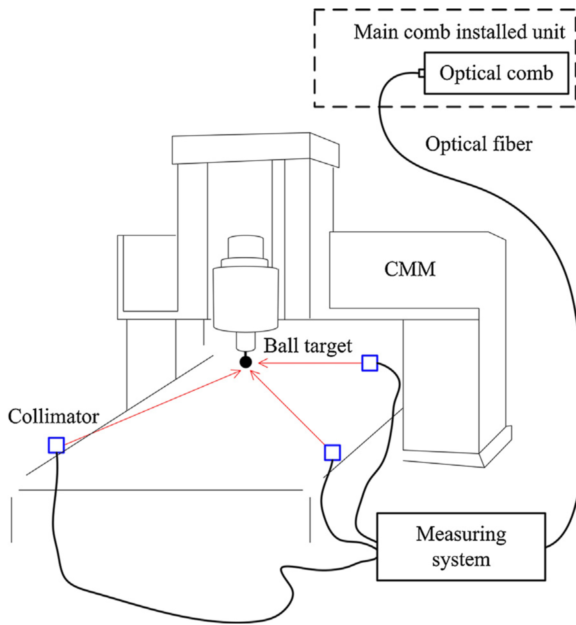

Fig. 1. The concept idea of CMM verification using an optical-comb pulsed interferometer with a rough metal ball target.

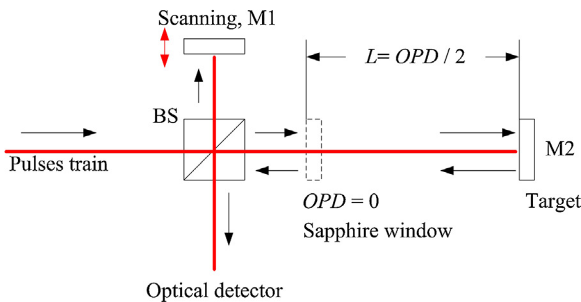

Fig. 2. Principle of an optical-comb pulsed interferometer.

Then, a compact absolute position-measuring system is established based on a single-mode fiber interferometer; a rough metal ball is used as the target because the alignment of the laser beam is easy. The conversion of the time scale, which is presented by envelope interference fringes, to the length scale is measured. The effect of the surface roughness of the target is also examined. The position errors of a moving bridge-type CMM were measured by the proposed measuring system paired with a commercial cw laser interferometer. Finally, the measurement uncertainty is also evaluated. The uncertainty of the measurement is approximately 0.6 μm with a confidence level of 95%. This technique provides enough accuracy for industrial CMMs.

2. Optical-comb pulsed interferometer

Mode-locked lasers generate ultrashort optical pulses by establishing a fixed-phase relationship across broad spectrum of frequencies. The spectrum of each pulse train is separated by the repetition rate of an optical comb, and the series of spectrum lines is called an optical frequency comb. In the time domain, the pulse train is emitted at the same time by a mode-locked laser [13]. The pulsed interferometer remains the principle of an unbalanced-arm Michelson interferometer where an optical comb is a laser source. As shown in Fig. 2, an optical comb generates a pulse train. Laser pulses are divided into two beams by an optical beam splitter (BS). One beam is reflected on a scanning mirror (M1), while the other is transmitted through a sapphire window (reference position) to the target mirror (M2).

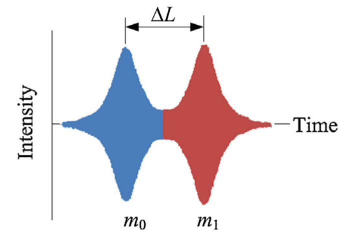

Fig. 3. Two interference fringes of an optical-comb pulsed interferometer; m_0 and m_1 are the fringe order at the reference position and the target position, respectively.

Subsequently, the reflected light pulses from a scanning mirror (M1) are recombined with the returned light pulses from a sapphire window and a target mirror (M2) to produce interference fringes when the optical path difference (*OPD*) between two arms follows Eq. (1) [14].

$$OPD = \frac{mc}{nf_{rep}} \quad (1)$$

where m is an integer, c is the speed of light in the vacuum, n is the refractive index of air, and f_{rep} is the repetition frequency.

Normally, two interference fringes will overlap when an optical-comb pulsed interferometer exactly satisfies the condition of Eq. (1). In practical use, the envelope peak of the interference fringes will be separated if displacement is provided (ΔL). The result is illustrated in Fig. 3.

Therefore, the position/length under measurement is determined by Eq. (2).

$$L = \frac{OPD}{2} + \Delta L \quad (2)$$

In application, two envelope interference fringes in Fig. 3 are presented in the time domain. The first fringe comes from the reference position when the *OPD* is zero ($m_0 = 0$), and the second fringe comes from the target when the *OPD* is around 300 mm ($m_1 = 1$). Therefore, the conversion of the time scale to the length scale of the peak-to-peak measurement of the envelope interference fringes must be measured because it relates to the speed of the scanning-fringe device. Moreover, the position/length under measurement must be corrected for the group refractive index of air due to changes in environmental conditions [18].

3. Experiments and results

3.1. Time scale and length scale measurement

The relationship between the time scale and the length scale measurement is required because the peak-to-peak of the envelope interference fringes shown in Fig. 3 is presented in the time domain. The measurement setup diagram to determine this relation is shown in Fig. 4.

A laser source (an optical comb C-Fiber Femtosecond Laser, Menlo Systems) generates a short pulse train with a repetition frequency of 100 MHz and a central wavelength of 1560 nm. The repetition rate was modified by a Fabry–Pérot fiber etalon. An optical fiber-type etalon was prepared from a special-cut length of a single-mode optical fiber (SMF-28). Both ends of the fiber are FC connectors (fiber-optic connector) whose surfaces are coated with 93% reflectivity to generate a 1-GHz FSR (free spectral range). The stability of repetition frequency after passing through a Fabry–Pérot fiber etalon was observed by a universal counter (SC-7206, Iwatsu). It was performed at an order of 10^{-9} over 2 h [16]. Subsequently, the laser beam was amplified by an optical amplifier.

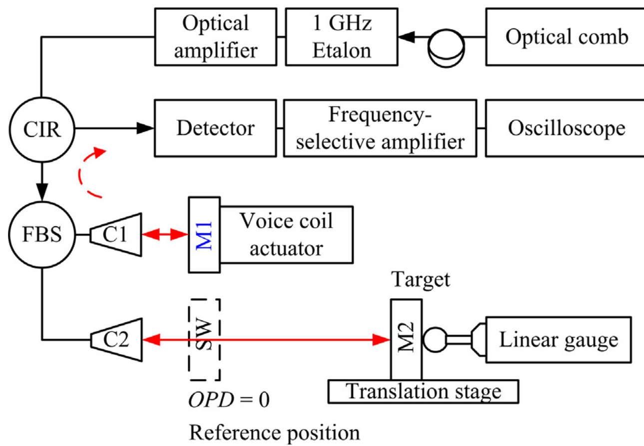

Fig. 4. Measurement setup diagram of the relationship between time scale and length scale measurement; CIR is optical fiber circulator, FBS is fiber beam splitter, C1 and C2 are collimators.

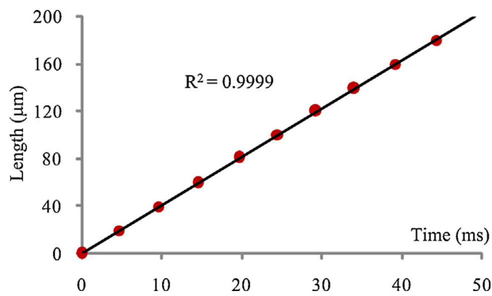

Fig. 5. Best-fit line of time and length scale.

The laser beam crosses an optical fiber circulator (CIR) to the fiber beam splitter (FBS), and then the beam is divided into two paths by the FBS. One beam falls onto a scanning mirror (M1) that is fixed on a voice coil actuator; the other falls onto a target mirror (M2) attached to a precise translation stage via a collimator (C2) and a sapphire window (SW). A linear gauge (Laser Hologauge LGH-110, Mitutoyo) with a resolution of 10 nm was installed behind a target mirror (M2). In practice, two interference fringes will occur on the screen of an oscilloscope when the distance from the reference position to the target is approximately 150 mm. After that, the target was moved far away from the reference position by a translation stage controller (FC-401, Sigma Tech). Then, the length scales were measured by a linear gauge. Using the same process, the time scales were determined from the peak-to-peak measurement of the envelope interference fringes, which appeared on the screen of an oscilloscope. In this experiment, a voice coil actuator was operated with a constant speed of 0.001 m/s. The measurement results are shown in Fig. 5.

Fig. 5 is a least-squares fitting of the data set between the length scale (y-axis) and the time scale (x-axis); this was repeated 11 times. The maximum deviation between the dependent variable (length scale) and the best-fit line is approximately 0.31 μm, the standard deviation is approximately 0.23 μm, and the correlation coefficient (R^2) is approximately 0.9999. This indicates that two data sets match a straight line that is obtained by a correlation coefficient value. This relation is linear. In experiments, the hysteresis of the scanning-fringe device is not considered because a one-way direction of scanning fringe is required for the proposed method. Conversely, this relation relates to the scanning speed of a voice coil actuator. Therefore, a constant speed of the scanning-fringe device is necessary during measurement.

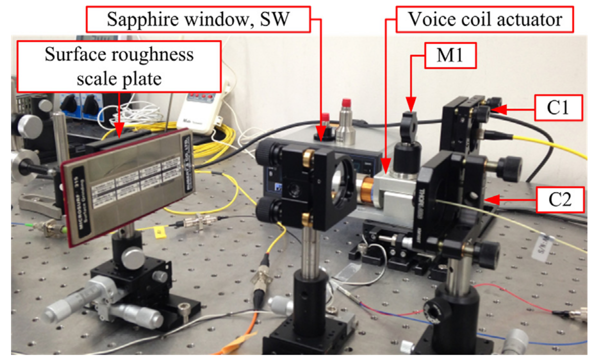

Fig. 6. Measurement setup to determine the effect of the surface roughness of targets on interference fringes.

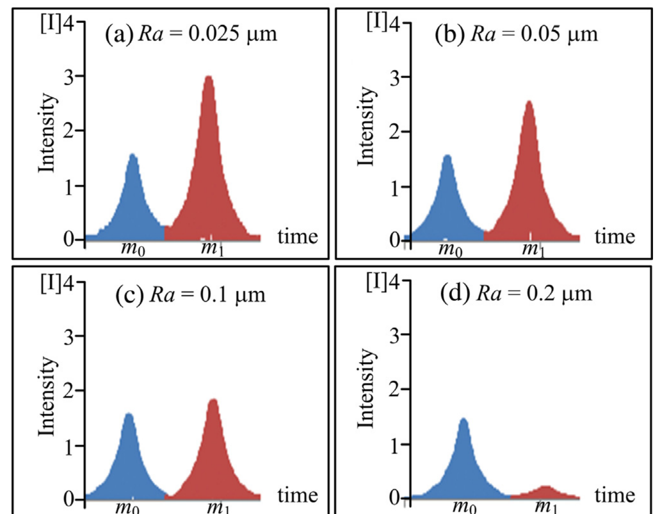

Fig. 7. Intensity of the interference fringes on different target *Ra* values; the red graphs are the fringes which come from the target, others come from the reference position. (For interpretation of references to colour in this figure legend, the reader is referred to the web version of this article.)

3.2. Surface roughness of the target

This experiment explains the effect of the surface roughness of the target on the absolute length measurement. The measurement setup is illustrated in Fig. 6.

A surface roughness scale plate with *Ra* values of 0.025 μm, 0.05 μm, 0.1 μm, and 0.2 μm was used as the target 150 mm from the reference position. Then, the interference fringes were recorded. The results are shown in Fig. 7

The results in Fig. 7 indicate that the intensity of the interference fringes, which are reflected from the surface of the target, is significantly weak if the value of *Ra* is increased. Next, the same plate was moved to a distance of 1500 mm. The length from the reference position to the targets was measured 10 times and evaluated by Eq. (2). The measured standard deviations of length were obtained and paired with the roughness surface of the target. The experimental results are shown in Table 1.

The standard deviations of the length measurement are shown in Table 1; they are gradually enlarged if the value of *Ra* value of the target is increased. When the surface roughness of the target is greater than 0.2 μm, it cannot be used as the target because the reflected beam from that target is not returned to single-mode fiber of the interferometer. The results from both Fig. 7 and Table 2 indicate that the surface roughness of the target significantly affects the performance of the proposed measuring system.

Table 1
Standard deviations of length measurement to surface roughness targets.

Nominal length (mm)	Surface roughness, *Ra* (μm)	Standard deviations (μm)
1500	0.025	0.59
	0.05	0.64
	0.1	0.74
	0.2	–

Table 2
Positioning measurement results of *y*-axis of a CMM.

CMM (mm)	Proposed method (mm)	Position error 1 (μm)	Standard deviation (μm)
0.000	0.0000	0.00	0.00
149.857	149.8557	1.31	0.29
299.714	299.7127	1.33	0.41
449.571	449.5690	2.01	0.47
CMM (mm)	Renishaw laser (mm)	Position error 2 (μm)	Standard deviation (μm)
0.000	0.0000	0.00	0.00
149.857	149.8559	1.11	0.14
299.714	299.7126	1.43	0.21
449.571	449.5692	1.77	0.24

3.3. The measurement of positioning accuracy of a CMM

In this experiment, a rough metal ball was used as the target of a single-mode fiber interferometer for the positioning measurement of a CMM. A single-mode optical fiber more than 100 m long was used to connect a laser source from the 10th floor of a building to the proposed measuring system inside a CMM room in the basement of the building. Then, the positioning accuracy of a CMM was measured and paired with a cw laser interferometer (Renishaw). The measurement setup is shown in Fig. 8.

A rough metal ball with an *Ra* of 0.1 μm; a diameter of 25 mm and a retroreflector were attached to the probing system of a CMM. A moving bridge-type CMM (FALCIO APEX 707, Mitutoyo) was used in this experiment. The positions of measurement were controlled by the CMM controller. Then, the linear positions of a CMM were measured by the Renishaw laser interferometer and the proposed measuring system. This experiment was conducted in an environmental control room. The average air temperature, relative humidity and air pressure were approximately 22.35 °C, 21.1%RH, and 100.40 kPa, respectively. The measurement results of five time repetitions are summarized in Table 2.

The measurement results shown in Table 2 were corrected for the group refractive index of air to the reference temperature [19]. The position error 1 shows the position errors of a CMM that are determined by the difference between the values of the CMM positions and the values measured by the proposed method. The position error 2 is determined by the difference between the values of the CMM positions and the values measured by the Renishaw laser interferometer. The maximum standard deviation of the measurement is approximately 0.47 μm for the proposed measuring system and 0.24 μm for the Ranishaw laser interferometer. The graph in Fig. 9 shows the position errors of the *y*-axis of a CMM paired with the maximum permissible error of indication of a CMM for size measurement—[$MPE_E = \pm(1.9 + 3L/1000)$] μm, where L is the indication length of a CMM in mm. This indicates that the position errors of a CMM show the same trends when measured by both measuring systems. The maximum difference between two curves is approximately 0.24 μm. These results suggest that the proposed measuring system can be applied successfully with high accuracy for industrial CMMs. However, the maximum permissible error of a CMM includes usage of a contact probing system when the measurement is performed. On the other hand, the proposed measuring system is a non-contact type of measurement, and does not contain the effect of the probing error.

a

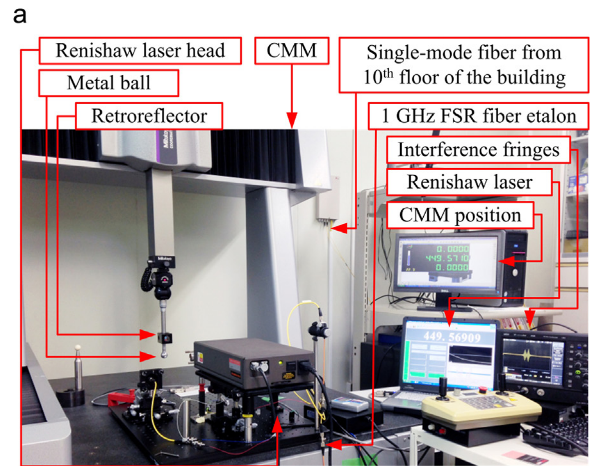

b

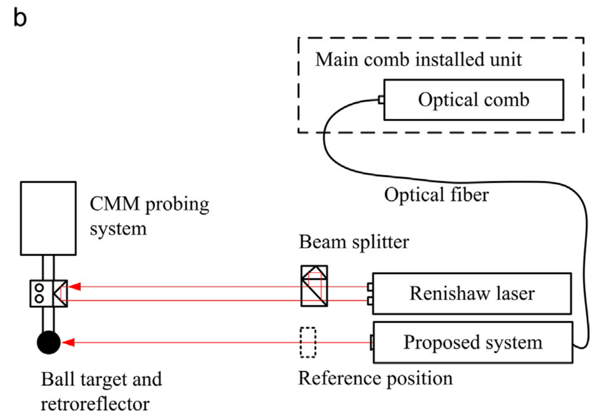

Fig. 8. CMM positioning measurement using proposed measuring system paired with Renishaw laser interferometer. (a) The photograph of measurement. (b) The measurement setup diagram.

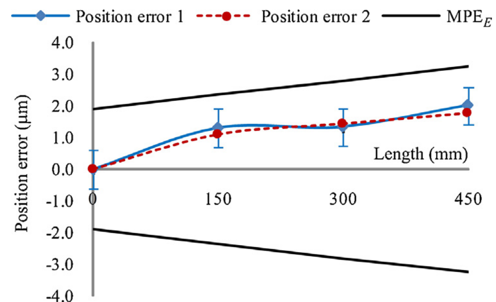

Fig. 9. Position errors of *y*-axis of a CMM; the blue solid line is the position errors of a CMM with gap of the measurement uncertainty that were measured by proposed system. The red dash line is the position errors of a CMM that measured by Renishaw laser interferometer, and the black lines are the maximum permissible error of indication of a CMM for size measurement. (For interpretation of references to colour in this figure legend, the reader is referred to the web version of this article.)

4. Uncertainty of measurement

The uncertainty of CMM positioning measurements has been evaluated following the recommended guideline [20]. The sources of errors under consideration may be divided into three groups. The first group involves the modified frequency source of the optical comb by the Fabry–Pérot fiber etalon. The stability of the

Table 3
Uncertainty evaluation of CMM positioning measurement.

Uncertainty source	Uncertainty value	Uncertainty contribution
Stability of modified frequency source	$<1 \times 10^{-9}$	$2.89 \times 10^{-1}L$
Refractive index of air	1.43×10^{-7}	$1.43 \times 10^{-7}L$
Air temperature	0.15 K	
Air pressure	0.64 kPa	
Air humidity	0.25%RH	
Cidder's formula	2.1×10^{-8}	
Thermal expansion	1×10^{-6}	$8.66 \times 10^{-8}L$
Repeatability of measurement	0.21 μm	
Time and length scale measurement	0.18 μm	
Combined standard uncertainty (k = 2)	$[(0.56)^2 + (33.4 \times 10^{-3}L)^2]^{½}$ μm	

Note: L is the indication length of a CMM in mm.

repetition frequency after passing a Fabry–Pérot fiber etalon is in the order of 10^{-9} over 2 h. This cause is a partial contribution of $0.5 \times 10^{-9}L$ divided by the rectangular distribution, because of semi-range limits of a finite resolution of the used instrument. The uncertainty of the repetition rate and carrier offset frequency is canceled because the accuracy ratio with the MPE_E of a CMM is more than 100 times better. The second group includes the environmental conditions, the compensation of the group refractive index of air, and thermal expansion of linear scale of a CMM. Because of the measurement errors of environmental conditions (air temperature, air pressure and, air humidity) during measurement, the contribution uncertainty of each parameter were determined by the standard uncertainty of each parameter multiple by their sensitivity coefficients. Therefore, the compensation uncertainty for the refractive index of air was calculated to be $1.43 \times 10^{-7}L$, where L is the indication length of a CMM. It was a root of square-sum of distribution uncertainties of air temperature, air pressure, air humidity and Cidder's formula. The coefficient of thermal expansion of the linear scale of a CMM is approximately of 8.0 μm m^{-1} K^{-1} with an uncertainty of ± 1 μm m^{-1} K^{-1}. In this experiment, the changes of temperature of linear scale of a CMM cannot be measured directly. Therefore, the uncertainty due to thermal expansion of linear scale in a CMM was determined from the changes of air temperature, because thermal expansion effect of a CMM was compensated automatically to reference temperature (20 °C) by CMM's software and the measurement values of the air temperature are generally utilized in the place of the scale temperature.

The last group involves the measurement procedures such as measurement repeatability and the uncertainty of time and length scale measurement. The uncertainty of measurement repeatability was approximately 0.21 μm which was evaluated from the maximum standard deviation of five times of measurement repetitions. The uncertainty due to the relationship of time and length measurement is evaluated from the maximum deviation between the measured values and the best-fit line and it was assumed to be a rectangular distribution. The error sources and their uncertainties of the measurement uncertainty are summarized in Table 3.

5. Conclusions

An optical-comb pulsed interferometer whose repetition frequency is transferred from 100 MHz to 1 GHz by an optical fiber-type Fabry–Pérot etalon was developed to verify the positioning measurements of industrial CMMs. A rough metal ball with an Ra of 0.1 μm was used as a target of the single-mode fiber interferometer. A moving bridge-type CMM was measured by the proposed technique paired with a Renishaw laser interferometer in an environmental control room. Both systems show the same trend of position error. The expanded uncertainty of positioning measurement is approximately 0.6 μm at the length of 450 mm. The results show that the measurement accuracy is mainly affected by changes in the environmental conditions, while the noise of the interference fringe is caused by air fluctuation and mechanical vibration. The proposed measurement technique is very convenient and is easier to align than using end standards or a continuous-wave laser interferometer. It also provides enough accuracy for measuring linear dimensions of industrial CMMs. The proposed measuring system can be installed at any location on the surface of a CMM. It can also be used on more than one system to measure the lengths because a rough sphere ball offers a 3D target for a single-mode fiber interferometer. Therefore, further research will be undertaken in the future to study the volumetric errors of CMMs.

References

[1] ISO10360-1. Geometrical Product Specification (SPC). Acceptance and reverification tests for coordinate measuring machines (CMM). Part 1: Vocabulary. International Organization for Standardization; 2000.
[2] Barakat NA, Elbestawi MA, Spence AD. Kinematic and geometric error compensation of a coordinate measuring machine. Int J Mach Tool Manuf 2000;40:833–50.
[3] ISO10360-2. Geometrical Product Specification (SPC). Acceptance and reverification tests for coordinate measuring machines (CMM). Part 2: CMMs used for measuring linear dimensions. International Organization for Standardization; 2009.
[4] EAL-G17. Coordinate measuring machine calibration. European Cooperation for Accreditation of Laboratories; 1995.
[5] Aguilar JJ, Aguado S, Santolaria, Samper D. Mutilateration in volumetric verification of machine tool. In: XX IMEKO World Congress. 2012.
[6] Schwenke H, Schmitt R, Jatzkowski P, Warmann C. On-the-fly calibration of linear and rotary axes of machine toolts and CMMs using tracking interferometer. CIRP Ann Manuf 2009;58:477–80.
[7] Trapet E, Wäldele F. A reference object based method to determine the parametric error component of coordinate measuring machines and machine tools. Measurement 1991;9:17–22.
[8] Swornowski PJ. A new concept of continuous measurement and error correction in Coordinate Measuring Technique using a PC. Measurement 2014;50:99–105.
[9] Weckenmann A, Lorz J. Monitoring coordinate measuring machine by calibrated parts, 7th International Symposium on Measurement Technology and Intelligent Instruments. J Phys: Conf Ser 2005;13:183–90.
[10] Curran E, Phelen P. Quick check error verification of coordinate measuring machines. J Mater Process Technol 2004;155–156:1207–13.
[11] Abbe M, Takamasu K, Ozono S. Reliability on calibration of CMM. Measurement 2003;33:359–68.
[12] Cauchick-Miguel P, King T, Davis J. CMM verification: a survey. Measurement 1996;17:1–16.
[13] Cundiff ST, Ye J. Femtosecond optical frequency comb. Rev Mod Phys 2003;75:325.
[14] Wang X, Takahashi S, Takamasu K, Matsumoto H. Spatial positioning measurements up to 150 m using temporal coherence of optical frequency comb. Precis Eng 2013;37:635–9.
[15] Matsumoto H, Wang X, Takamasu K, Aoto T. Absolute measurement of baselines up to 403 m using heterodyne temporal coherence interferometer with optical frequency comb. Appl Phys Express 2012;5:046601.
[16] Chanthawong N, Takahashi S, Takamasu K, Matsumoto H. Performance evaluation of a coordinate measuring machine's axis using a high-frequency repetition mode of a mode-locked fiber laser. Int J Precis Eng Manuf 2014;15:1507–12.
[17] Balling P, Křen P, Mašika P, van den Berg SA. Femtosecond frequency comb based distance measurement in air. Opt Express 2009;17:9300–13.
[18] Ciddor PE, Hill RJ. Refractive index of air. 2. Group index. Appl Opt 1999;38:1663–7.
[19] ISO 1. Geometrical product specification (SPC). Standard reference temperature for geometrical product specification and verification. International Organization for Standardization; 2002.
[20] EA-4/02. Evaluation of the uncertainty of measurement in calibration. European Co-operation for Accreditation; 2013.

Precision Engineering 42 (2015) 276–282

Contents lists available at ScienceDirect

Precision Engineering

journal homepage: www.elsevier.com/locate/precision

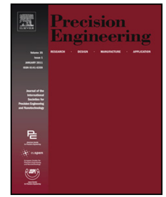

Development of high-precision micro-roundness measuring machine using a high-sensitivity and compact multi-beam angle sensor

Meiyun Chen[a], Satoru Takahashi[b], Kiyoshi Takamasu[a,*]

[a] *Faculty of Engineering, Department of Precision Engineering, The University of Tokyo, 7-3-1 Hongo, Bunkyo-ku, Tokyo 113-8656, Japan*
[b] *Research Center for Advanced Science and Technology, The University of Tokyo, 4-6-1 Komaba, Meguro-ku, Tokyo 153-8904, Japan*

ARTICLE INFO

Article history:
Received 19 January 2015
Accepted 15 May 2015
Available online 2 June 2015

Keywords:
Micro-RMM
Multi-beam angle sensor
Roundness
Autocollimator
Stage-independence

ABSTRACT

With recent development in advanced manufacturing, demand for nanometric accuracy in dimensional metrology has increased dramatically. To satisfy these requirements, we propose a high-accuracy micro-roundness measuring machine (micro-RMM) using a multi-beam angle sensor (MBAS). The micro-RMM includes three main parts: the MBAS, a rotary unit, and a bearing system. The MBAS has been designed and established in order to improve motion accuracy of the micro-RMM. The dimensions of the MBAS are $125(L)\,\text{mm} \times 130(W)\,\text{mm} \times 90(H)\,\text{mm}$. Compared with other methods, an MBAS is less susceptible to spindle error (stage-independence) when detecting angles, can maintain high sensitivity with miniaturized size, and can be used conveniently at the factory level. The optical probe, reported in this paper, is based on the principle of an autocollimator, and the stability is improved when using the MBAS. Unlike multi-probe methods, the micro-RMM is constructed to realize roundness measurement by using only one probe, which is less susceptible to instrumental errors. Experimental results confirming the feasibility of the multi-beam angle sensor for roundness measurement are also presented.

© 2015 Elsevier Inc. All rights reserved.

1. Introduction

In recent years, there has been a growing demand for high-accuracy surface roundness measurement techniques and for simple instruments that can be used conveniently in situ, including in fields such as optical metrology, semiconductors, and space satellites [1–3].

To measure roundness errors of cylindrical workpieces and spindle errors of machine tools in on-machine conditions, it is important to distinguish between roundness error and spindle error. There are two methods of distinguishing these errors: the multi-orientation method and the multi-probe method [4–7].

The multi-orientation method can differentiate the spindle error and the roundness error effectively if the spindle error has good repeatability. Compared with multi-orientation methods, multi-probe methods are more suitable for on-machine measurements because it does not depend on the repeatability of the spindle error [8–10].

Reversal methods can be used to eliminate the systematic errors of a spindle; however, they are very time consuming and still demand good repeatability of spindle motion. This has led us to the solution of using the measured object itself as a reference by employing the three-point method [11–13]. However, using numerous sensors makes it difficult to attach or remove the measured object, and it is not easy to adjust the direction of the sensor's radius.

Several techniques have been proposed and developed for measuring roundness precisely. Each of these methods comes with its own advantages, disadvantages, and limitations [14–18]. This paper analyzes existing techniques and proposes a new technology called multi-beam angle sensor (MBAS) for measuring roundness [19].

From an engineering point of view, the most useful type of surface metrology instrument would probably have an accurate axis of rotation and accurate Cartesian and radial movements; furthermore, it would measure according to a cylindrical frame of reference. However, the disadvantages are that they it can only be used under laboratory conditions, and to get better results, it is necessary to match the co-ordinate system of the measuring instrument to that of the component [20].

In this study, an MBAS based on an autocollimator is proposed for roundness measurement. Compared to other technologies, the micro-RMM uses just one sensor that is less susceptible to instrumental errors when detecting angles, the dimensions of the MBAS are $125(L)\,\text{mm} \times 130(W)\,\text{mm} \times 90(H)\,\text{mm}$ which can be used conveniently at the factory level [21]. In addition, a simple optical-path

* Corresponding author. Tel.: +81 03 5841 6472; fax: +81 03 5841 6472.
E-mail address: chenmeiyun@nanolab.t.u-tokyo.ac.jp (K. Takamasu).

http://dx.doi.org/10.1016/j.precisioneng.2015.05.009
0141-6359/© 2015 Elsevier Inc. All rights reserved.

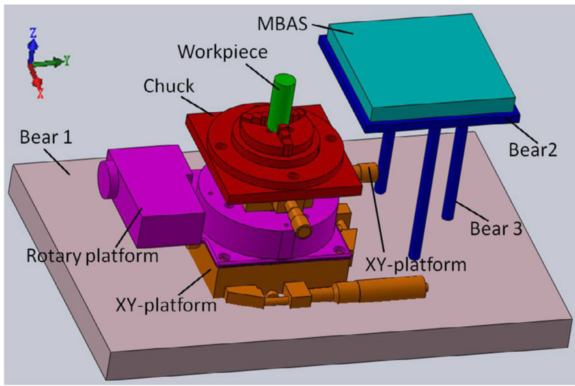

Fig. 1. Schematic of the micro-RMM: an MBAS, a rotary unit, and a bearing system.

design enables the proposed setup to be insensitive to environmental vibration.

2. Micro-RMM configuration

The micro-RMM configuration includes three main parts: an MBAS, a rotary unit, and a bearing system. The MBAS is based on a multi-autocollimator system using a microlens array. It works by projecting an image onto a beam splitter, and measuring the deflection of the returned image against a scale. The reflected angles at several points on the cylindrical workpiece can be measured by a sensor, and the curvature of the workpiece can be calculated by the difference between the two reflected angles. Therefore, the micro-RMM can realize roundness measurement by using the curvature, which is less susceptible to instrumental errors.

Using the MBAS, we designed the experimental system shown in Fig. 1. A cylindrical workpiece is mounted on a chuck, and a rotary platform is mounted between two *XY*-platforms. For roundness measurement, the cylindrical workpiece is rotated by the rotary platform. The axis of rotation of the workpiece spindle is represented by the *Z*-axis. In any roundness measuring instrument, the spindle of a rotary stage is the most important component in its assembly. Here, when the workpiece is assembled, it is necessary to align the *Z*-axis and the axis of the rotary platform to be collinear. The alignment is performed by adjusting the positions of the two *XY*-platforms. Along with the upper *XY*-platform, which is used to achieve minimal spindle error between the workpiece and rotary stage, the lower one is used to approach an almost perfect position between the MBAS and rotary stage.

Fig. 2 illustrates the construction of the MBAS. A laser beam passes through a pinhole and is collimated by a collimator lens. The beam is then bent by a beam splitter and projected through

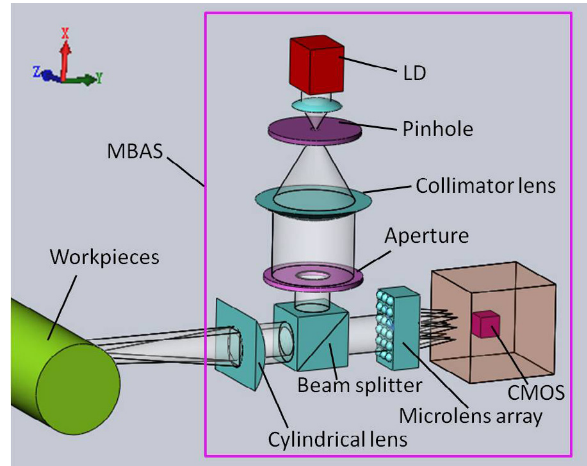

Fig. 2. Construction of the MBAS: the multi-beam angle sensor is based on a multi-autocollimator system using a microlens array.

a cylindrical lens to the workpiece surface. The cylindrical lens is employed in the sensor for removing the influence of the curvature of the cylinder's surface. The reflected beam from the workpiece surface passes through the beam splitter and is focused on a microlens array, which divides the beams into several beams. The resulting pattern is observed and recorded by a CMOS camera mounted along the vertical axis. The image can be observed on a TV monitor. Further processing of the pattern is performed using a PC.

3. Principle of the MBAS

3.1. Calculating the angle difference Δc

To measure roundness errors of a cylindrical workpiece, it is important to obtain the relationship between the radius and the curvature. Fig. 3 illustrates the changing radius of curvature of the workpiece. The red and blue lines delineate a small radius with high curvature and a large radius with low curvature, respectively, f_1 and f_2 are the focal distances of the cylindrical lens and microlens array, respectively, R and r is the radius of curvature of the large radius and small radius, respectively, and x_0 and x_1 are the distance between points A and B, A_1 and B_1 in Fig. 3 of the low curvature and high curvature images, respectively.

Fig. 4 shows the principle of an angle difference measured by the MBAS. Let A and B be representative points of the workpiece. When the radius of curvature changes from R to r, the distance between two points change from x_0 to x_1.

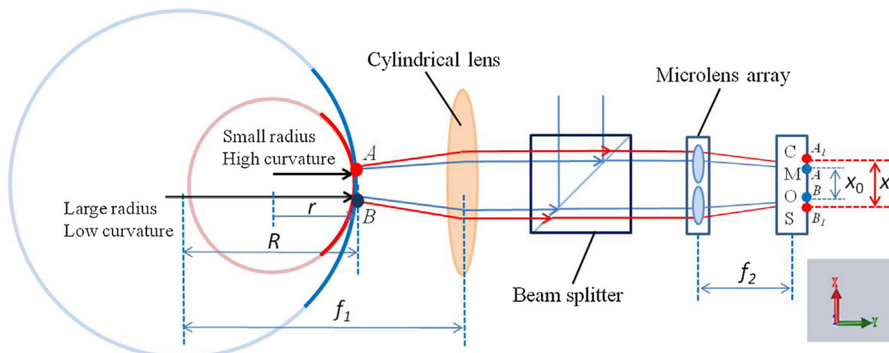

Fig. 3. Radius of curvature comparison: the red and blue lines delineate a small radius with high curvature and a large radius with low curvature, respectively.

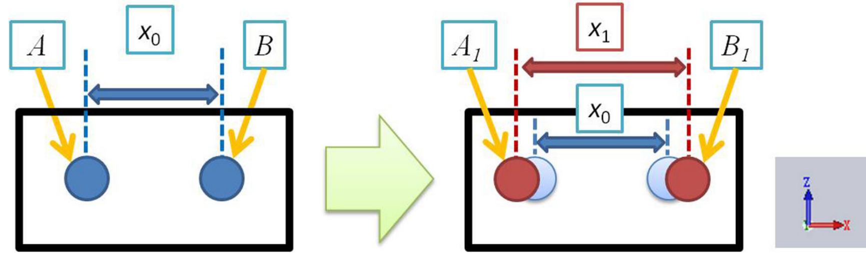

Fig. 4. Calculating the angle difference: from intensity distribution of the center of gravity.

Fig. 5 illustrates the change in angle of a reflected ray when the curvature changes from R to r. The value R–r and t is small compared to R. Thus, it is easily understood that the change in angle of a reflected ray Δc on the surface can be described by the following equation:

$$\Delta c = \frac{1}{r} - \frac{1}{R} = \frac{c_r}{Rt} \quad (1)$$

When the angle of a reflected ray c_r from the workpiece surface passes through the cylindrical lens and microlens array, the output image on the CMOS is presented in Fig. 3. Here, the relationship between the change in the distance of two points Δx and the change in angle of a reflected ray c_r can be calculated as follows:

$$\Delta x = \frac{c_r R f_2}{f_1} \quad (2)$$

Clearly, from Eqs. (1) and (2), the change in angle of a reflected ray Δc can be expressed as

$$\Delta c = \frac{\Delta x f_1}{f_2 R t} = \frac{(x_1 - x_0) f_1}{f_2 R^2 t} \quad (3)$$

3.2. Reducing rotary stage susceptibility

Fig. 6 shows the path of a reflected beam from the surface of a cylindrical workpiece. An optical probe is used to scan the cylindrical workpiece while the workpiece is rotating. Assuming that the center of the cylinder (eccentricity) is at O_1 (o_x, o_y) and the cylinder radius is R and using the MBAS, we can obtain the two measured angles c_a and c_b.

Assuming that the center of the cylinder is O_1 (o_x, o_y), W is a representative point on the workpiece, and the cylinder radius is R, we can obtain the distance of the projected beam b_a by the relationship between the points O, O_1 and W. The distance b_a is then given by

$$(b_a \cos t - o_x)^2 + \left(b_a \sin t - o_y\right)^2 = R^2 \quad (4)$$

$$b_a = o_x \cos t + o_y \sin t + \sqrt{\left(o_x \cos t + o_y \sin t\right)^2 + \left(R^2 - o_x^2 - o_y^2\right)} \quad (5)$$

Through the model of triangle ΔOO_1W, the cosine theorem is used to evaluate the angle c_a, where $2c_a$ is the reflection angle. The angle c_a is given by

$$o_x^2 + o_y^2 = R^2 + b_a^2 - 2Rb_a \cos c_a \quad (6)$$

$$\cos c_a = \frac{R^2 + b_a^2 - o_x^2 - o_y^2}{2Rb_a} = \frac{\sqrt{R^2 - o_x^2 - o_y^2 + \left(o_x \cos t + o_y \sin t\right)^2}}{R} \quad (7)$$

Furthermore, we can approximate c_a and c_b as follows:

$$\cos c_a \approx 1 + \frac{-o_x^2 - o_y^2 + \left(o_x \cos t + o_y \sin t\right)^2}{2R^2} \approx 1 - \frac{c_a^2}{2} \quad (8)$$

$$c_a \approx \frac{o_y \cos t - o_x \sin t}{R} \quad (9)$$

$$c_b \approx \frac{o_y \cos t + o_x \sin t}{R} \quad (10)$$

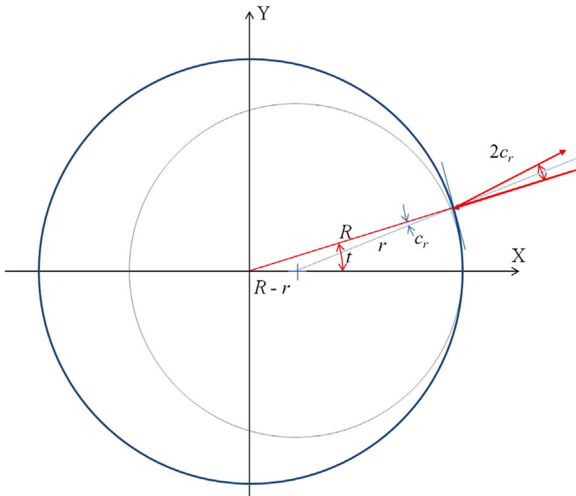

Fig. 5. The change in angle of a reflected ray when the curvature changes from R to r.

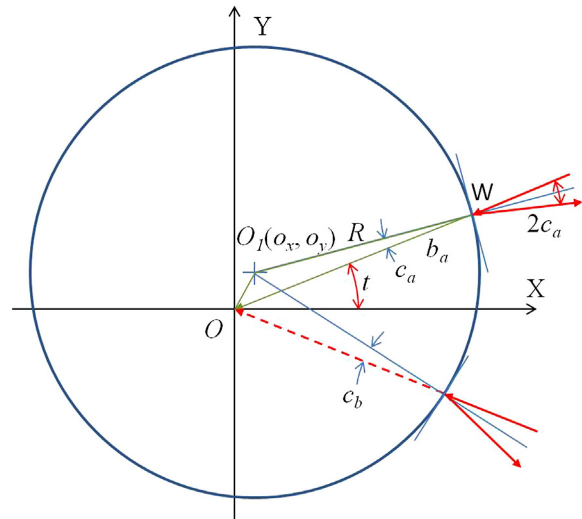

Fig. 6. Relation between eccentricity and reflected beam.

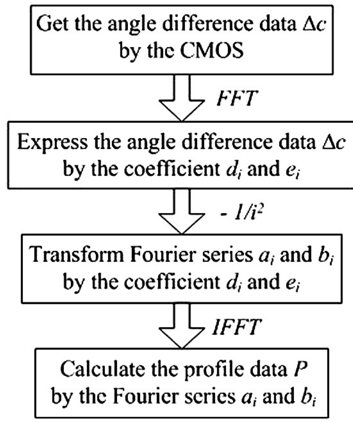

Fig. 7. Algorithm flowchart of the measurement: from angle difference Δc to profile data P use Fourier series.

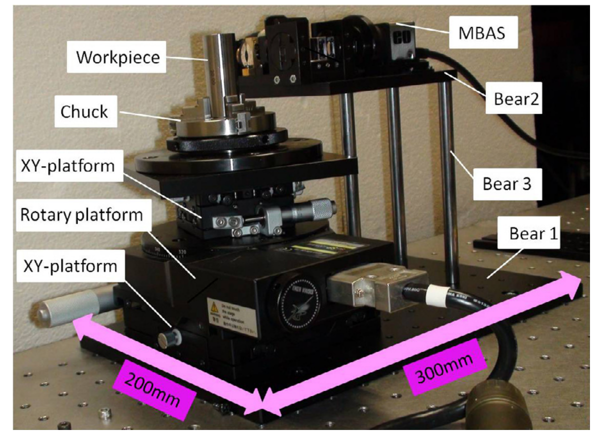

Fig. 8. Micro roundness measuring machine for noncontact roundness measurement: the main setup of the pre-experiment consisted of the MBAS, two *XY*-platforms, a rotary platform, a chuck, and a bearing system.

From Eqs. (9) and (10), the transform of Δc (=$c_a - c_b$), which is the combination that eliminates o_y, is calculated by a simple arithmetic:

$$c_a - c_b \approx \frac{-2o_x \sin t}{R} \tag{11}$$

The value of o_x is small compared to R. Additionally, the influence of the term ($o_x \sin t$) is small. More will be said on this topic in Section 4, the experimental results in Section 4.2 will confirm that the angle difference value Δc is found to be small enough when comparing with random angle error.

Here, the curvature is the angle difference in the small area, and the curvature of the workpiece can be calculated by the angular difference of two reflected beams. Therefore, the micro-RMM can realize roundness measurement by using the curvature, which is less susceptible to instrumental errors.

3.3. *Calculating the profile* P

Fig. 7 shows the algorithm flowchart of the measurement. The profile data P of workpiece in position t can be expressed as a Fourier series, given by

$$P(t_j) = a_0 + \sum_{i=1}^{n} \left(a_i \cos t_j i + b_i \sin t_j i\right)$$
$$t_j = \frac{2\pi (j-1)}{m} \quad (j = 1, 2, \ldots, m) \tag{12}$$

where a_i and b_i are the Fourier series coefficients, n the maximum iterations of the Fourier series, and m the number of sample points. Here, the angle difference Δc can be measured by the sensor, and can also be expressed as the second order differential of the profile data P, given by

$$\Delta c\left(t_j\right) = P''\left(t_j\right) = -\sum_{i=1}^{n} i^2 \left(a_i \cos t_j i + b_i \sin t_j i\right) \tag{13}$$

Then, using a Fourier transformation, we can also transform the angle difference Δc to coefficients d_i and e_i, given by the following equation:

$$c_j = \sum_{i=1}^{n} \left(d_i \cos t_j i + e_i \sin t_j i\right) = P''\left(t_j\right) \tag{14}$$

We note that the relationship between the Fourier series (a_i and b_i) and coefficients (d_i and e_i) can be denoted as

$$a_i = -\frac{d_i}{i^2}, \; b_i = -\frac{e_i}{i^2} \tag{15}$$

Consequently, the profile data P can be denoted as a Fourier series by using an inverse Fourier transform.

The characteristics of the algorithm chart can be estimated by its transfer function, which defines the relationship between the angle difference value Δc and profile data P.

4. Pre-experiment and simulation

4.1. *Configuration of the pre-experiment*

The pre-experimental arrangement is shown in Fig. 8. In the pre-experiment, the MBAS is based on a multi-autocollimator system using a microlens array. Table 1 shows the specifications of the devices in Fig. 8. The main setup of the pre-experiment consisted of the MBAS, two *XY*-platforms, a rotary platform, a chuck, and a bearing system. We used a stage controller to move the rotary platform by using the Labview program in our PC to receive the output signals from the MBAS in each measuring position.

Fig. 9 illustrates the construction of the MBAS. A laser beam from an LD (laser diode) of 650 nm wavelength passes through a pinhole with a diameter of 400 μm and is collimated by the microlens. The beam is then bent by a beam splitter and projected through a cylindrical lens with a focal distance of 50 mm to the workpiece surface. The cylindrical lens is employed in the sensor for removing the influence of the curvature of the cylinder's surface. The reflected beam from the workpiece surface passes totally through the beam splitter and focuses it on the microlens array, which divides the

Table 1
Specifics of devices in micro-RMM (Fig.8).

Laser Diode	Output power: 35 mW (CW) Wavelength: 658 nm
Cylindrical lens	Focal distance: 50 mm (f_1)
Pinhole	Diameter: 400 μm
Aperture	Diameter: 4 mm
Microlens array	Focal distance: 46.7 mm (f_2)
	Pitch of the array: 500 μm
CMOS	Size: 5.6 mm × 4.2 mm
	Valid pixels: 2560 pixel × 1920 pixel
	Sensitive area: 2.2 μm × 2.2 μm

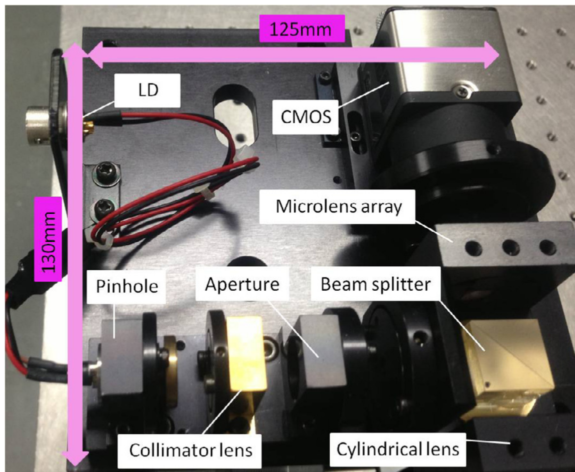

Fig. 9. Construction of the multi-beam angle sensor: the MBAS is based on a multi-autocollimator system using a microlens array.

beams into several beams. The resulting pattern is observed and recorded by a CMOS camera mounted along the vertical axis.

Fig. 10(a) shows an example of one output signal from the CMOS. The scatter plot presents eight lines by eight columns. We choose the points in number four line to calculate the data. In Fig. 10(b) you can see the intensity distribution in the whole and in a spot. By using the intensity distribution, the angle difference data can be calculated. Then, using centroid, we can also estimate the resolution of sensor is about 0.05 μrad.

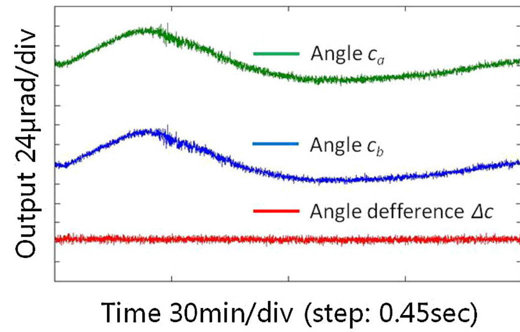

Fig. 11. Stability of multi-beam angle sensor: we measured the stability of angle and angle difference for 2 h.

4.2. Stability of the MBAS

In order to verify the standard deviation of the measurement taken by MBAS in the real environment, we measured the stability of angle and angle difference for 2 h. Fig. 11 shows the results of the angle at point A and point B. In the stability test of the MBAS, the output signals were sampled without rotating the cylinder; therefore, in the pre-experiment, the stability of the MBAS corresponds to the standard deviation of the autocollimator.

The experimental setup is mounted on a table in the basement. In Fig. 11, because the test time was long and the influence of the thermal drift was large. The standard deviation of the angle data at point A was 18.36 μrad. However, the stability of angle difference output was 2.35 μrad. We note that the fluctuation of stability of

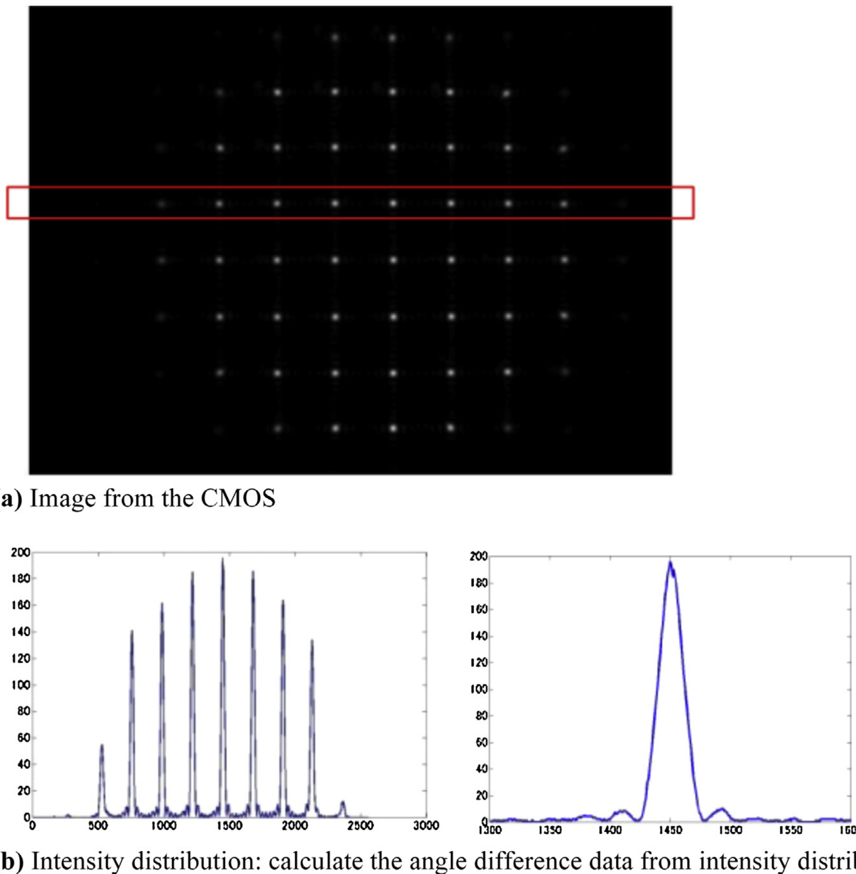

Fig. 10. Image from the CMOS.

Table 2
Experimental conditions.

Parameters	Values
Diameter of cylinder	20 mm
Sample points	360
Rotation angle of one point	1 degree
Measuring time	14 min

angle difference was slight because it eliminated influence of thermal drift. Here, only the characteristics of the differential output to measure the roundness will be investigated.

Assuming that the value of o_x is 1 μm, t is 2000 as, and R is 10 mm. From Eq. (11), we can calculate the $(c_a - c_b)$ to be 2 μrad in the experimental condition. The experimental results also confirmed that the angle difference value Δc reached the same level with random angle error.

From the stability testing results, we note that a simple optical-path design enables the proposed setup to be insensitive to environmental vibration.

4.3. Pre-experiment results

Table 2 shows the experimental conditions. Fig. 12 shows the angle data c_a and c_b by MBAS system. The horizontal axis is the rotation angle and the vertical axis is the angle data.

Measured results presented in Fig. 13 shows the roundness on average of four times was 2.26 μm with standard deviation 0.027 μm.

To evaluate the developed methodology based on the MBAS method on real datasets, an experiment was developed using conventional high-precision machines (KOSAKA EC1550) for roundness assessment. Here, the roundness measurement accuracy of EC1550 is 0.02 μm. Fig. 14 shows the roundness measurement of two separate measurement methods. The roundness for the MBAS method and radius method are 2.26 μm and 2.16 μm, respectively. The roundness test with MBAS system was performed in a circumstance without any temperature control or vibration isolation. Therefore, the influence of circumstance may be one reason to the differential output of two methods.

The pre-experiment results confirm the feasibility of the MBAS for roundness measurement. In the future, we still need to analyze factors influencing measurement accuracy and find measures adopted for evaluating and calibrating the MBAS.

4.4. Simulation of sensitivity error of the MBAS

To confirm the effectiveness of the sensitivity error of the sensor, numerical simulations were performed. Table 3 shows the simulation conditions. Supposing a random angle error of 2.4 μrad, where roundness is 2.2 μm, Fig. 15 shows a simulation example with

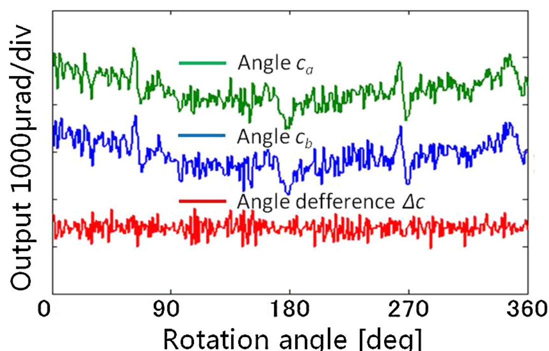

Fig. 12. Measured angle data at points A and B and angle difference data.

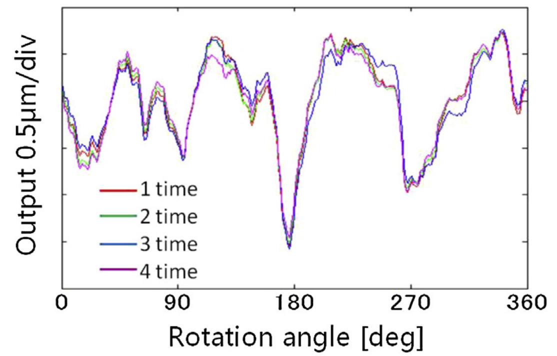

(a) Profile data (four trials)

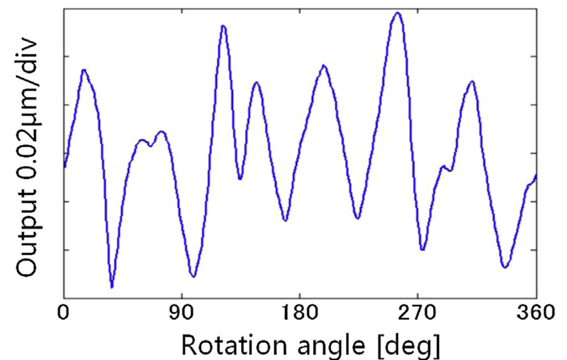

(b) Repeatability (STD)

Fig. 13. Profile data and repeatability for a cylinder measured by the MBAS.

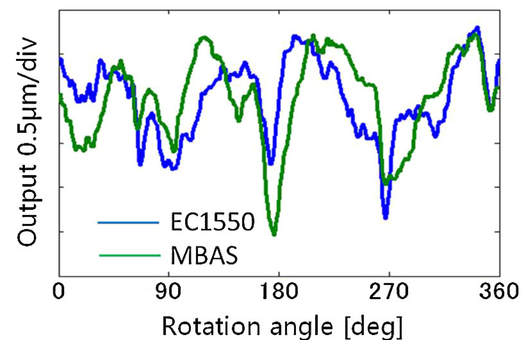

Fig. 14. Comparison with the radius method.

similar conditions as those of the pre-experiment. During 10 simulations, we obtained roundness measurements with repeatability around 0.03 μm (see Fig. 15). Despite the simplicity of the proposed method, the simulated results agree well with experimental data.

Under similar experimental conditions, the standard deviation of repeatability is proportional to the random value. The simulation result implies that this system can measure roundness with repeatability under 10 nm if the random angle error is less than

Table 3
Simulation conditions.

Parameters	Values
Diameter of cylinder	20 mm
Sample points	360
Roundness	2.2 μm
Random angle error	2.4 μrad

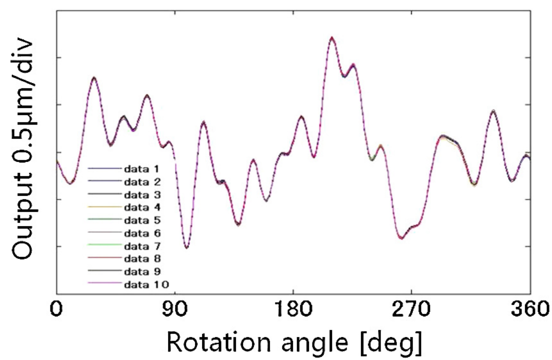

Fig. 15. Sensitivity of the sensor (10 times).

0.8 μrad. Therefore, a further improvement of measurement accuracy could be achieved by reducing the random error of MBAS.

5. Conclusions

The results of this paper are summarized as follows:

(1) A high accuracy micro roundness measuring machine (micro-RMM) for accurately measurement the roundness profiles has been proposed in this paper. The schematic of the micro-RMM includes three main parts: a multi-beam angle sensor (MBAS), a rotary unit, and a bearing system. The MBAS has been incorporated in order to improve the motion accuracy of the micro-RMM. Compared with other methods, the MBAS is less susceptible to instrumental errors for angle detection, can maintain high sensitivity with a miniaturized size, and can be used conveniently at the factory level.

(2) A measurement system for roundness measurement using the MBAS has been constructed. The resolution of the MBAS is 0.05 μrad. The optical probe is based on the principle of an autocollimator and has a stability of 2.35 μrad. The roundness in the MBAS method and radius method are 2.26 μm and 2.16 μm, respectively. It can be seen that the standard deviation is approximately 0.17 μm. Experimental results confirm feasibility of the MBAS for roundness measurement are also presented.

(3) To confirm the effectiveness of the sensitivity error of the sensor, numerical simulations were performed with conditions similar to those of the experiment. Despite the simplicity of the proposed method, the simulated results agree well with experimental data. In a similar condition of the experiment, the standard deviation of repeatability is proportional to the random angle error. The simulation result implies that the proposed system can measure roundness with repeatability under 10 nm if stability of the angle difference value is less than 0.8 μrad.

As mentioned previously, the scatter plot in CMOS presents eight lines by eight columns. We use one line spots to measure the roundness. In the future, our instrument will measure not only roundness, but also axial form or vertical straightness, dimensional uniformity or parallelism by using the spots in axial direction.

We also plan to calibrate the autocollimator by analyzing factors influencing measurement accuracy or by finding measures adopted for high-speed measurement. A new experiment has been designed, which is planned to be conducted in the near future in order to implement the improvements.

References

[1] Chetwynd DG, Siddall GJ. Improving the accuracy of roundness measurement. J Phys E: Sci Instrum 1976;9(7):537–44.
[2] Whitehouse DJ. Some theoretical aspects of error separation techniques in surface metrology. J Phys E: Sci Instrum 1976;9:531–6.
[3] Shimizu Y, Goto S, Lee JC, Ito S, Gao W, Adachi S, et al. Fabrication of large-size SiC mirror with precision aspheric profile for artificial satellite. Precis Eng 2013;37:640–9.
[4] Vissiere A, Nouira H, Damak M, Gibaru O, David JM. A newly conceived cylinder measuring machine and methods that eliminate the spindle errors. Meas Sci Technol 2012;23(9):094015.
[5] Bernstein J, Weckenmann A. Measurement uncertainty evaluation of optical multi-sensor-measurements. Measurement 2012;45:2309–20.
[6] Mekid S, Vacharanukul K. In-process out-of-roundness measurement probe for turned workpieces. Measurement 2011;44:762–6.
[7] Gao W, Kiyono S. On-machine roundness measurement of cylindrical workpieces by the combined three-point method. Measurement 1997;21:147–56.
[8] Gleason E, Schwenket H. A spindleless instrument for the roundness measurement of precision spheres. Precis Eng 1998;22:37–42.
[9] Marsh E, Couey J, Vallance R. Roundness measurement of spherical artifacts at arbitrary latitude. Precis Eng 2006;30:353–6.
[10] Gao W, Huang PS, Yamada T, Kiyono S. A compact and sensitive two-dimensional angle probe for flatness measurement of large silicon wafers. Precis Eng 2002;26:396–404.
[11] Teimel A. Technology and applications of grating interferometers in high-precision measurement. Precis Eng 1992;14:147–54.
[12] Whitehouse DJ. Surface metrology. Meas Sci Technol 1997;8:955–72.
[13] Muralikrishnan B, Venkatachalam S, Raja J, Malburg M. A note on the three-point method for roundness measurement. Precis Eng 2005;29:257–60.
[14] Horikawa O, Maruyama N, Shimada M. A low cost, high accuracy roundness measuring system. Precis Eng 2001;25:200–5.
[15] Gao W, Tano M, Sato S, Kiyono S. On-machine measurement of a cylindrical surface with sinusoidal micro-structures by an optical slope sensor. Precis Eng 2006;30:274–9.
[16] Estler WT, Evans CJ, Shao LZ. Uncertainty estimation for multiposition form error metrology. Precis Eng 1997;21:72–82.
[17] Zeng L, Matsumoto H, Kawachi K. Multi-point dynamic displacement probe that uses a self-focusing microlens array. Opt Eng 1997;36:1361–6.
[18] Horikawa O, Sato K, Shimokohbe A. Roundness and absolute radial motion accuracy measurement by an improved reversal method. J Jpn Soc Precis Eng 1991;57:2231–6.
[19] Ueda S, Chen M, Takahashi S, Takamasu K. Roundness measurement of a cylindrical surface by a multi-beam angle sensor (1st report: Measurement method and verification scheme). In: 2014 JSPE spring conference. 2014.
[20] Smith GT. Industrial metrology: surfaces and roundness. London: Springer; 1993.
[21] Chen M, Ueda S, Miyazaki G, Takahashi S, Takamasu K. Roundness measurement of a cylindrical surface by a multi-beam angle sensor (2nd report: experimental verification and calibration of multi-beam angle sensor). In: 2014 JSPE autumn conference. 2014.

Paper:

Automatic Recording Absolute Length-Measuring System with Fast Optical-Comb Fiber Interferometer

Hirokazu Matsumoto*, and Kiyoshi Takamasu***

*Department of Precision Engineering, The University of Tokyo
7-3-1 Hongo, Bunkyo, Tokyo 113-8656, Japan
E-mail: hi.matsumoto@nanolab.t.u-tokyo.ac.jp
**Tokyo Seimitsu Co., Ltd.
4 Higashinakanuki-machi, Tsuchiura, Ibaraki 300-0006, Japan
[Received March 20, 2015; accepted April 13, 2015]

The optical frequency comb has a short pulse, broad spectra, many spectral lines, and high temporal coherency. In this paper, a new absolute length-measuring technique with a high resolution of 0.05 μm is developed by using the temporal-coherence interferometry of the optical comb. A new fiber Fabry-Perot etalon (etalon) of a free spectral range with a frequency of 15 GHz is developed to improve fine positioning in space, so a short translation stage of up to a 10 mm movement is realized for various ranges of length. Moreover, the interference fringe peak is automatically detected by developing a new analog electrical circuit. The ambiguity of the interference-fringe orders is determined by using the etalon at a frequency 14.9 GHz within a time of 1 second for various length ranges.

Keywords: length measurement, high repetition frequency, optical comb, absolute metrology

1. Introduction

In the field of length/distance metrology, precision and then efficiency of measurement are the current demands. The manufacturing industry in particular requires ultimate precision of measurement for the production of high-quality products, and precise measurements are also important in the assessment of safety in society. For example, it is vitally important that the shape and form of aircraft and engines be absolutely measured with the utmost precision. Under such circumstances, studies have long been carried out using a continuous wave (CW) laser interferometers or pulse lasers, but the use of such technology is restricted to special applications. Recently, ultra-short, optical, new pulse generation has become significant, and broad-band spectra are being utilized again. The development of femtosecond mode-locked laser technology has been particularly rapid. In addition, high-speed optical communication technology has also been studied. With the advent of photonic crystal fiber, mode-locked pulse laser technology has become very attractive in the field of optical metrology, and the laser has come to be called an "optical frequency comb," or "optical comb." The optical comb has various useful characteristics.

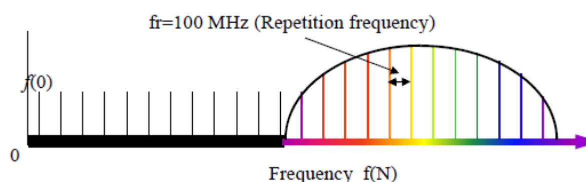

Fig. 1. Outline of optical frequency comb. $f(N) = f(0) + N \cdot f_r$ $(N : \text{integer})$.

Here, we report the results of experimental investigations done on a new, highly accurate method of measuring absolute length using the pulse interference of the optical comb. The technique uses only the temporal coherence (pulse) interferometry of the optical comb, so the measuring system is simple and very accurate. It is therefore useful for absolute length measurements with an accuracy of 0.05 μm for measurements of up to several hundred meters.

2. Optical Frequency Comb

2.1. Outline of Optical Frequency Comb

The optical frequency comb has many narrow spectral lines in equal frequency intervals in the frequency domain, as shown in **Fig. 1**. However, there is sometimes carrier envelop offset frequency, and it is not easy to control. On the other hand, in the time domain, the laser is a pulse train with very short pulse width, and the intervals are precisely constant. The time interval is easily stabilized to frequency standards, such as a rubidium optical clock system. The stability of the time interval is very good, with an accuracy equivalent to 10^{-11} [1]. Moreover, for industrial metrology in various factories, the optical comb with an all optical fiber system has been found to be profitable, because it was not strongly affected by the surrounding condition.

The principle of position measurement using temporal-

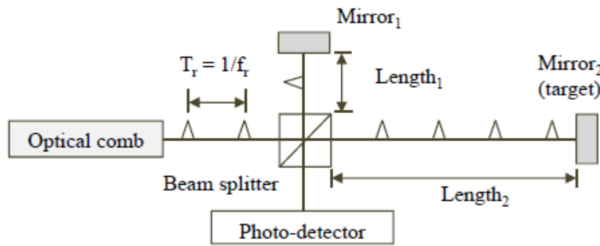

Fig. 2. Temporal coherence interferometry using the repetition f_r of optical pulses(T_r; time interval).

coherence interferometry is shown in **Fig. 2**. Interference fringes are generated when the difference between the measurement path length L_1 and the reference path length L_2 is $mc/2f_r$. Here, m is an integer, c is the speed of light through air, and f_r is the repetition frequency of the optical comb used [2]. The interference is generated in the range of length of several tens of micrometers in space, depending on the pulse width of the optical comb. This technique is very useful for various types of positioning with a high spatial accuracy because the f_r has an accuracy of more than 10^{-11}. In general, the technique is useful for absolute distance measurement, and distance measurement with a high reproducibility of several μm has been realized at about 403 m in general industrial fields [3–5]. Therefore, temporal coherence interferometry has proven useful for measuring lengths in industry and society, because it is not affected by air turbulence and mechanical vibration due to its ultra-short pulse characteristics.

Therefore, the optical comb offers an absolute measuring system using a simple system for in-situ metrology and temporal coherence interferometry which does not utilize the carrier envelop offset frequency control. It has a wide range of measurement from 0 to several hundred meters. However, the interference fringes generated are limited to the distance region of each 1.5 m time m in the case of a 100 MHz repetition frequency, so more than 1.5 m of the translation stage must be scanned for generating the interference fringe.

2.2. Fast Optical Frequency Comb

In general, the repetition frequency that optical combs can produce relatively easily is in the frequency range of 40–150 MHz because the optical fiber is relatively long for laser oscillation. Temporal coherence interference fringe is therefore generated at spatial positions of intervals longer than 1 m. Consequently, the length fields that can be used in measurements in industry and society may be limited to special isolated measurements. Therefore, it is important to develop a high-frequency repetition (fast) optical comb. For realizing this resolution, a new fiber-type Fabry-Perot etalon (etalon) has been developed for increasing the repetition frequency of optical comb from around 100 MHz to around 10 GHz. Fortunately, since the optical comb has a discrete spectrum, a high-accuracy length of etalon is not required.

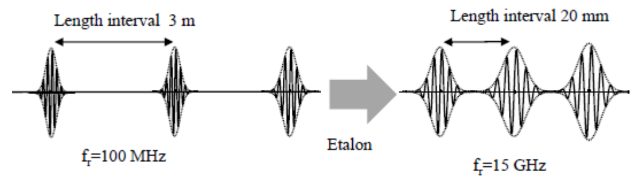

Fig. 3. High frequency comb produced by filtering with Fabry-Perot etalon.

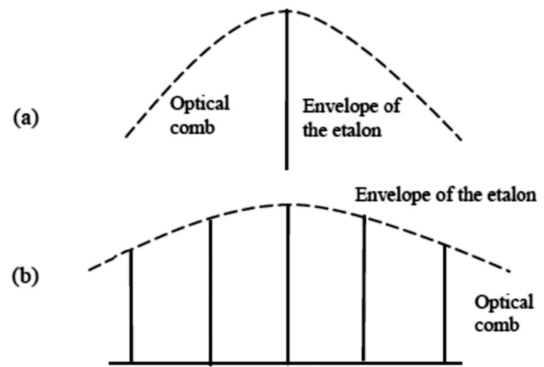

Fig. 4. Filtering of optical comb; (a) high-finesse etalon, (b) low-finesse etalon.

An optical fiber-type etalon has been developed, as shown in **Fig. 3**, because the fiber-optic etalon is not strongly affected by variations in air temperature or mechanical vibrations. Since the free spectral range is not required to be accurate, the length of the etalon cavity fiber (device) is cut according to the free spectral range required and is sometimes sandwiched between the general optical fibers with the reflective coating and the FC/PC connectors. In this case, one optical line should be selected by the etalon of high finesse, but the power of the light is reduced, as shown in **Fig. 4(a)**. The accuracy of the fast optical comb is the same as that of the original optical comb, which has a repetition frequency of 100 MHz. On the other hand, if we use the etalon of low finesse, the power is not largely reduced, but several lines are selected similar to multi-mode He-Ne gas lasers, and the selected optical comb laser is similar to those of multi-mode gas lasers as shown in **Fig. 4(b)**. In this case, the accuracy of the repetition frequency is dependent on the length of the etalons used. We can easily suppose that the length stability of the etalon is better than about 0.5 ppm, as that of the multi-mode He-Ne laser [6]. Finally, etalons with free spectral ranges of 15.0 GHz and 14.9 GHz have been developed by polishing the length of a ferrule fiber device. The length is measured by using a low coherence interferometer in polishing process. In this case of 15 GHz, the geometrical length of device is 6.8063 mm, because the group refractive index of the optical fiber is 1.4682. The reflectivity of the etalon fiber has been coated to be 98% (finesse; about 150) by dielectric multilayer coating. Therefore, the etalon reduces the output power of optical comb from about 12 mw to about 0.1 mw, but the SN

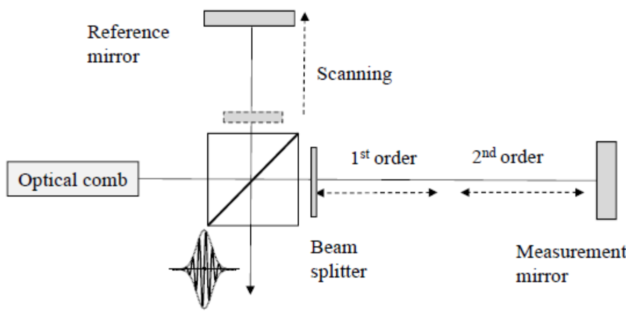

Fig. 5. Interference fringe generation according to the pulse interval.

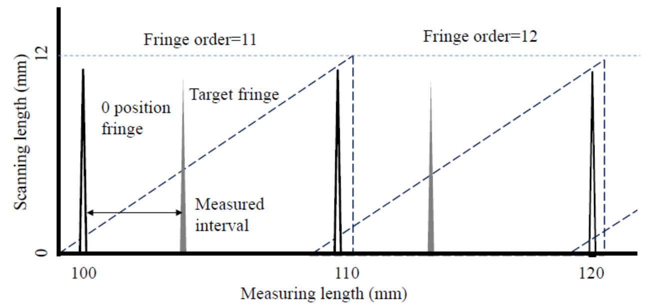

Fig. 6. Measurement principle of absolute distances with high-frequency optical comb.

ratio of interference fringe was no problem in high resolution measurements of about 50 nm. If necessary, we may use an optical fiber amplifier for more-high accuracy measurement.

3. Absolute Ranging Method

3.1. The Principle of Absolute Measurement

In order to form an interference fringe pattern, the reference optical path length must be scanned over several tens of millimeters according to the length of etalon used. For example, in the 1 GHz etalon, the optical spacing of the etalon is 150 mm. Since 1.4682 is the group refractive index of the optical fiber, the size of the etalon free spectral range is about 100 mm. Therefore, the scanning stage must be 150 mm or longer.

We will now discuss the length measurement for using the repetition frequencies of 15.0 GHz and 14.9 GHz. The scanning range of the stage is about 14 mm long. **Fig. 5** shows an outline of the distance measurement with an unbalanced arm interferometer and a scanning stage. To reduce the effect of the drift in the measurement system, the zero-point of each interference fringe order is generated using a window plate, and the detected signal is always displayed at each order. The object mirror is at the position of the target mirror in spatial measurement.

The interference fringes at 0 mm are always generated at the same position by scanning over 14 mm. On the other hand, the interference fringes of the target are generated at every position corresponding to the length being measured within a 14 mm scan. This is because the 15 GHz repetition frequency is equal to the 10 mm interval. **Fig. 6** shows the behavior of interference fringe generation in the length range of 100 mm to 120 mm. In the measurement, the interval between the 0 position signal and the measurement position signal is determined by the displacement of the stage with an accuracy of higher than 0.1 μm. Secondly, the order of the interference fringe is determined by the same measurement by the 14.9 GHz repetition frequency of the comb.

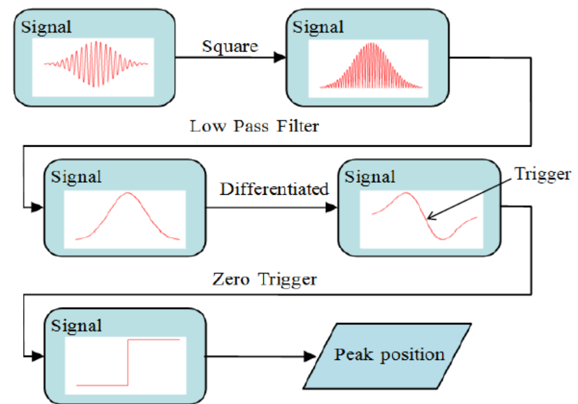

Fig. 7. Interference fringe automatic-processing using an electric circuit.

3.2. Automatic Measurement

Figure 7 shows an outline of the automatic processing of interference fringes for determining the length [7, 8]. First, the photo-detection signal of the interference fringes is squared, and then it is filtered by a low-path filter. The output signal is differentiated by an electrical circuit. Finally, the pulse signal is generated at the zero-crossing position to trigger a short traditional length-measurement sensor with a resolution of 10 nm.

4. Experiment

4.1. Interferometer and its System

The measurement system we have developed is shown in **Fig. 8**. The optical comb is incident to a two-beam interferometer through an etalon and a fiber circulator. About 14 mm of the reference path is scanned because the free spectral range of the etalon used is 15 GHz, which corresponds to about 10 mm in length. The ultrasonic linear stage is used because it is compact. The measurement path has a window plate (0 point) and a reflecting mirror (target). The generated interference fringes are detected by a photodiode and are amplified with a high SN ratio by a frequency selective amplifier. The SN ratio of the final signal is high enough for automatic measurements.

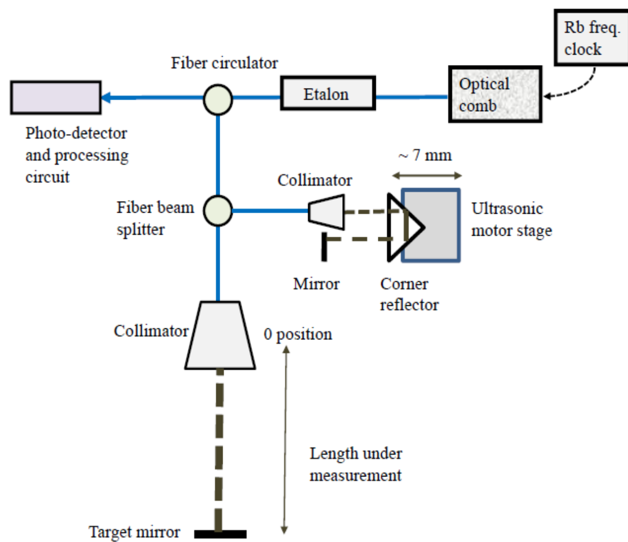

Fig. 8. Temporal coherence interferometer for absolute length measurements.

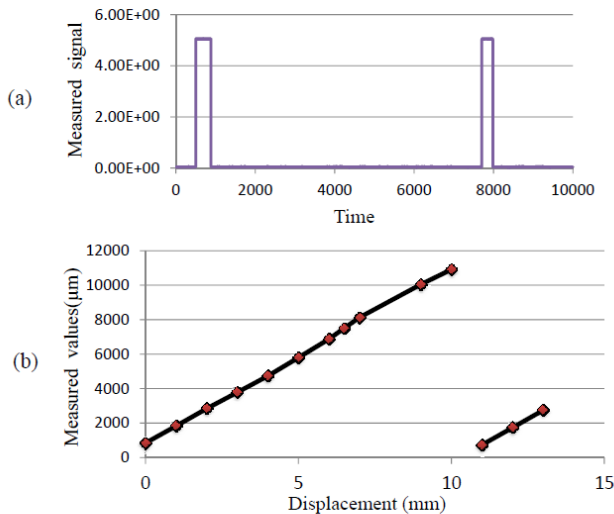

Fig. 9. Results of the experiment.

4.2. Results

With our new system, the length/distance measurements were preliminary achieved; the results of the experiment are shown in **Fig. 9**. **Fig. 9(a)** shows the processed signal for the triggering of measurements, and **Fig. 9(b)** shows the results of the measurements. The standard deviation of the measured values is less than 0.05 μm, though the accuracy of displacement is relatively poor because the micrometer was operated by manual operation. Moreover, higher-reliability measurements has been achieved by taking the average of several measurements. The result shows that the new system may be able to measure lengths or distances of up to several hundred meters by utilizing various etalons of different free spectral ranges. The total time for taking the overall measurement has been made within several seconds, but it may be improved by using a fast scanning stage.

4.3. Discussion

As indicated above, the present measurement system is not much affected by air turbulence or mechanical vibration. However, the resolution is not small, because the peak of the interference fringe pattern is achieved using the effect of the electrical circuit. Since the optical comb of the spectral width of 60 nm is used, the half-width of the fringe pattern is about 20 μm. Considering the SN ratio of the pattern, a measurement resolution of better than 0.05 μm may be expected by using professional software. Therefore, the present system may be useful for measurements of relatively large objects, though it is very useful for measurements of small objects.

5. Conclusion

A new absolute distance-measuring technique with a high resolution of 0.05 μm has been developed using the temporal-coherence interferometry of an optical frequency comb and a short translation stage for various distance ranges. A new fiber Fabry-Perot etalon having the frequency of 15 GHz of the etalon has been developed to improve fine positioning in space. Therefore, the scanning length for generating the temporal coherence interference fringe is only about 14 mm. Moreover, the interference fringe peak has been automatically achieved by developing a new analog electrical circuit.

The present system with an optical comb is applicable to the measurement of lengths up to several hundred meters. It is particularly applicable to industrial metrology because it is not much affected by surrounding conditions.

References:

[1] H. Inaba, Y. Daimon, K. Minoshima, F. Hong, A. Onae, S. R. Thomas, H. Matsumoto, M. Hirano, T. Okuno, M. Onishi, and M. Nakazawa, "Long-term Measurement of Optical Frequencies Using Simple, Robust, and Low-noise Fiber Based Frequency Comb," Optics Express, Vol.14, No.12, pp. 5223-5231, 2006.

[2] H. Matsumoto, "Measurement Standard and Traceability," Optics, Vol.39, No.3, p. 114, 2010.

[3] Y. Yamaoka, K. Minoshima, and H. Matsumoto, "Direct Measurement of the Group Refractive Index of Air with interferometry between Adjacent Femtosecond Pulses," Appl. Opt., Vol.41, pp. 4318-4324, 2002.

[4] X. Wang, S. Takahashi, K. Takamasu, and H. Matsumoto, "Space position measurement using long-path heterodyne interferometer with optical frequency comb," Opt. Express, Vol.20, pp. 2725-2732, 2012.

[5] H. Matsumoto, X. Wang, K. Takamasu, and T. Aoto, "Absolute Measurement of Baselines up to 403 m Using Heterodyne Temporal Coherence Interferometer with Optical Frequency Comb," Appl. Phys. Express, Vol.5, p. 046601, 2012.

[6] N. Chanthawong, S. Takahashi, K. Takamasu, and H. Matsumoto, "A new method for high-accuracy gauge block measurement 2 GHz repetition mode of a mode-locked fiber laser," Meas. Sci. Technol., Vol.23, p. 054003, 2012.

[7] H. Matsumoto, S. Seino, and Y. Sakurai, "Automatic Recording Laser Interferometer for Line Standards up to 2 m," metrologia, Vol.16, pp. 169-175, 1980.

[8] N. Ohsawa, H. Matsumoto, A. Hirai, T. Shimizu, and T. Kikuchi, "Non-Contact Remote Measurements of Ring Gauge Using a Low-Coherence Interferometer," 10th Int. Symposium on Measurement and Quality Control, 2010.

Name:
Hirokazu Matsumoto

Affiliation:
Project Researcher, Department of Precision Engineering, The University of Tokyo
Director, Tokyo Seimitsu Co., Ltd.

Address:
7-3-1, Hongo, Bunkyo-ku, Tokyo 113-8656, Japan

Brief Biographical History:
1976- Joined National Research Laboratory of Metrology
2001- National Metrology Institute, National Institute of Advanced Industrial Science and Technology (AIST)
2008- The University of Tokyo

Main Works:
• Optical length standard metrology, Interferometric measurement of industrial products, Non-linear optics

Membership in Academic Societies:
• Japan Society of Applied Physics (JSAP)
• Japan Society for Precision Engineering (JSPE)

Name:
Kiyoshi Takamasu

Affiliation:
Professor, Department of Precision Engineering, School of Engineering, The University of Tokyo

Address:
7-3-1 Hongo, Bunkyo-ku, Tokyo 113-8656, Japan

Brief Biographical History:
1982-1985 Research Associate, Department of Precision Engineering, The University of Tokyo
1985-1993 Lecturer, Tokyo Denki University
1993-2002 Associate Professor, Department of Precision Engineering, The University of Tokyo
2002- Professor, Department of Precision Engineering, The University of Tokyo

Main Works:
• K. Ishikawa, T. Takamura, M. Xiao, S. Takahashi, and K. Takamasu, "Profile measurement of aspheric surfaces using scanning deflectometry and rotating autocollimator with wide measuring range," Measurement Science and Technology, Vol.25, p. 064008, 2014.
• M. Chen, S. Takahashi, and K. Takamasu, "Development of high-precision micro-roundness measuring machine using a high-sensitivity and compact multi-beam angle sensor," Precision Engineering, Vol.42, pp. 276-282, 2015.

Membership in Academic Societies:
• The European Society for Precision Engineering and Nanotechnology (euspen)
• Japan Society for Precision Engineering (JSPE)

Measurement 78 (2016) 381–387

Contents lists available at ScienceDirect

Measurement

journal homepage: www.elsevier.com/locate/measurement

Non-contact measurement technique for dimensional metrology using optical comb

Wiroj Sudatham [a,*], Hirokazu Matsumoto [a], Satoru Takahashi [b], Kiyoshi Takamasu [a]

[a] *Department of Precision Engineering, The University of Tokyo, Hongo 7-3-1 Bunkyo, Tokyo 113-8656, Japan*
[b] *Research Center for Advanced Science and Technology, The University of Tokyo, Komaba 4-6-1, Meguro, Tokyo 153-8904, Japan*

ARTICLE INFO

Article history:
Received 6 February 2015
Received in revised form 16 July 2015
Accepted 22 July 2015
Available online 8 August 2015

Keywords:
Non-contact measurement
Pulse interferometer
Absolute length measurement
Dimensional metrology

ABSTRACT

This paper proposes a non-contact pulsed interferometer for dimensional metrology using the repetition frequency of an optical frequency comb. A compact absolute-length measuring system is established for practical non-contact measurement based on a single-mode fiber interferometer. The stability and accuracy of the measurements are compared with those from a commercial incremental laser interferometer. The drifts of both systems have the same tendency and a maximum difference is approximately 0.1 μm. Subsequently, preliminary absolute-length measurements up to 1.5 m were measured. The signal-to-noise ratios of the small signals are improved by a frequency-selective amplifier. It is apparent that the noise is rejected, and the intensity of the interference fringes is amplified, achieving a maximum standard deviation of measurement approximately 1 μm. The proposed technique can provide sufficient accuracy for non-contact measurement in applications such as a simple laser-pulse tracking system.

© 2015 Elsevier Ltd. All rights reserved.

1. Introduction

Recently, demand for high-accuracy measurement for dimensional metrology has increased rapidly. To respond to this requirement, many applications using an optical frequency comb were developed for absolute-length measurements because optical frequency combs have very high accuracy and a high stability of their frequencies. However, those applications, the measuring systems and the optical components are different [1–7].

This paper presents an optical comb application for absolute-length measurement using a single-mode fiber pulsed interferometer technique, which an optical comb is used as the laser source. A repetition frequency of 100 MHz of a general optical frequency comb is transferred to 1 GHz by a fiber type Fabry-Pérot etalon. The stability of the pulsed interferometer is considered because it is a factor that reflects the reliability of the measurement system versus changes in ambient environmental conditions. The experimental results are compared to measurements obtained with a commercial incremental interferometer. The drifts of both interferometer types are considered in a laboratory without control of air temperature and humidity. Subsequently, a metal ball with a rough surface is used as a target of the interferometer to obtain the length under measurement because the rough metal ball mainly reflects the laser beam to the single-mode fiber interferometer. It is easy to align the laser beam, and this setup also provides three-dimensional target positions. The surface roughness of the metal ball targets is analyzed because it directly influences the envelope inference fringes. Additionally, the requirement of a laser-beam alignment is considered. Finally, a preliminary absolute-length measurement up to 1500 mm was measured by an optical-comb pulsed interferometer, in which a rough metal ball is used as the target. A phase-sensitive analyzing method is used to obtain envelope interference fringes, and

* Corresponding author. Tel./fax: +81 3 5841 6472.
E-mail address: wiroj@nanolab.t.u-tokyo.ac.jp (W. Sudatham).

http://dx.doi.org/10.1016/j.measurement.2015.07.053
0263-2241/© 2015 Elsevier Ltd. All rights reserved.

the measurement results are compensated for the group refractive index of air [8,9] owing to changes in environmental conditions. The proposed measuring system can possibly be used to develop a length-measuring tracking system, and can be applied to verify the coordinate measuring machine (CMM) by the multilateration measurement method [10,11].

2. Measurement principle

2.1. Optical frequency comb

Generally, a laser does not have only one wavelength or frequency, but has some natural bandwidth that is related to the gain medium and the optical cavity. In the optical cavity, the light waves will constructively and destructively interfere with themselves, becoming a formation of standing waves. The discrete sets of frequencies of standing waves are called longitudinal modes. These modes are the only frequencies of light that is allowed to oscillate by the resonant cavity and to oscillate independently. The output of a laser has several thousands of modes. Thus, the output intensity will become nearly constant; this is known as a continuous wave, or cw. If all of the modes of a cw laser are fixed in phase relationship, the lasers will periodically interfere with one another. As a result, the laser produces pulse trains of light and it is said to be mode-locked. Mode-locked lasers generate repetitive, ultrashort optical pulse trains by fixing the relative phases of all of the lasing longitudinal modes [12–15]. These pulses are separated in time that is given by Eq. (1).

$$\tau = \frac{2L}{c} \tag{1}$$

where L is the length of the optical cavity and c is the speed of light in vacuum. Therefore, the mode spacing of the laser will be

$$\Delta\upsilon = \frac{1}{\tau} \tag{2}$$

For that reason, the spectrum of each pulse train is separated by the repetition rate of the laser, and the spectral lines are called an optical frequency comb.

The time and frequency domains of an optical frequency comb are shown in Fig. 1. In the time domain, the pulse train is emitted by a mode-locked laser in the same time as the pulse-to-pulse separation time, $1/f_{rep}$, where f_{rep} is the repetition frequency of the optical frequency comb. In the frequency domain, each shape line is separated equally. The optical frequencies f_m of the comb lines is described as $f_m = mf_{rep} + f_0$, where m is a large integer of order 10^6 and f_0 is the offset frequency resulting from the pulse-to-pulse phase shift ($\Delta\phi$).

2.2. Fabry-Pérot Etalon

A Fabry-Pérot Etalon (etalon) is an interferometer in which the beam of a laser undergoes multiple reflections between two reflecting mirrors [16]. The resulting optical transmission is periodic in wavelength. The transmission of the etalon is at a maximum when the phase difference for a round-trip follows Eq. (3):

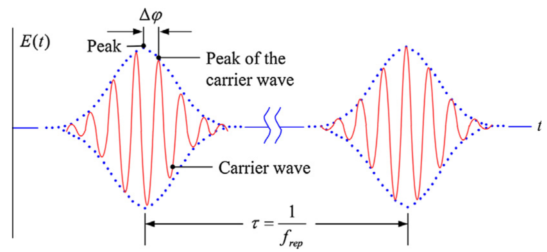

(a) Time domain.

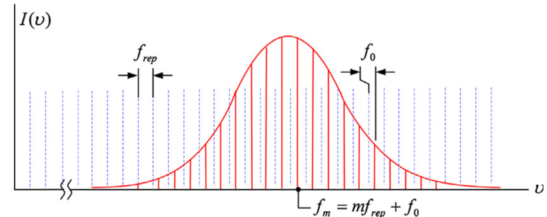

(b) Frequency domain.

Fig. 1. (a) Time domain and (b) frequency domain of an optical frequency comb.

$$\frac{2\pi}{\lambda} 2nl\cos\theta = 2m\pi \tag{3}$$

where l is the cavity length of an etalon, θ is the transmission angle, n is the refractive index of the medium and λ is the laser wavelength. Expressing the maximum condition in terms of frequency, the location of transmission peak locations can be written as follows:

$$\upsilon = m\frac{c}{2nl\cos\theta} \tag{4}$$

Therefore, the frequency separation between successive peaks can be determined. The peak-to-peak frequency separation is called the free spectral range (FSR), and it is given by Eq. (5):

$$\mathrm{FSR} = \Delta\upsilon = \upsilon_{m+1} - \upsilon_m = \frac{c}{2nl\cos\theta} \tag{5}$$

As a result, when an etalon is applied, the repetition frequency of an optical frequency comb is transferred to the high frequency of the FSR. However, the output intensity is reduced when the laser pulse passes through an etalon. Therefore, an optical amplifier is required for some applications.

2.3. Optical comb pulsed interferometer

The diagram of an optical-comb pulsed interferometer is shown in Fig. 2. It is the operating principle of the unbalanced-arm Michelson interferometer. An optical comb generates a pulse train, and the laser pulses are divided into two beams by optical beam splitter (BS). One beam is reflected in the direction of a scanning mirror (M1), while the other is transmitted through a reference position ($OPD = 0$) to a target mirror (M2).

Both reflected light pulses are recombined with the beam that returned from M1 to produce interference fringes when the optical path difference (OPD) of the two arms satisfies the following Eq. (6) [1–3]:

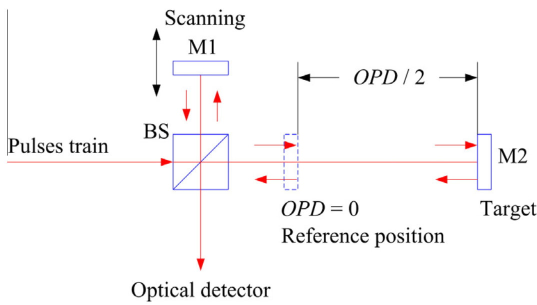

Fig. 2. Principle of an optical-comb pulsed interferometer.

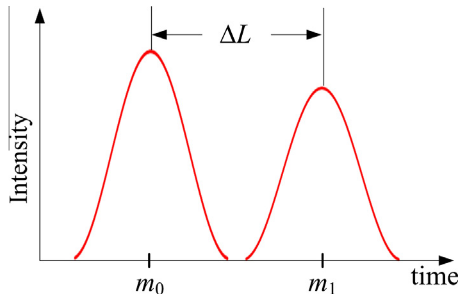

Fig. 3. Envelope interference fringes of the reference position (m_0) and the target (m_1).

$$OPD = \frac{mc}{n_{air} f_{rep}} \tag{6}$$

where m is an integer, n_{air} is the refractive index of air and f_{rep} is the repetition frequency.

Generally, two interference fringes will overlap with each other when observed by an oscilloscope. If the fringes provide a slight displacement (ΔL), the envelope interference fringes will be separated, as shown in Fig. 3. Therefore, the absolute length under measurement is determined as Eq. (7):

$$L = \frac{OPD}{2} + \Delta L \tag{7}$$

In the experiment, two envelope interference fringes are presented in the time domain. Consequently, the relationship between the time scale and length scale must be calibrated to determine the value of ΔL. A linear gauge with a resolution of 10 nm was used to determine this relation. The absolute lengths under measurement also have to compensate for the group refractive index of air owing to the change of environmental conditions by Ciddor's equation [8].

3. Experiments and results

3.1. Stability and accuracy of pulse interferometer

To study measurement stability, a measurement was setup as shown in Fig. 4. An optical-comb pulsed interferometer was paired with an incremental interferometer (Renishaw length-measuring 633 nm, He–Ne laser interferometer).

An optical comb, (C-Fiber femtosecond laser, MenloSystems) was used as the source of laser pulses. The central wavelength is 1560 nm, the output power is 12 mW, and the repetition frequency is 100 MHz, which is stabilized by an Rb-frequency standard. Both measurement systems were prepared in an air-uncontrolled laboratory. Lengths of 150 mm were measured every ten minutes in one hour. The environmental conditions (ambient temperature, relative humidity and air pressure) were also recorded. Then, the drifts of both systems were calculated. The results are illustrated in Fig. 5.

In the experiment, the average value of the ambient temperature, relative humidity, and air pressure were 25.60 °C, 36.5%, and 101.02 kPa; and the maximum variation was approximately 0.2 °C, 1.7% and 10 Pa, respectively. The results in Fig. 5 show that the variations from the average values of both measuring systems have the same drift tendency. The maximum variations of pulse interferometer and incremental interferometer are 0.25 μm and 0.21 μm, respectively. The maximum difference between the two curves is approximately 0.1 μm. Subsequently, the accuracy of the pulse interferometer was considered. According to the incremental interferometer, a comparison requires a long, precise translation stage. The setup diagram for this comparison is shown in Fig. 6(a). Both measuring length systems share the same target to avoid the errors of motion translation, and a photograph of measurement comparison is illustrated in Fig. 6(b).

In the measurement comparison, a precise translation stage was controlled by a resolution of 0.05 μm, which was moved to a position of approximately 150 mm. Subsequently, the length was measured five times by both measuring systems. The environmental conditions were also recorded, to calculate and compensate for the refractive index of air. The measurement results are listed in Table 1.

3.2. Surface roughness and the fringes of target balls

In this experiment, two rough metal ball with a diameter of approximately 25 mm were used to obtain the envelope interference fringes at the reference position ($OPD = 0$). The measurement setup is illustrated in Fig. 7. One ball is smooth, with Ra of approximately 0.1 μm. The other ball is of rough metal, with Ra of approximately 0.2 μm.

The fringes observation in Fig. 8 indicates that the surface roughness of the target affects the quality of the

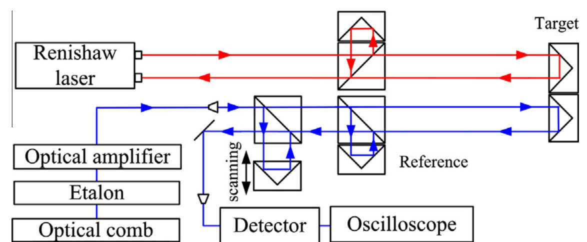

Fig. 4. Measurement setup for study of stability of optical-comb pulsed interferometer compared with an incremental interferometer.

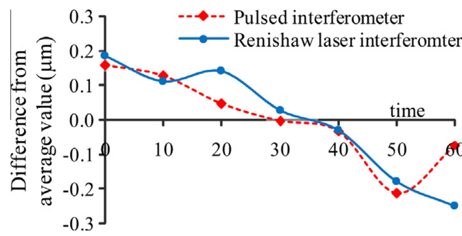

Fig. 5. Measurement stability of pulse interferometer and incremental interferometer.

pattern fringe: a ball with a smooth surface presents a perfect interference fringe, and its intensity is also higher than that of a ball with a rough surface. In addition, if the *Ra* value of the metal ball is higher than 0.2 µm, the interference fringe will disappear because the laser beam cannot reflect to the interferometer system. On the other hand, the intensity of the interference fringe is enhanced if the *Ra* value is better than 0.1 µm. However, aligning the laser beam is not simple if the surface roughness of the metal ball is very smooth ($Ra \ll 0.1$ µm) because the reflected area on the metal ball is too small.

3.3. Preliminary absolute-length measurement up to 1500 mm

The preliminary measurement setup diagram of the pulsed interferometer with a metal ball target is shown in Fig. 9. According to the measurement results in Section 3.2, a metal ball with *Ra* approximately 0.1 µm was selected as the target. The ball was moved by 150 mm in each position. Each length was measured 10 times to determine the repeatability of the measurement. In this experiment, although an etalon plays the role of frequency-mode selector, laser power is reduced. In addition, the surface roughness of the target also affects the laser beam that returns to the interferometer. It is very difficult to detect an interference signal by using only a simple optical detector. Consequently, a frequency-selective amplifier was used to amplify a small interference signal. Noise was also rejected by this technique. Fig. 10 shows the results of the measurement.

The measurement performance of the proposed technique was evaluated by the repeatability of the measurement of each position. The maximum standard deviation is approximately 1 µm for the absolute length up to 1.5 m. However, the results were measured in an air-uncontrolled laboratory, and the environmental conditions swing between (19.9–22.3) °C, (23.7–28.4) %RH, and (99.7–100.9) kPa for the ambient temperature, air humidity, and air pressure, respectively.

4. Discussion

The stability of an optical-comb pulsed interferometer causes an error in length measurement owing to changes in the refractive index of air. The drift of measurement

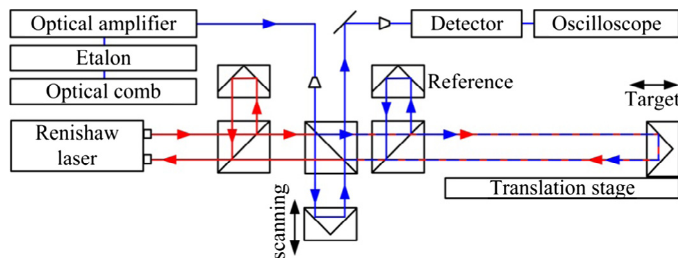

(a) Comparison setup of optical-comb pulsed interferometer and incremental laser interferometer

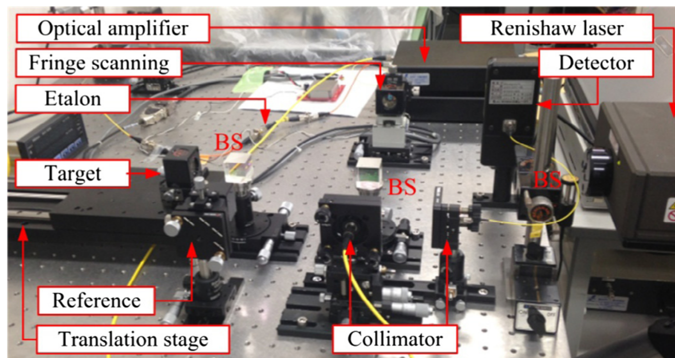

(b) Photograph of measurement comparison.

Fig. 6. (a) Comparison setup diagram, (b) photograph of comparison between optical-comb pulsed interferometer and incremental laser interferometer.

Table 1
Measurement results.

Average of environmental conditions			
	101.02 kPa	25.60 °C	36.5 %RH
No.	Pulsed interferometer (mm)	Incremental interferometer (mm)	Difference (μm)
1	149.85692	149.85689	0.03
2	149.85693	149.85694	−0.01
3	149.85692	149.85682	0.09
4	149.85692	149.85689	0.03
5	149.85693	149.85710	−0.18
SD	0.01	0.10	μm

SD: Measurement standard deviation.

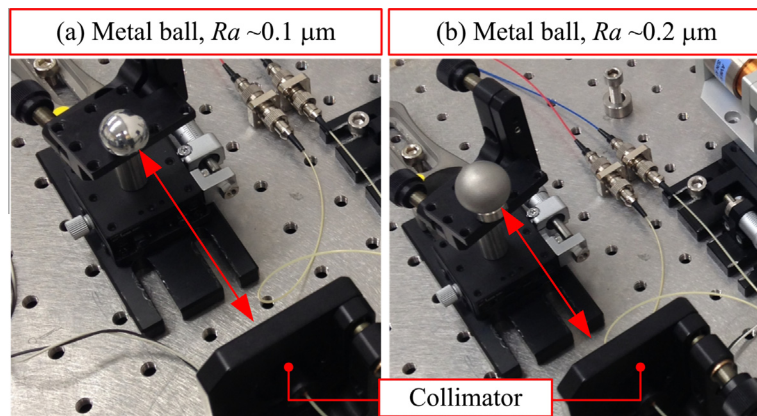

Fig. 7. Optical-comb pulsed interferometer setup with targets at the reference position of measurement: (a) ball is smooth, with *Ra* of approximately 0.1 μm, and (b) ball is of rough metal, with *Ra* of approximately 0.2 μm.

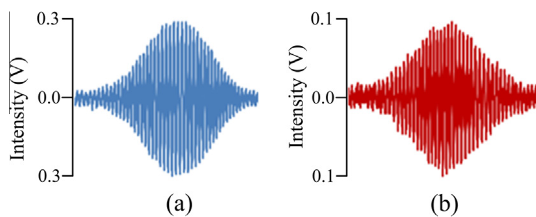

Fig. 8. Interference fringes of (a) a smooth surface, $Ra \sim 0.1$ μm, and (b) a rough surface, $Ra \sim 0.2$ μm of metal ball targets.

was approximately 0.25 μm in one hour. This result shows that the drift was mainly caused by changes in the environmental conditions, while the noise of interference fringe was caused by air fluctuation and mechanical vibration. This is a source of measurement uncertainty, which should be considered in making a precise measurement. In addition, sensors with higher accuracy are required in order to record a change in environment along the entire optical path for compensation.

The roughness of the surface target is significant to the accuracy of measurement. This roughness directly affects fringe acquisition. A suitable surface of a target is one factor that must be considered for applications with a high-accuracy requirement. Moreover, the roundness and diameter tolerance of the target should also be considered for possible applications. When a metal ball with a diameter of 25 mm is used as the target, a beam misalignment of ±0.2 mm from the center of the ball will cause an error of measuring length of approximately 1 μm. However, the error also depends on the surface roughness, roundness, laser beam diameter, and length of measurement. If some area of the ball's surface is not sufficiently smooth, it will affect the error of measurement. In the experiment, using a focusing beam, the repeatability of measurement was improved over using a small spot beam and a large beam diameter. However, the laser beam will be lost when the ball is moved far away from its position. On the other hand, the laser beam is not lost when using a small spot beam and a large beam diameter, but this presents a large standard deviation.

Although an etalon plays the role of frequency mode selector for this application, the power of the laser is reduced. Therefore, the reference mirror type not only achieves a good transmission but also sufficiently reflects the laser beam to produce reference fringes. In the experiment, a sapphire window plate was selected as a reference position ($m = 0$) because its transmission property is appropriate for a laser wavelength in the range of

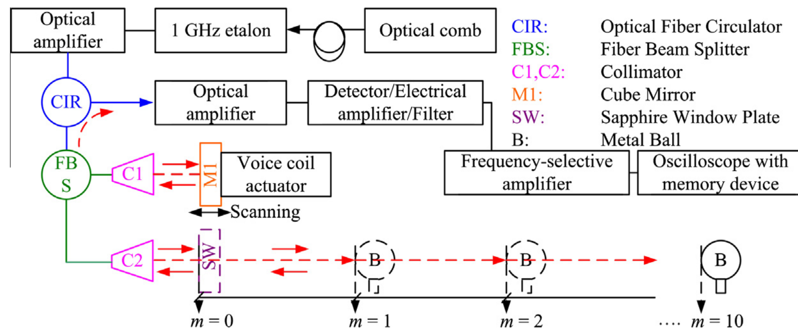

Fig. 9. Measurement set up diagram for absolute length measurement.

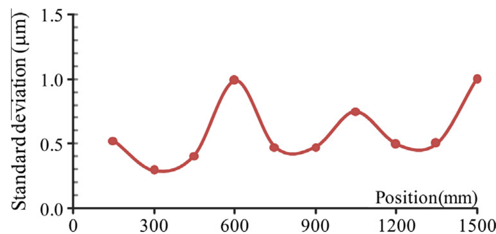

Fig. 10. Measurement results of the absolute length up to 1500 mm.

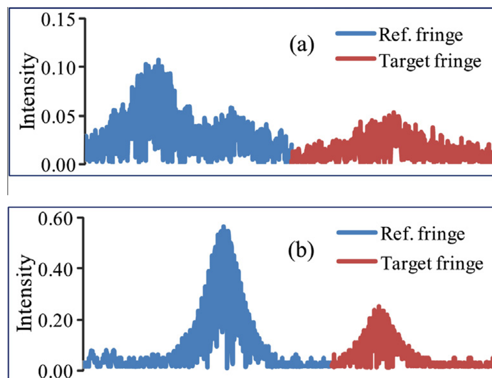

Fig. 11. Interference fringes (a) before and (b) after passing through a frequency-selective amplifier.

1.56 μm. This means the laser power is slightly reduced when the laser passes through a sapphire window plate. Furthermore, an optical amplifier was used to gain the laser power. The interference-fringe signals were amplified by a frequency-selective amplifier. In this case, the phase-sensitive detection method was sufficiently powerful to gain a small signal and reduce noise. Although the power of the laser beam was reduced by an etalon, and the interference fringes were also influenced by the roughness surface of the target, the signal-to-noise ratio of the small signals was improved by a frequency-selective amplifier. It is apparent that the noise is rejected and the interference fringes intensity is amplified, as shown in Fig. 11. Consequently, the interference fringes are captured, and the length observations are also measured.

5. Conclusion

Experiments on absolute-length measurement for dimensional applications have been conducted using an optical-comb pulsed interferometer. The 1-GHz FSR Fabry-Pérot fiber etalon plays the role of a frequency mode selector, and a metal ball is employed as the target of the single-mode fiber interferometer. The measurement accuracy mainly involves the quality of the envelope interference fringes, which correspond to the surface roughness of the target. The drift is mainly sourced from changes in environmental conditions, while the noise of the interference fringe is caused by air fluctuation and mechanical vibration. The stability and accuracy of the measurements are compared with those of a commercial incremental laser interferometer, and the drifts of both systems have the same tendency. The maximum standard deviation is approximately 1 μm for the absolute length measurement up to 1.5 m. The proposed technique can provide sufficient accuracy for non-contact measurement in applications such as a simple laser-pulse tracking system.

References

[1] X. Wang, S. Takahashi, K. Takamasu, H. Matsumoto, Spatial positioning measurements up to 150 m using temporal coherence of optical frequency comb, Prec. Eng. 37 (2013) 635–639.

[2] C. Narin, S. Takahashi, K. Takamasu, H. Mastsumoto, Step gauge measurement using high-frequency repetition of a mode-locked fiber, in: XX IMEKO World Congress, IMEKO2012, Busan, Korea, TC 14-O-19, 2012, pp. 1–5.

[3] H. Matsumoto, X. Wang, K. Takamasu, T. Aoto, Absolute measurement of baselines up to 403 m using heterodyne temporal coherence interferometer with optical frequency comb, Appl. Phys. Exp. 5 (2012) 046601.

[4] P. Balling, P. Křen, P. Mašika, S.A. van den Berg, Femtosecond frequency comb based distance measurement in air, Opt. Exp. 17 (2009) 9300–9313.

[5] S. Hyun, Y.-J. Kim, J. Jin, S.-W. Kim, Absolute length measurement with the frequency comb of a femtosecond laser, Meas. Sci. Technol. 20 (2009).

[6] K. Joo, Y. Kim, S.W. Kim, Distance measurements by combined method based on a femtosecond pulse laser, Opt. Exp. 16 (2008) 19799–19806.

[7] J. Ye, Absolute measurement of a long, arbitrary distance to less than an optical fringe, Opt. Lett. 29 (2004) 1153–1155.

[8] P.E. Ciddor, R.J. Hill, Refractive index of air. 2. Group index, Appl. Opt. 38 (1999) 1663–1667.

[9] Y. Yamaoka, K. Minoshima, H. Matsumoto, Direct Measurement of the group refractive index of air with interferometer between adjacent femtosecond pulse, Appl. Opt. 41 (2002) 4318–4324.

[10] J.J. Aguilar, S. Aguado, J. Santolaria, D. Samper, Multilateration in volumetric verification of machine tool, in: XX IMEKO World Congress, Busan, Republic of Korea, September 9–14, 2012.

[11] W. Klaus, F. Matthias, H. Frank, Measuring large 3D structure using four portable tracking laser interferometer, J. Meas. 45 (2012) 2339–2345.
[12] S.T. Cundiff, J. Ye, Femtosecond optical frequency comb, Rev. Mod. Phys. 75 (2003) 325–342.
[13] D.J. Jones, S.A. Diddams, et al., Carrier-envelope phase control of femtosecond mode-locked laser and direct optical frequency synthesis, J. Sci. 288 (2000) 635–639.
[14] R. Holzwarth, T. Udem, T.W. Hansch, J. Knight, W. Wadsworth, P.S.J. Russell, Optical frequency synthesizer for precision spectroscopy, Phys. Rev. Lett. 85 (2000) 2264–2267.
[15] T. Udem, R. Holzwarth, T.W. Hansch, Optical frequency metrology, Nature 416 (2002) 233–237.
[16] J.M. Yaughan, The Fabry-Perot Interferometer History, Theory, Practice and Applications, Taylor & Francis Group, New York, 1989.

Precision Engineering 43 (2016) 486–492

Contents lists available at ScienceDirect

Precision Engineering

journal homepage: www.elsevier.com/locate/precision

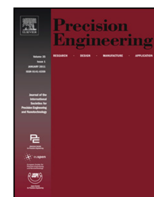

Diagonal in space of coordinate measuring machine verification using an optical-comb pulsed interferometer with a ball-lens target

Wiroj Sudatham [a,*], Hirokazu Matsumoto [a], Satoru Takahashi [b], Kiyoshi Takamasu [a]

[a] *Department of Precision Engineering, The University of Tokyo, Hongo 7-3-1, Bunkyo-ku, Tokyo 113-8656, Japan*
[b] *Research Center for Advanced Science and Technology, The University of Tokyo, Komaba 4-6-1, Meguro, Tokyo 153-8904, Japan*

ARTICLE INFO

Article history:
Received 30 July 2015
Received in revised form 9 September 2015
Accepted 16 September 2015
Available online 30 September 2015

Keywords:
Optical comb
Pulsed interferometer
Length measurement
Coordinate measuring machine
CMM verification

ABSTRACT

This paper presents a new optical method of coordinate measuring machine (CMM) verification. The proposed system based on a single-mode fiber optical-comb pulsed interferometer with a ball lens of refractive index 2 employed as the target. The target can be used for absolute-length measurements in all directions. The laser source is an optical frequency comb, whose repetition rate is stabilized by a rubidium frequency standard. The measurement range is confirmed to be up to 10 m. The diagonals of a CMM are easier to verify by the proposed method than by the conventional artifact test method. The measurement uncertainty of the proposed method is also smaller than that of the conventional method because the proposed measurement system is less affected by air temperature; it achieves an uncertainty of approximately 7 μm for measuring lengths of 10 m. The experimental results show that the measurement accuracy depends on noise in the interference fringe, which arises from airflow fluctuations and mechanical vibrations.

© 2015 Elsevier Inc. All rights reserved.

1. Introduction

Coordinate measuring machines (CMMs) are widely used to measure the three-dimensional sizes, forms, and positions of workpieces. Demonstrating traceability to the International System of Units (SI) and estimating the accuracy of CMM measurements are critical to maintaining confidence in their reliability. Therefore, CMMs must be calibrated upon installation and verified periodically during operation. The main tests required to decide whether the CMM performs to the maximum permissible error of length measurement specified by the manufacturer are detailed in Part 2 of the International Organization for Standardization (ISO) 10360 series [1]. The standard states that five different lengths should be chosen. The longest calibrated test length should be at least 66% of the maximum travel of the CMM. Measurements should be performed in four required positions along the space diagonals shown in Fig. 1, and in three positions parallel to each of the CMM axes. Many methods using calibration artifacts and continuous wave (CW) laser interferometers have been developed to verify CMMs [1–11].

Most methods prefer to use end standards, such as a series of gauge blocks, a step gauge, or a ball plate. However, evaluating large-CMMs (measuring volumes over 2 m^3) has been problematic because of the unavailability of large calibration artifacts. Large calibrated artifacts are difficult to produce because of their size and weight. Calibrating large gauges is difficult, and maintaining gauge accuracy during storage and handling is troublesome [12,13]. Although a CW-laser interferometer can measure long lengths along body diagonals, the measurements can be slow and require difficult laser beam alignment. Moreover, the measurement path cannot be interrupted during the measurement period, because it is operated based on interference fringe counting method.

Recently, optical frequency combs have been proven useful tools for dimensional metrology because of their high frequency-stability and direct traceability to the SI base unit [14]. Several length measurement methods using optical frequency combs have been proposed [15–19]. We developed an optical system for large-size CMM verification that overcomes the problems of conventional artifact test methods. The new system is based on a single-mode fiber optical-comb pulsed interferometer, and uses a ball lens of refractive index 2 as a target. The repetition frequency of a general optical comb is generated, and an optical fiber etalon (Fabry-Pérot fiber etalon) is used as a frequency mode selector to generate interference fringes at the required absolute positions. The performance of long-range measurements was demonstrated by preliminary absolute-length measurements. The proposed system can be used to measure absolute length up to 10 m. The proposed system was used to verify the diagonals of a moving-bridge type CMM in

* Corresponding author. Tel.: +81 3 5841 6472; fax: +81 3 5841 6472.
E-mail address: wiroj@nanolab.t.u-tokyo.ac.jp (W. Sudatham).

http://dx.doi.org/10.1016/j.precisioneng.2015.09.017
0141-6359/© 2015 Elsevier Inc. All rights reserved.

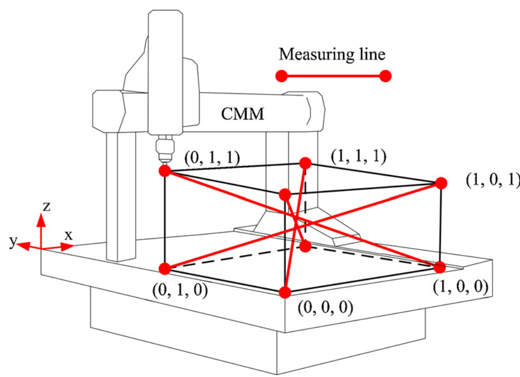

Fig. 1. Measuring lines of the diagonals in space of a CMM; opposite corners of the measuring volume are assumed to be (0, 0, 0) and (1, 1, 1) in coordinates (*X*, *Y*, *Z*).

volume space, as was an artifact test method, for comparison, and the measurement uncertainties of both techniques are discussed.

2. Principle of measurement

The proposed measurement technique is based on a single-mode fiber interferometer, as shown in Fig. 2. An optical comb (C-Fiber femtosecond laser, MenloSystems) with a 1560 nm central wavelength and a 100 MHz repetition frequency stabilized by a rubidium frequency standard generates a laser pulse that passes through a fiber etalon with a free spectral range (FSR) of 1 GHz. An optical amplifier amplifies the laser beam, which then passes through an optical fiber circulator (CIR) to a fiber beam splitter (FBS). One of the resulting split beams is collimated by a collimator (C1) toward a scanning mirror (M1), while the other is collimated by a lens, transmitted through a sapphire window plate (SW) at the reference position before reaching probing target. This second beam acts as measurement arms of a Michelson interferometer.

Subsequently, the beams reflected from the SW at the reference position and the target recombine with the beam reflected from the scanning mirror M1 to generate interference fringes when the optical path differences (*OPD*) between the two arms follow Eq. (1) [16,17].

$$OPD = \frac{mc}{n_{air} f_{rep}} \quad (1)$$

where m is an integer, c is the speed of light in the vacuum, n_{air} is the group refractive index of air [20,21], and f_{rep} is the repetition frequency. The interference fringe signals return to the output port of the CIR and are subsequently detected by a photodetector (2053FC-M, Newport), and observed by an oscilloscope.

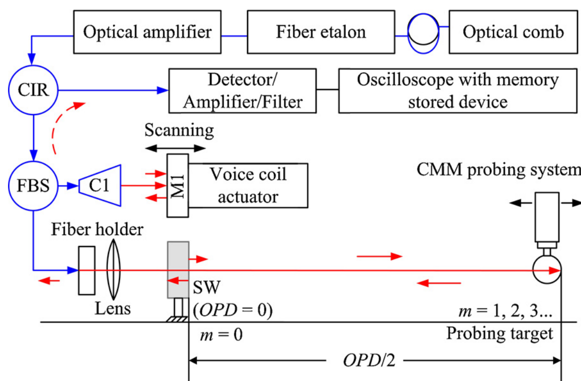

Fig. 2. Diagram of the proposed measurement system; CIR is an optical fiber circulator, FBS is a fiber beam splitter, C1 is a collimator, and SW is a sapphire window plate (reference position). The optical components are connected by optical fibers.

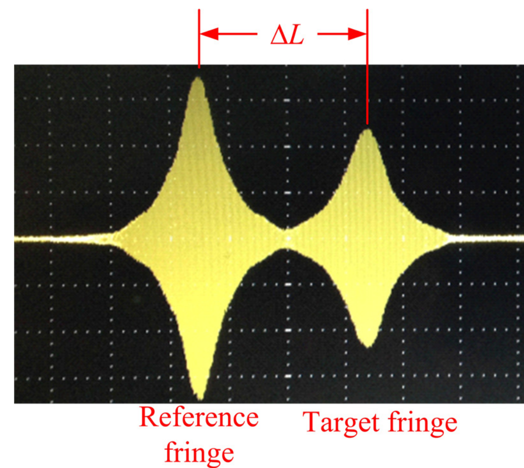

Fig. 3. Interference fringes; the first fringe is produced by reflection of the SW at the reference position. The second is generated by the target.

Two interference fringes overlap with each other when the *OPD* exactly satisfy Eq. (1). In practice, if the measurement length provides a displacement ΔL, the envelope interference fringes will be separated, as shown in Fig. 3.

Therefore, the absolute measurement length is determined by Eq. (2), where ΔL is the distance between the peaks of the interference fringe envelopes.

$$L = \frac{mc}{2n_{air} f_{rep}} + \Delta L \quad (2)$$

The interference fringes of a pulsed interferometer, as shown in Fig. 3, are represented in the time domain. The time scale must be converted to a length scale to determine the distance between the peaks of the interference fringe envelopes, ΔL [18].

3. Experiments and results

3.1. Pulsed interferometer accuracy

The accuracy of the proposed pulsed interferometer was directly evaluated using a standard length of long gauge block. The measurement setup is shown in Fig. 4.

A long gauge block [LGB, 150 mm, grade-0, thermal expansion coefficient $(10.8 \pm 0.5) \times 10^{-6}\,\mathrm{K}^{-1}$] was used as the standard length. The first facet of the LGB was wrung by an optical parallel, and the other was wrung by a short gauge block (GB). The Airy points of the LGB were supported by two pin gauges on a translation stage. The optical components were as described in Fig. 2; the laser beam of an optical comb passed through a fiber etalon and was aligned perpendicular to the optical parallel plate over the travel length of the translation stage. The translation stage was moved until the first interference fringe appeared due to the beam reflected from the inner surface of the optical parallel. The second fringe will automatically arise from the facet of the GB due to the traveling stroke of the scanning device expending the length of the *OPD*. A temperature sensor was attached to the LGB, and a metal sheet covered the measurement setup for more than 24 h to stabilize the temperature of the LGB before measurements were taken. The averages of 10 repeated measurements are shown in Table 1.

The measurements in Table 1 indicate sufficient accuracy of the optical-comb pulsed interferometer for CMM verification.

The precise positions of the interference fringes are very significant to the accuracy of pulsed interferometer, which is used to determine the absolute-length measurement. It relates to the FSR of the fiber etalon, which is proportional to the refractive index of the fiber medium and the length of the fiber cavity. Fabricating a

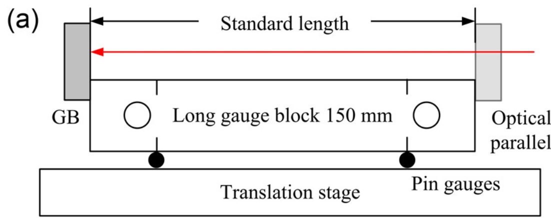

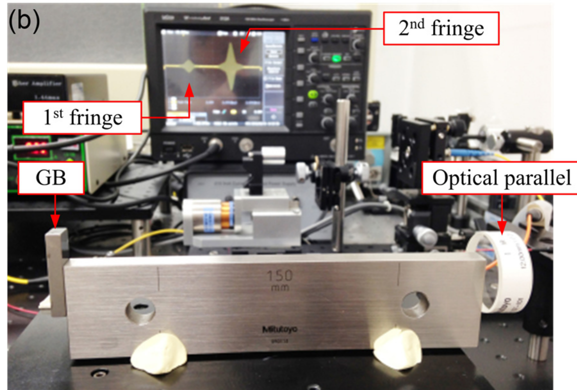

Fig. 4. Measurement comparing the position of interference fringes with a standard length 150 mm long gauge block. (a) Diagram of measurement setup. (b) Photograph of the experimental setup.

Table 1
Accuracy of pulsed interferometer determined by comparison with the length of a standard gauge block.

	T_{LGB} (°C)	ΔL_t (mm)	LGB_t (mm)	Measured value (mm)	Difference (μm)
Average	21.82	0.00294	150.00294	150.00301	−0.07
SD	0.01	0.00002	0.00002	0.00009	–
Variation	0.03	0.00005	0.00005	0.00027	–

T_{LGB} is the gauging temperature of the long gauge block. ΔL_t is the length of thermal expansion. LGB_t is the actual length of the long gauge block at the average temperature of 21.82 °C, and SD is the measurement standard deviation.

preface fiber etalon is difficult because of the inhomogeneous-medium indices of the fiber and coating etalon. The etalon cavity length is also difficult to control, and so must be measured and compensated. The FSR is related to the full-width half-maximum of any one transmission band by a quantity known as the finesse; high finesse fiber etalons are required for this application as they show sharper transmission peaks with lower minimum transmission coefficients [22].

3.2. Ball lens target

We aimed to develop a system that can observe interference fringes in all measurement directions. Therefore, a ball lens (S-LAH79, Ohara) with a refractive index of 2 and a diameter of 10 mm was used as the target of our pulsed interferometer. The back focal length of the ball lens was set to zero. When this ball lens is employed as a target, the entire incoming beam will focus at the ball-lens end surface, as shown in Fig. 5. The reflected beam retraces its incoming path in the opposite direction. Thus, the ball lens functions as a retroreflector [23,24].

The total accuracy of the ball lens target depends on the accuracies of both the refractive index of glass material and the spherical fabrication. The following experiment demonstrates the simplest method to determine the contribution of a ball lens target to optical path error, as shown in Fig. 6.

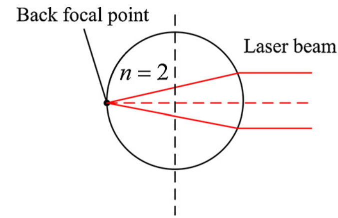

Fig. 5. Structure diagram of the ball-lens target.

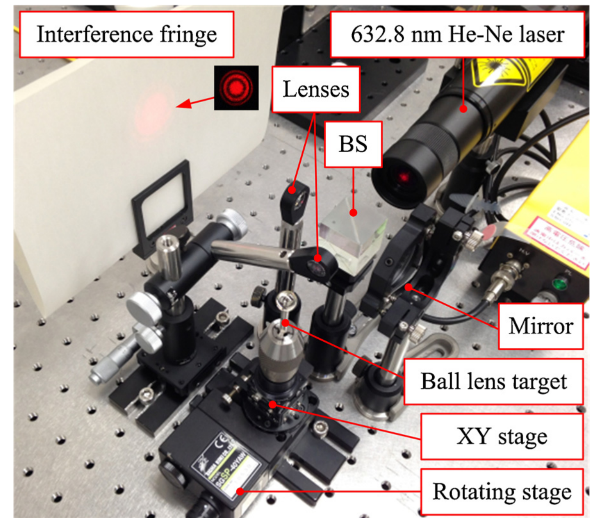

Fig. 6. Experimental setup of method determining the effect of a ball lens target on optical path error.

The experimental setup is based on a general unbalanced-arm Michelson interferometer. A long-coherence light source (632.8 nm He-Ne laser, NEOARK) served as a light source. The laser beam was divided by a beam splitter. One beam was collimated by a lens to the back focal point of a ball lens target, and the other was incident on the reference mirror. The beams reflected from the target and the reference mirror recombined to produce a pattern fringe on an imaging screen. The ball lens was positioned to be concentric with a translation stage to avoid errors of stage rotation. The laser beam was then aligned until a fringe pattern appeared. The ball lens was rotated by the rotating stage, and the pattern fringe on the screen was observed.

In observation, the pattern fringe did not change during ball lens rotation. It can be implied that the ball lens caused an optical path error of less than one half of the laser source wavelength, i.e., less than 0.3 μm. However, vibration of the rotating stage directly affects the fringe pattern. Therefore, a precise, smoothly rotary stage is required to achieve high precision in the observed fringe pattern. A highly accurate roundness measuring machine to confirm the roundness accuracy of the target is an alternative. However, for one-dimensional length measurements, the sphericity of the ball lens does not affect the optical path difference, but it does significantly affect three-dimensional lengths measurements by the target. Thus, the error due to the target can be ignored for CMM diagonal measurements by the proposed method.

3.3. Preliminary absolute-length measurement

We demonstrated measurement reproducibility of our method by preliminary absolute-length measurements, as shown in Fig. 7. The optical components of this experiment were the same as described in Fig. 2. The absolute-length measurements were made

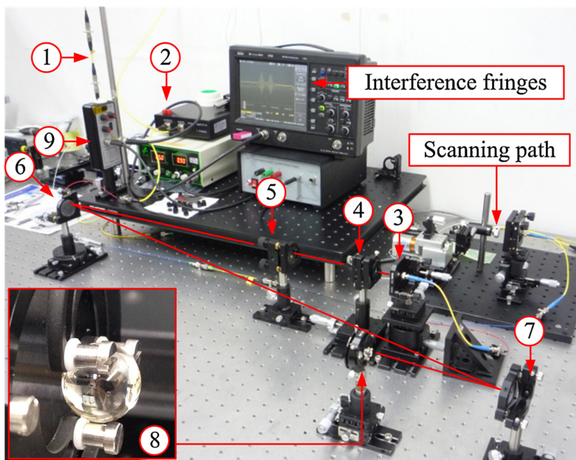

Fig. 7. Preliminary absolute-length measurement set up; (1) is a fiber etalon with 1-GHz FSR, (2) is an optical amplifier, (3) is a fiber holder, (4) is a lens, (5) is a reference position, (6) and (7) are mirrors, (8) is a ball lens target, and (9) is a photodetector.

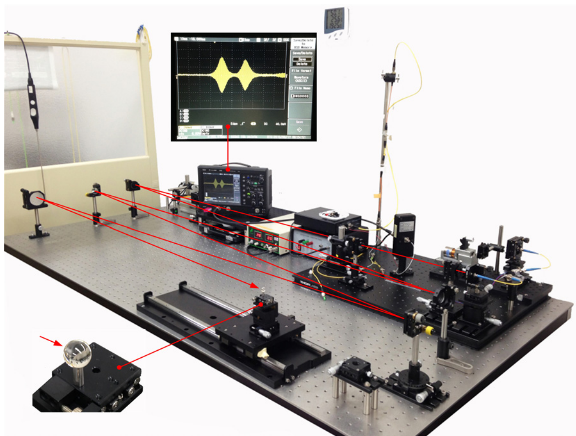

Fig. 8. Long-range measurement of a pulsed interferometer with a ball lens target (absolute-length measurement is approximately 9 m).

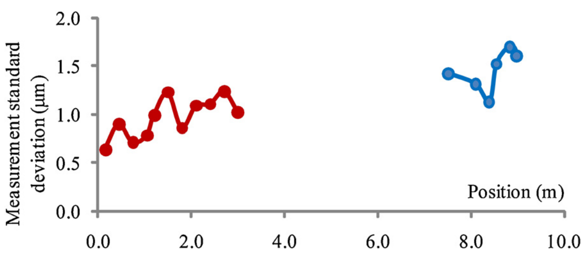

Fig. 9. Preliminary absolute-length measurement results; the maximum measurement standard deviation is approximately 1.25 μm for the measurement range of (0–3) m and 1.71 μm for the measurement range of (7.5–9.0) m.

at target positions approximately every 150 mm up to 3 m. The absolute lengths were measured and determined using Eq. (2).

Finally, we considered the efficiency of the optical-comb pulsed interferometer with the ball lens target in long-range measurements. The measurement setup is similar to the previous experiment, but the target was positioned from 7.5 m to 9.0 m. The measurement setup is shown in Fig. 8, and the measurement results of both the short-range (0–3 m) and long-range (7.5–9.0 m) measurements are shown in Fig. 9.

The maximum measurement standard deviation is approximately 1.25 μm for measurements in the range of (0–3) m, and 1.71 μm for measurements in the range of (7.5–9.0) m. The

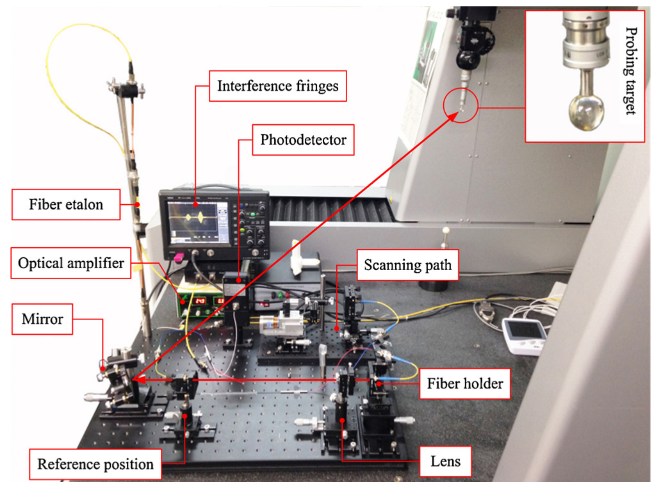

Fig. 10. Space diagonal of a CMM measurement using the pulsed interferometer.

reproducibility is mainly affected by environmental conditions, especially airflow fluctuations and mechanical vibrations. However, the interference fringes at 9.0 m are very clear, as illustrated in Fig. 8. These pattern fringes show that the signal-to-noise ratios of the long length measurements are very high. Therefore, the experimental results strongly indicate that the proposed measurement system can measure absolute lengths for a range of applications, because the maximum measurement volumes of most large-CMMs are approximately 10 m^3.

3.4. CMM space diagonals verification

A compact pulsed interferometer was connected to an optical comb passing through an optical fiber over 100 m from the 10th floor to the basement floor of a building. (The optical comb was installed at the 10th floor, and the CMM was installed at the basement of the building). A ball lens target was fixed on a CMM probe head. The diagonals of a moving bridge-type CMM (FALCIO APEX 707, Mitutoyo) were measured by the proposed technique, as shown in Fig. 10. First, the measurement lines were defined as in Fig. 1. To avoid optical path error due to the different refractive indices of air and the target, the initial zero positions of both the CMM and interferometer were set for a value of $m \geq 1$; therefore, the initial positions would compensate for the optical path error of each position. Absolute length measurements of the CMM probe were made at 150 mm increments along its diagonals using the proposed system.

To confirm the efficiency of our proposed method, these measurements were compared with the results of a standard artifact test method. The artifact was a step-gauge (S232, KOBA-step) with a steel frame, 16 ceramic gauges, 32 faces, and 20 mm nominal length. The thermal expansion coefficient was $11.5 \times 10^{-6}\,K^{-1}$. This step gauge was supported, and the reference lengths were measured by the National Metrology Institute of Japan, (NMIJ). The step gauge was aligned to approximate the measurement lines of the proposed method along the four diagonals of the CMM. A temperature sensor was attached to the gauge to monitor the gauge temperature during measurements. Each measurement line was measured only after the temperature of the step gauge had remained stable for more than 3 h. The diagonals of the CMM were verified, and the measurement results were corrected to the reference temperature (20 °C) [25]. The results of both methods are shown in Fig. 11(a)–(d), where the blue-diamonds lines are indication error of a CMM that measured by the proposed system, the red-circles lines are measured by a step gauge method, and

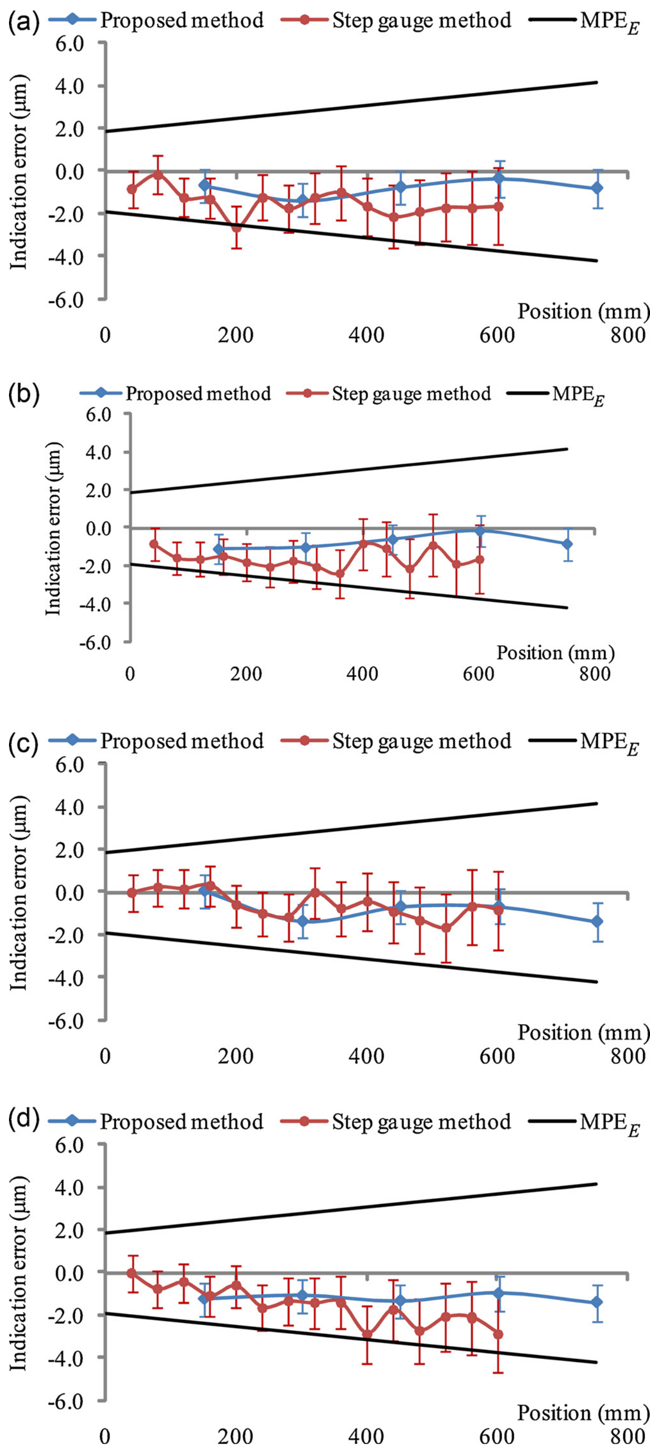

Fig. 11. Comparison of indication errors of CMM diagonal lines measured by the proposed method (blue diamonds), a standard step gauge method (red circles). MPE$_E$ is the maximum permissible error. (For interpretation of the references to color in this figure legend, the reader is referred to the web version of this article.)

the black lines are the maximum permissible error of a CMM. The measurements along the diagonal in space of a CMM refer to Fig. 1.

In the measurement comparisons, to reduce probing error of the CMM, only unidirectional measurements of step gauge were considered. The results show that all position measurements fall within the maximum permissible error of indication of a CMM for size measurement [$MPE_E = \pm(1.9 + 3l/1000)$ µm, where l is the indication length of the CMM measurement in mm]. The differences between the uncertainties of measurements are discussed in the next section. However, the proposed method is non-contact, and the positioning accuracy along each diagonal was verified approximately every 150 mm. In contrast, the step gauge methods are contact measurements, and each diagonal was verified at approximately every 40 mm, according to the nominal length of a step gauge. In addition, although error due to stylus tip compensation was eliminated by taking only unidirectional measurements, probing errors of the CMM still affect measurement repeatability. Measurement uncertainty of the proposed method was smaller than that of the step gauge due to slight effects of air temperature, because temperature distribution on a step gauge significantly affects the measurement uncertainty. In addition, the step gauge method is more time consuming than the proposed method because of the wait for stabilized temperature. The proposed method can directly verify a CMM after a 30-min warm up of the measurement system.

4. Uncertainty of measurement

The measurement uncertainty by our proposed method was evaluated in accordance with GUM [26]. The positioning error of each diagonal of the CMM (E_x), as measured by an optical-comb pulsed interferometer, is determined by Eq. (3).

$$E_x = l_x - l_s + \delta l_{ix} + l_N \cdot \alpha \cdot \Delta T \tag{3}$$

where l_x is the indication length of a CMM, l_s is the standard length determined by the proposed method, δl_{ix} is the correction due to finite resolution of the CMM, l_N is the nominal length, α is the thermal expansion coefficient of a linear scale of CMM, ΔT is the difference between the linear scale temperature of a CMM and the reference temperature.

According to Eq. (3), the uncertainty of CMM diagonal measurements is evaluated as Eq. (4).

$$u^2(E_x) = u^2(l_x) + u^2(l_s) + u^2(\delta l_{ix}) + l_N \cdot \Delta T u^2(\alpha) \tag{4}$$

The standard length (l_s), determined as in Eq. (2), relates to the uncertainties of the repetition frequency, the group refractive index of air, and the distance between peaks of the envelope interference fringes. The stability of the repetition frequency after passing through a fiber etalon is in the order of 10^{-9} over 2 h [16]. This partially contributes a length uncertainty of $0.5 \times 10^{-9}\ l$ divided by the rectangular distribution, because of the semi-range limits of the finite resolution of the instrument. The uncertainty of the repetition rate and carrier offset frequency of the optical comb are neglected because they are more than 100 times more accurate than the maximum permissible error of a CMM. The standard length was compensated for the group refractive index of air by Ciddor's equation. Therefore, this group refractive index of air equation relates to the uncertainties of air pressure, air humidity, and air temperature. The combined standard uncertainty for the length correction is determined by applying Ciddor's equation, in which the sensitivity coefficients are evaluated by first performing partial derivatives. The contribution to uncertainty of each parameter is evaluated by multiplying standard uncertainties with their sensitivity coefficients [26,27]. The uncertainties due to air pressure, air temperature, and air humidity were evaluated from the maximum variations in the laboratory during measurements; these were 0.1 kPa, 0.40 °C, and 0.5%RH respectively. These parameters were estimated to have rectangular limits, and the uncertainty of Ciddor's equation was estimated to be on the order of 10^{-8}.

Next, the uncertainty in the distance between peaks of interference fringe envelopes was determined by the relationship between time scale and length scale [18]. This was evaluated using the maximum deviation between the measured values and the best-fit line, and assumed to be a rectangular distribution.

Table 2
Uncertainty sources of CMM space diagonal verification using a pulsed interferometer.

Uncertainty source, x_i	Uncertainty value, $u(x_i)$	Uncertainty contribution, $u(y)$
Absolute uncertainty		
Repeatability of measurement	0.18 μm	0.18 μm
Variations due to the finite resolution of a CMM	0.29 μm	0.29 μm
Time and length scale measurement	0.18 μm	0.18 μm
Relative uncertainty		
Stability of modified repetition frequency	$<10^{-9}$	$2.89 \times 10^{-9}\ l$
Ciddor's equation	$<10^{-8}$	$1.00 \times 10^{-8}\ l$
Variation of air humidity	0.29%RH	$2.95 \times 10^{-9}\ l$
Variation of air pressure	57.74 Pa	$1.52 \times 10^{-7}\ l$
Variation of air temperature	0.23 °C	$2.11 \times 10^{-7}\ l$
Thermal expansion coefficient	1×10^{-6} K^{-1}	$2.31 \times 10^{-7}\ l$
Combined standard uncertainty	$[(0.38\ \mu m)^2 + (3.48 \times 10^{-7} l)^2]^{1/2}$	

l is the indication length of a CMM in mm.

Table 3
Uncertainty sources of CMM diagonal verification using a step gauge.

Uncertainty source, x_i	Uncertainty contribution, $u(y)$	
	Absolute	Relative
Uncertainty of step gauge	0.09 μm	$2.40 \times 10^{-7}\ l$
Repeatability of measurement	0.32 μm	–
Variations due to the finite resolution of a CMM	0.29 μm	–
Correction due to temperature distribution	–	$1.41 \times 10^{-6}\ l$
Expanded uncertainty $[(0.87)^2 + (2.86 \times 10^{-3} l)^2]^{1/2}$ μm		

l is the indication length of a CMM in mm.

In the measurement, the difference in temperature between linear scale of a CMM and a reference temperature cannot be directly measured, and the positions of a CMM in each diagonal were automatically corrected for thermal expansion to the reference temperature by CMM's software. Therefore, only uncertainty of the thermal expansion coefficient was considered.

The digital scale interval of the linear scale of CMM is 0.001 mm (the resolution in X, Y, and Z axes of a CMM are 0.0001 mm. In the experimental measurement, the resolution of a CMM was rounded of the reading at the digit of 1 μm). Variations due to this finite resolution were estimated to have rectangular limits of ±0.5 μm. And the measurement was repeated five times, resulting in a maximum standard deviation of approximately 0.40 μm. Consequently, uncertainty due to limited repeatability was estimated to have a normal distribution.

Finally, the expanded uncertainty (k = 2) of the CMM verification along the diagonals was calculated to be $[(0.77)^2 + (0.69 \times 10^{-3} l)^2]^{1/2}$ μm. The uncertainty components are summarized in Table 2.

The positioning error of each diagonal of a CMM (E_x) using a step gauge is determined by replacing the l_s term of Eq. (3) with the reference length of the step gauge. As a result, the uncertainty components are evaluated as in Eq. (5).

$$u^2(E_x) = u^2(l_x) + u^2(l_s) + u^2(\delta l_{ix}) + l_N \cdot \bar{\alpha} u^2(\Delta t) \quad (5)$$

where $\bar{\alpha}$ is the average thermal expansion coefficient of the step gauge and the linear scale of a CMM, and Δt is the temperature difference between the step gauge and linear scale of a CMM. The uncertainty sources of CMM diagonal verification using a step gauge are summarized in Table 3.

5. Conclusions

A new optical measurement method to verify CMMs was proposed. It is a single-mode fiber pulsed interferometer that performs non-contact measurements on a ball lens of refractive index 2 as a target. The target can be used for absolute-length measurements in all directions. The measurement range is up to 10 m, and the proposed method is directly traced to the SI base unit. If the uncertainty due to the finite resolution of a CMM is ignored because of dependent upon machines, the measurement capability of the proposed system is approximately $[(0.36)^2 + (0.69 \times 10^{-3}\ l)^2]^{1/2}$ μm, which the coverage factor k is 2, or approximately 7 μm for the indication length of 10 m. The experimental results show that the measurement accuracy depends on noise in the interference fringe caused by airflow fluctuations and mechanical vibrations. However, measurement uncertainty is smaller than that of the artifact test method due to the effects of air temperature. In addition, the measurement time of the proposed method is 60% less than that of the artifact method because of its shorter start-up time; the proposed method can be used in measurements after a 30-min system warm-up, while the artifact method requires a waiting period of more than 3 h to achieve a stabilized gauge temperature for each alignment. Moreover, the alignment procedure is easier in the proposed system because of the compact and convenient optical components. However, the proposed method is a non-contact one, and therefore its CMM verification does not include effects of the CMM probing system.

Acknowledgements

The authors appreciate the step gauge and reference lengths provided by the National Metrology Institute of Japan (NMIJ), Lengths and Dimensions Division, for use in the measurement comparison between the proposed method and the artifact test method.

References

[1] ISO10360-2. Geometrical Product Specification (SPC). Acceptance and reverification tests for coordinate measuring machines (CMM). Part 2: CMMs used for measuring linear dimensions. International Organization for Standardization; 2009.
[2] EAL-G17. Coordinate measuring machine calibration. European Cooperation for Accreditation of Laboratories; 1995.
[3] Abbe M, Takamasu K, Ozono S. Reliability on calibration of CMM. Measurement 2003;33:359–68.
[4] Aguilar JJ, Aguado S, Santolaria, Samper D. Multilateration in volumetric verification of machine tool. In: XX IMEKO World Congress. 2012.
[5] Schwenke H, Schmitt R, Jatzkowski P, Warmann C. On-the-fly calibration of linear and rotary axes of machine tools and CMMs using tracking interferometer. CIRP Ann Manuf Technol 2009;58:477–80.
[6] Barakat NA, Elbestawi MA, Spence AD. Kinematic and geometric error compensation of a coordinate measuring machine. Int J Mach Tool Manuf 2000;40:833–50.
[7] Trapet E, Wäldele F. A reference object based method to determine the parametric error component of coordinate measuring machines and machine tools. Measurement 1991;9:17–22.
[8] Swornowski PJ. A new concept of continuous measurement and error correction in coordinate measuring technique using a PC. Measurement 2014;50:99–105.
[9] Weckenmann A, Lorz J. Monitoring coordinate measuring machine by calibrated parts. In: 7th international symposium on measurement technology and intelligent instruments. 2005. p. 183–90.
[10] Curran E, Phelen P. Quick check error verification of coordinate measuring machines. J Mater Process Technol 2004;15:5–156, 1207–13.
[11] Cauchick-Miguel P, King T, Davis J. CMM verification: a survey. Measurement 1996;17:1–16.

[12] Phillips SD, Sawyer D, Borchardt B, Ward D, Beutel DE. A novel artifact for testing large coordinate measuring machines. Precis Eng 2001;25:29–34.
[13] Arriba L, Trapet E, Bartscher M, Franke M, Balsamo A, Costelli G, et al. Method and artifacts to calibrate large CMMs. European standards measurements and testing programme, Project SMT4-PL97-2330; 1999.
[14] Cundiff ST, Ye J. Femtosecond optical frequency comb. Rev Mod Phys 2003;75:325.
[15] Matsumoto H, Wang X, Takamasu K, Aoto T. Absolute measurement of baselines up to 403 m using heterodyne temporal coherence interferometer with optical frequency comb. Appl Phys Express 2012;5:046601.
[16] Chanthawong N, Takahashi S, Takamasu K, Matsumoto H. Performance evaluation of a coordinate measuring machine's axis using a high-frequency repetition mode of a mode-locked fiber laser. Int J Precis Eng Manuf 2014;15:1507–12.
[17] Wang X, Takahashi S, Takamasu K, Matsumoto H. Spatial positioning measurements up to 150 m using temporal coherence of optical frequency comb. Precis Eng 2013;37:635–9.
[18] Wiroj S, Hirokazu M, Satoru T, Kiyoshi T. Verification of the positioning accuracy of industrial coordinate measuring machine using optical-comb pulsed interferometer with a rough metal ball target. Precis Eng 2015;41:63–7.
[19] Balling P, Křen P, Mašika P, van den Berg SA. Femtosecond frequency comb based distance measurement in air. Opt Express 2009;17:9300–13.
[20] Ciddor PE, Hill RJ. Refractive index of air. 2. Group index. Appl Opt 1999;38:1663–7.
[21] Ciddor PE. Refractive index of air: new equations for the visible and near infrared. Appl Opt 1995;35(9):1566–73.
[22] Šmíd R, Číp O, Lazar J. Precise length etalon controlled by stabilized frequency comb. Meas Sci Rev 2008;8(5):114–7.
[23] Nakamura O, Goto M, Toyoda K, Takai N, Kurosawa T, Makamata T. A laser tracking robot-performance calibration system using ball-seated bearing mechanisms and a spherically cat's-eye retroreflector. Rev Sci Instrum 1994;65:1006–11.
[24] Toshiyuki T, Mitsuo G, Sonko O, Ruimin Y, Tomizo K. Whole-viewing-angle cat's-eye retroreflector as a target of laser trackers. Meas Sci Technol 1999;10:N87–90.
[25] ISO 1. Geometrical product specification (SPC). Standard reference temperature for geometrical product specification and verification. International Organization for Standardization; 2002.
[26] Evaluation of measurement data-Guide to the expression of uncertainty in measurement, GUM 1995 with minor corrections, vol. 100, 1st Ed. JCGM; 2008.
[27] EA-4/02. Evaluation of the uncertainty of measurement in calibration. European Co-operation for Accreditation; 2013.

Precision Engineering 46 (2016) 254–262

Contents lists available at ScienceDirect

Precision Engineering

journal homepage: www.elsevier.com/locate/precision

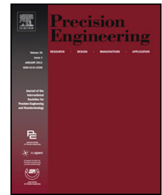

Calibration for the sensitivity of multi-beam angle sensor using cylindrical plano-convex lens

Chen Meiyun[a,*], Takahashi Satoru[b], Takamasu Kiyoshi[a]

[a] Faculty of Engineering, Department of Precision Engineering, The University of Tokyo, 7-3-1 Hongo, Bunkyo-ku, Tokyo 113-8656, Japan
[b] Research Center for Advanced Science and Technology, The University of Tokyo, 4-6-1 Komaba, Meguro-ku, Tokyo 153-8904, Japan

ARTICLE INFO

Article history:
Received 23 February 2016
Received in revised form 18 April 2016
Accepted 6 May 2016
Available online 21 May 2016

Keywords:
Autocollimator
Calibration
Sensitivity
Cylindrical plano-convex lens
Multi-beam angle sensor

ABSTRACT

A highly sensitive and compact multi-beam angle sensor (MBAS), which utilizes the principle of operation of an autocollimator, was developed to detect the differential of the local slope components (angle difference) of a point on the mirror surface and using Fourier series, we can obtain the profile data from the angle difference. In order to investigate the application of the MBAS for high precision aspheric surface measurements, two types of calibration methods using plane mirror and cylindrical plano-convex lens has been proposed to measure the sensitivity of the MBAS. The calibration data analysis results using plane mirror agree well with the measurement results of the cylindrical plano-convex lens data. Comparison of the two methods confirms that the second method (using cylindrical plano-convex lens) is more adapted for measurement with ultra high level of uncertainty. Further, the second method is simple, corresponding to a direct calculate in the sensitive parameters aiming to minimize the cost.
© 2016 Elsevier Inc. All rights reserved.

1. Introduction

Precision autocollimators are the most accurate, widely available means of measuring the tilt angle of a reflecting plane mirror. They have a wide range of applications such as optical metrology instruments, the semiconductor industry, and inspection equipment (Whitehouse, 1976; Chetwynd and Siddall, 1976; Vissiere et al., 2012; Whitehouse, 1974).

The autocollimator method is generally used to measure flatness due to its simple optical-path design (Ennos and Virdee, 1982; Xiao et al., 2012; Ennos and Virdee, 1983). At the Tohoku University, the optical was modified by fitting the photoelectric autocollimator with a resolution of 0.1″ for angle measurements (Gao and Kiyono, 1997; Gao et al., 2002). The well-balanced harmonic response in the entire frequency range is a drawback of this method. Bručas proposed and developed two modified autocollimators by fitting a charge-coupled device (CCD) to the optical units, which can be also used for the angle measurements (Bručas and Giniotis, 2009a,b, 2010). However, they are very time consuming and too many autocollimators make it difficult to adjust the direction of the sensor's radius. At the Physikalisch-Technische Bundesanstalt institute, the autocollimators are calibrated by using a WMT 220 angle comparator, which demonstrated the direct traceability of high-resolution autocollimators to the SI unit of the plane angle (Just et al., 2009; Probst et al., 1998; Probst, 2008). It is expected that the measurement uncertainty of the angle will be further reduced by calibrating the angle autocollimator, so that in future the measurement can be attained with an even smaller uncertainty (Just et al., 2003; Yandayan et al., 2011; ISO/IEC Guide 98-3:2008).

In order to investigate the application of the multi-beam angle sensor (MBAS) for high precision roundness measurements, we previously reported the preliminary results of MBAS applications to measure the surface profiles of a cylindrical workpiece. Using Fourier series, we obtained the profile data from the angle difference (Chen et al., 2015a, 2014). Here, we present a new detailed, expanded two types of calibration methods for the sensitivity of MBAS using a plane mirror and cylindrical plano-convex lens. The calibration data analysis results using plane mirror agree well with the measurement results of the cylindrical plano-convex lens data. In the second method (using cylindrical plano-convex lens), the radius of curvature R and the differential spacing Δd can be used to calibrate the sensitivity of the MBAS. Despite the simplicity of the proposed method, the uncertainty budget for the sensitivity of the MBAS in the calibration experiment using plane mirror agrees well with the measurement results of the sensitivity in the cylindrical plano-convex lens experiment, which also verified the feasibility of the calibration for the MBAS sensitivity using a cylindrical plano-convex lens.

* Corresponding author. Fax: +81 3 5841 6472.
E-mail address: chenmeiyun@nanolab.t.u-tokyo.ac.jp (M. Chen).

http://dx.doi.org/10.1016/j.precisioneng.2016.05.004
0141-6359/© 2016 Elsevier Inc. All rights reserved.

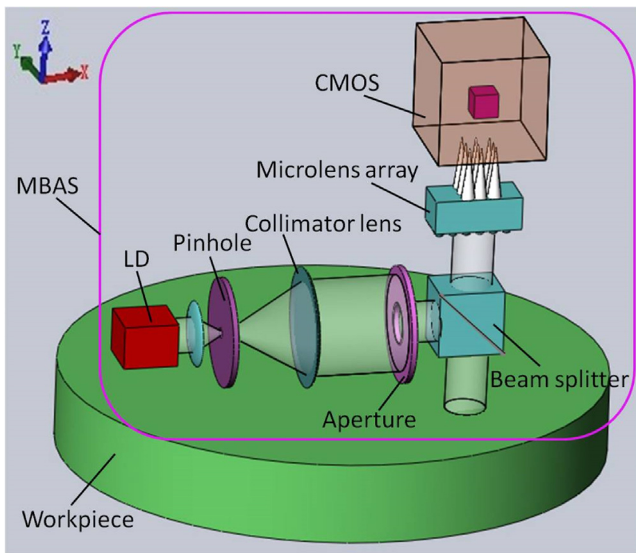

Fig. 1. Construction of the MBAS.

Comparison of the two methods confirms that the second method is more adapted for measurement with ultra high level of uncertainty. Further, the second method is simple, corresponding to a direct calculate in the sensitive parameters aiming to minimize the cost.

2. Principle of operation

2.1. Multi-beam angle sensor for flatness measurement of mirror

An autocollimator is an optical instrument for non-contact measurement of angles from a reflecting surface. The MBAS is based on a multi-autocollimator system using microlenses to measure deflections in an optical system. The MBAS works by projecting an image onto a beam splitter, and measuring the deflection of the returned image against a scale. The reflected angles at several points on the mirror surface can be measured using the sensor. Then, the sensor scans the workpiece while it is rotating.

Fig. 1 illustrates the optical system of the MBAS. The laser beam from a laser diode (LD) passes through a pinhole, and it is collimated by a collimator lens. The beam is then bent by a beam splitter and projected to the workpiece surface. The reflected beam from the workpiece surface passes totally through the beam splitter to the microlens, and after being focused on the microlens, it is split into several beams. The resulting pattern is observed and recorded by a CMOS camera mounted along the vertical axis. The imaging can be observed on a TV monitor. In order to investigate the application of the multi-beam angle sensor (MBAS) for high precision roundness measurements, we previously reported the preliminary results of MBAS applications to measure the surface profiles of a cylindrical workpiece. Using Fourier series, we obtained the profile data from the angle difference (Chen et al., 2015a, 2014).

Using the MBAS, we implemented the experimental system shown in Fig. 2. A workpiece was placed on the tilt stage, and the rotary platform is mounted between two *XY*-platforms. Therefore, the rotary table in this case acts as a small angle generator and the reference mean of angle measurement.

Fig. 3 illustrates how the two points A and B in the circumference of the circle with certain radius are carried out by rotating the workpiece step by step (Chen et al., 2015b). The workpiece flatness is calculated by applying the autocollimator principle of the angle difference at each of these two angles on the workpiece. The angle difference can be calculated from the intensity distribution of the spots on the CMOS (Chen et al., 2016). Then, the specimen profile at each location on the circle can be determined accurately. This procedure is repeated for circular scans of different radii, to yield the overall shape of the surface.

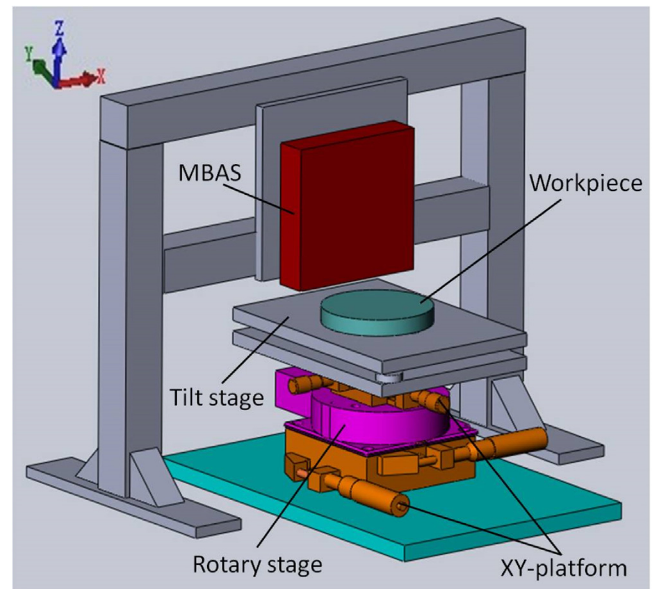

Fig. 2. Schematic of the micro-SMM.

In the flatness measurement, the sensitivity W and width of the lattice spacing Δd (calculated from the angle difference using MBAS) have been used to estimate the radius of curvature R of the cylindrical plano-convex lens (if R is unknown). Here, the profile of cylindrical is also can be calculated from the curvature R. Therefore the sensitivity W is an important parameter in the profile measurement.

Reversely, in the calibration experiment, the radius of curvature R and width of the lattice spacing Δd (calculated from the angle difference using MBAS) have been used to calibrate the sensitivity of the MBAS.

2.2. Measurement of the sensitivity W

Using the MBAS, we could measure the flatness of several tens micrometer with repeatability of several tens nanometer. Some flatness measurement results also imply that the MBAS can measure flatness with absolute accuracy under several tens nanometer if the sensitivity W is less than 0.5% (Chen et al., 2015b, 2016). Therefore, an important prerequisite for the determination of the measurement uncertainty can be achieved with the accurate calibration of sensitivity of the MBAS.

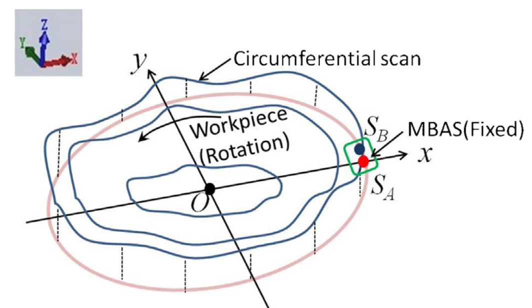

Fig. 3. Profile measurement along the circumference of a circle with certain radius: the multi-beam angle sensor is fixed onto the support structure and scanning the workpiece while it is rotating.

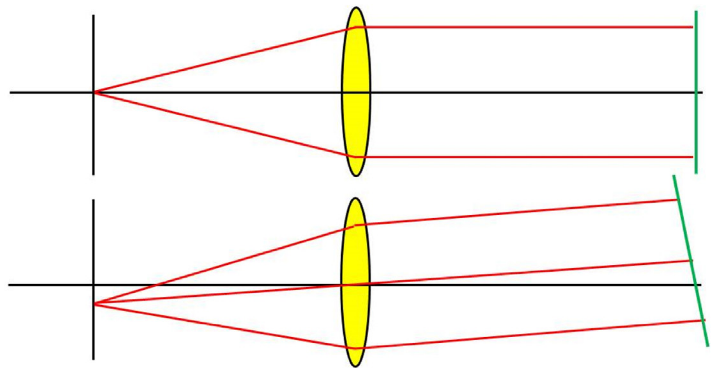

(a) Perfectly collimated beam: the slope is coupled to the position of spot.

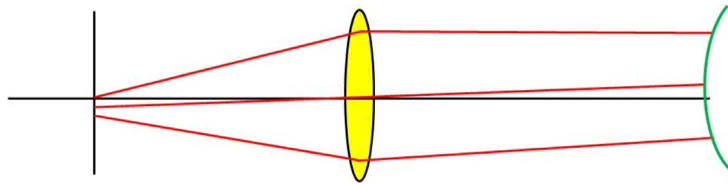

(b) Nearly collimated beam: the slope of the center of the lens is coupled to the center of the spot.

Fig. 4. Focusing a collimated laser beam: the relationship between the beam, slope, and spot.
(a) Perfectly collimated beam: the slope is coupled to the position of spot.
(b) Nearly collimated beam: the slope of the center of the lens is coupled to the center of the spot.

2.2.1. The principle of the MBAS for measurement of variable-radius of curvature

In order to investigate the sensitivity of the MBAS in measurement of variable-radius of curvature, the principle for the flatness and aspheric surface measurement are discussed.

As a first example, we consider a common application in flatness measurement, the focusing of a perfectly collimated beam to a small spot, which is shown in Fig. 4(a). Here we have a laser beam, which is focused by a lens. From Fig. 4(a), we find that the slope is coupled to the position of the spot.

Another example is the nearly collimated beam focused by a lens in aspheric surface measurement, as shown in Fig. 4(b). Only the slope of the center of the lens is coupled to the center of the spot and the size of the spot increases. The problem is often stated in terms of focusing the output from a “parallel light source.”

A further analysis of the radius of curvature and sensitivity of the autocollimator will be discussed on this topic in Section 2.2.2.

2.2.2. Calculating the sensitivity W *from the radius of curvature* R

In order to obtain a precise estimate of the signal in the measurement of the aspheric surface, a multi-spot light beam has been developed for measurement of the local slope of the cylinder lens. Whereas in this situation, the MBAS is sequential with a highly flexible sampling pattern and measures aberrations of the incoming beam using only one sensor for an imaging system. Here, we have a laser beam as shown in Fig. 5, with radius of curvature R and divergence 2α that is focused by a lens of focal length f. Assuming that the lattice spacing of the lens is d, k is the distance between the lens and aspheric surface, and the position of the beam coming from the center of lens on the aspheric surface is c, we can obtain the divergence α by the lens spacing between points A and B, d_{AB} and radius of curvature R. The divergence α is then given by:

$$\alpha = \frac{d_{\mathrm{AB}}}{2R} \tag{1}$$

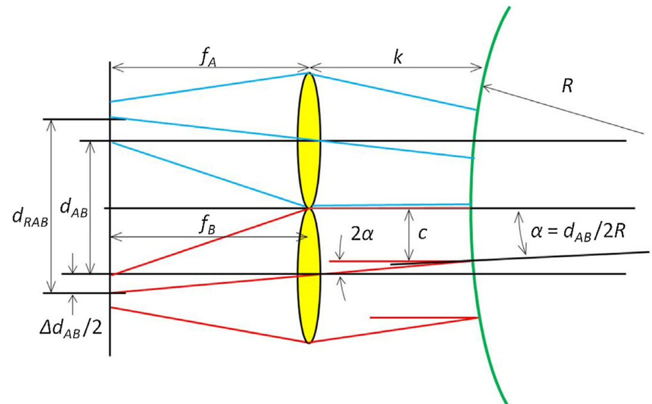

Fig. 5. The lattice spacing varied with focal distance f, lens spacing d, the spot spacing d_R, the radius of curvature of the workpiece R, the differential spacing Δd_{AB} and the distance between lens and aspheric surface k.

The optical invariant then tells us that we must have Eq. (2), because the product of the radius and divergence angle must be constant. From Fig. 5, we obtain the lens spacing between points A and B, d_{AB}, by the following:

$$\frac{d_{\mathrm{AB}}}{2} = c + 2\alpha k \tag{2}$$

From Eqs. (1) and (2), we obtain the position of the beam from center lens on the aspheric surface c, calculated by a simple equation:

$$c = \frac{R d_{\mathrm{AB}}}{2R + 4k} \tag{3}$$

From Fig. 5, we obtain the spot spacing between points A and B, $d_{R\mathrm{AB}}$, by the following:

$$\frac{d_{R\mathrm{AB}}}{2} = \frac{d_{\mathrm{AB}}}{2} + \alpha(f_{\mathrm{A}} + f_{\mathrm{B}}) \tag{4}$$

From Eqs. (3) and (4), we obtain the differential between the lens spacing d and the spot spacing d_R, Δd_{AB} (the differential spacing), by the following:

$$\Delta d_{AB} = d_{RAB} - d_{AB} = \frac{(f_A + f_B)d_{AB}}{R + 2k} \tag{5}$$

Accordingly, a variation in the differential spacing of points A and B, can be known from variation in the focal distance f_{AB}, lens spacing d_{AB}, radius of curvature of the workpiece R, and distance between lens and aspheric surface k.

In order to know, theoretically, the relationship between the radius of curvature R and the sensitivity between points A and B, we derived the following formula:

$$R = \frac{(f_A + f_B)d_{AB}}{\Delta d_{AB}} - 2k = \frac{W_{AB}}{\Delta d_{AB}} - 2k \tag{6}$$

where W_{AB} is the sensitivity between points A and B, which can be described as follows:

$$W_{AB} = (f_A + f_B)d_{AB} \tag{7}$$

Here, the sensitivity in the calibration experiment using plane mirror can be calculated from Eqs. (7).

We note that the sensitivity W_{AB} can also be denoted as:

$$W_{AB} = (R + 2k)\,\Delta d_{AB} \tag{8}$$

Similarly, the sensitivity in the calibration experiment using cylindrical plano-convex lens can be calculated from Eqs. (8).

In order to know, theoretically, the relationship between the radius of curvature R and the sensitivity W_{AB} between points A and B, we derived formula:

$$R = \frac{W_{AB}}{\Delta d_{AB}} - 2k \tag{9}$$

In the flatness measurement, using Formula (9), the sensitivity W and width of the lattice spacing Δd (calculated from the angle difference using MBAS) have been used to estimate the radius of curvature R of the cylindrical plano-convex lens (if R is unknown). Here, the profile of cylindrical is also can be calculated from the curvature R. Therefore the sensitivity W is an important parameter in the profile measurement.

Reversely, in the calibration experiments, using Formula (7), we can calculate the sensitivity W by measuring focal lens f of two spots and the lens spacing d between two spots; using Formula (8), we can calculate the sensitivity W by measuring the width of the lattice spacing Δd between two spots (calculated from the angle difference using MBAS).

2.3. Calibration of the MBAS

For the determination of the sensitivity of MBAS, two independent calibration methods can be applied using the Formulas (7) and (8) in Section 2.2.2.

One fundamental calibration method is based on a comparison of all displacements in a measurement range with certain steps of a plane mirror. The selection of measurement points and precise adjustment of the angles specified is performed with the aid of a tilt stage and laser hologage. Using Formula (7), we can calculate the sensitivity W by measuring focal lens f of two spots and the lens spacing d between two spots.

Another novel calibration method is independent of any assistive tools, which is based on the angle difference measurement using a cylindrical plano-convex lens (if the radius of curvature R is known). Using Formula (8), we can calculate the sensitivity W by measuring the width of the lattice spacing Δd between two spots (calculated from the angle difference using MBAS).

2.3.1. Using plane mirror and tilt stage

Calibration of the autocollimator is always a complicated task since small angle steps must be generated with a very high precision. In principle, the measurement step width can be selected by the resolution of the autocollimator; however, limited by the repeatability of the MBAS readout, the selection of micro area measurement steps is necessary to detect short period deviation of the autocollimator. As the scope of the calibration must be kept within reasonable limits and additional requirements for long-term stability must be met in the case of long measuring times, calibrations in micro area measurement steps are carried out only over selected small sections of the measurement range. The most accurate available method is to perform calibrations in different measurement ranges with appropriate measurement steps.

Fig. 6 illustrates the construction of calibration performed by comparison with the sensitivity of the autocollimator in different points. The measured displacement of the spot values of the MBAS with different t indicated for the sensitivity difference of the autocollimator. The selection of measurement points and precise adjustment of the angles specified is performed with the aid of a laser hologage. For data acquisition, 30 single values are read out in each adjustment for 10 μm displacement of the tilt stage and mean values of the displacement of spot are calculated. To eliminate the linear drift influences during calibration, three measurement series are carried out to obtain the standard deviation.

Here, the distance between the fulcrum and observation point l is 132 mm, the displacement of the tilt stage h is 10 μm (measurement step). Thus, the angle of inclination t (in μrad) can be described by Eq. (10).

$$t = \frac{1000h}{l} \tag{10}$$

The sensitivity of the autocollimator s can be expressed as:

$$s = \frac{t}{p} \tag{11}$$

where p represents the ratio between the angle of inclination t and sensitivity of the autocollimator s. From Eqs. (10) and (11), we can derive the sensitivity of the autocollimator s (in μrad/pixel), which is expressed as follows:

$$s = \frac{1000h}{pl} \tag{12}$$

The focal length of the microlens array f (in μm) can be denoted as:

$$f = \frac{d_s}{2S} \tag{13}$$

From Eqs. (12) and (13), we can derive the focal length of the microlens array f (in mm), which is expressed as follows:

$$f = \frac{pld_s}{2h} \tag{14}$$

To evaluate the sensitivity W based on the calibration method using real datasets, the measurement components were also analyzed.

Explanations regarding the components are:

(p_A, p_B) Here p represents the ratio between the angle of inclination t and sensitivity of the autocollimator s. p_A and p_B is the ratio in point A and B, respectively. According to the calibration experiment using plane mirror, the ratio p can be calculated by the mean value of typically 3–5 repeat measurements.

($\frac{ld_s}{2h}$) Here the distance between the fulcrum and observation point l is 132 mm, the sensitive area of the CMOS d_s is 2.2 μm and the displacement of the tilt stage h is 10 μm. We can calculate the coefficient of the focal distance is 14.520 (in mm/pixel).

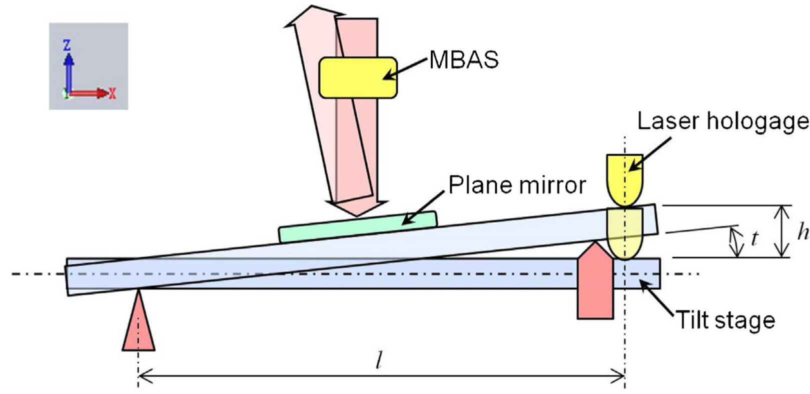

Fig. 6. Calibration system (principle): h is the displacement (the measurement value of the laser hologage) of the tilt stage, l is the distance between the fulcrum and observation points, and t is the angle of inclination.

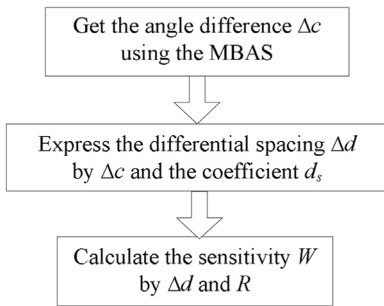

Fig. 7. Algorithm flowchart of the measurement: from the differential spacing Δd to the sensitivity W_{AB} using radius of curvature R.

(f_A, f_B) Here f_A and f_B is the focal length in point A and B, respectively. From Eq. (14), we can calculate the focal length of microlens array at each point.

(d_{AB}) Calculation of the mean value of typically 3–5 repeat measurements. The standard average value of the differential spacing between points A and B is found by simple arithmetic:

$$d_{AB} = (d_A - d_B)\, d_s \tag{15}$$

From Eq. (15), we also can calculate pitch of the microlens array d_{AB}.

Finally, the sensitivity W_{AB} between points A and B can be calculated from Eq. (7). Similarly, we can obtain the sensitivity W for other points.

2.3.2. Using cylindrical plano-convex lens

Fig. 7 shows the algorithm flowchart of the measurement. The angle difference value can be measured by MBAS, then to evaluate the sensitivity W based on the measurement of the cylindrical plano-convex lens using real datasets, the measurement components are analyzed as follows.

Explanations regarding the components are:

(Δd_{AB}) We note that the relationship between the differential spacing Δd_{AB} and the angle difference Δc_{ab} can be denoted as:

$$\Delta d_{AB} = \frac{\Delta c_{ab}}{1000 \times d_s} \tag{16}$$

Here the sensitive area of the CMOS d_s is 2.2 μm.

($R + 2k$) Calculation of the mean value of typically 5–10 repeat measurements. The standard average value of the distance between the lens and aspheric surface k is 55.5 (in mm). Here, as shown in Table 3, the radius of curvature R of the cylindrical plano-convex lens is 519 (in mm).

(W_{AB}) Furthermore, we can obtain the sensitivity W_{AB} from Eq. (8).

Consequently, the sensitivity W_{AB} can be denoted as the differential spacing Δd_{AB} using the radius of curvature R. Similarly, we can obtain the sensitivity for other points.

The characteristics of the algorithm chart can be estimated by its transfer function, which defines the relationship between the differential spacing Δd_{AB} and the sensitivity W_{AB}.

2.4. Estimation of uncertainty

In statistics, propagation of error is the effect of variable uncertainty in the measurement of plane mirror. We can estimate the uncertainty in the calibration method using an error propagation matrix that is deformed by neglecting correlations or assuming independent variables, yielding a common formula to calculate error propagation, the variance equations (Ku, 1966):

$${\sigma_s}^2 = \left(\frac{\partial s}{\partial h}\right)^2 {\sigma_h}^2 + \left(\frac{\partial s}{\partial p}\right)^2 {\sigma_p}^2 + \left(\frac{\partial s}{\partial l}\right)^2 {\sigma_l}^2 \tag{17}$$

where σ_s represents the standard deviation of the function s, σ_h represents the standard deviation of h, σ_p represents the standard deviation of p, and σ_l represents the standard deviation of l. From Eqs. (12) and (17), the standard deviation of the function s is obtained as Eq. (18).

$$\sigma_s = \sqrt{\left(\frac{1000}{pl}\right)^2 {\sigma_h}^2 + \left(\frac{1000h}{p^2 l}\right)^2 {\sigma_p}^2 + \left(-\frac{1000h}{pl^2}\right)^2 {\sigma_l}^2} \tag{18}$$

$$\sigma_s = \sqrt{s^2\left(\frac{\sigma_h}{h}\right)^2 + s^2\left(-\frac{\sigma_p}{p}\right)^2 + s^2\left(-\frac{\sigma_l}{l}\right)^2} \tag{19}$$

From Eq. (19), the standard deviation of the function s can also be expressed in terms of the standard deviations of the other functions, given by:

$$\sigma_s = s\sqrt{\left(\frac{\sigma_h}{h}\right)^2 + \left(\frac{\sigma_p}{p}\right)^2 + \left(\frac{\sigma_l}{l}\right)^2} \tag{20}$$

We note that the relationship between standard deviation of the function σ_s and sensitivity of the autocollimator s can be denoted as:

$$\frac{\sigma_s}{s} = \sqrt{\left(\frac{\sigma_h}{h}\right)^2 + \left(\frac{\sigma_p}{p}\right)^2 + \left(\frac{\sigma_l}{l}\right)^2} \tag{21}$$

It is important to note that this formula is based on the linear characteristics of the gradient of s and therefore it is a good estimation for the standard deviation of s as long as $\sigma_h, \sigma_p, \sigma_l$ are small compared to the partial derivatives (Clifford, 1973).

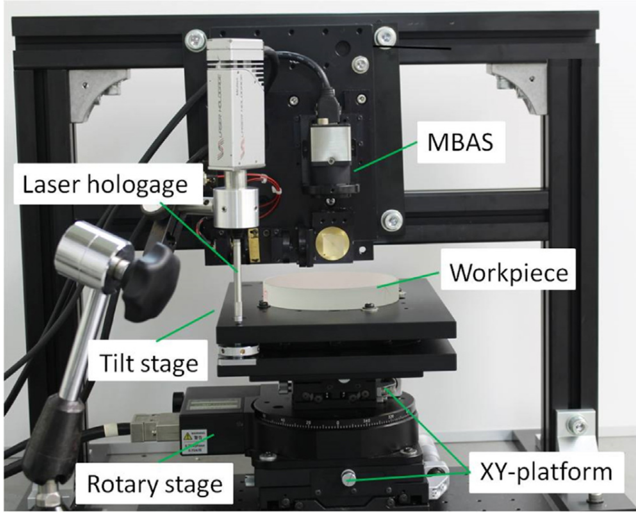

Fig. 8. Measurement arrangement for calibration of the MBAS: main setup of the pre-experiment consisted of the MBAS, a laser hologage, a tilt stage, a rotary stage, and two *XY*-platforms.

Table 1
Specifics of devices in MBAS (Fig. 8).

Laser diode	Output power: 35 mW (CW) Wavelength: 658 nm
Pinhole	Diameter: 400 μm
Aperture	Diameter: 4 mm
Microlens array	Focal length (f): 46.7 mm Pitch of the array: 500 μm
CMOS	Size: 5.6 mm × 4.2 mm Valid pixels: 2560 pixels × 1920 pixels Sensitive area (d_s): 2.2 μm × 2.2 μm
Laser hologage	Resolution: 0.01 μm Repeatability: 0.02 μm
Tilt stage	Size: 160 mm × 220 mm Tilt range: (α axis) ±0.7°; (β axis) ±0.6°

Similarly, from Eqs. (7) and (8), the standard deviation of the function W_{AB} can also be expressed in terms of the standard deviations of the other functions, given by:

$$\sigma_{W_{AB}} = \sqrt{(d_{AB})^2\sigma_{f_A}^2 + (d_{AB})^2\sigma_{f_B}^2 + (f_A + f_B)^2\sigma_{d_{AB}}^2} \tag{22}$$

$$\sigma_{W_{AB}} = \sqrt{(\Delta d_{AB})^2\sigma_R^2 + 4(\Delta d_{AB})^2\sigma_k^2 + (R + 2k)^2\sigma_{\Delta d_{AB}}^2} \tag{23}$$

3. Experiment and result

3.1. Configuration of the experiment

The pre-experimental arrangement is shown in Fig. 8. In the pre-experiment, the MBAS is based on a multi-autocollimator system using a microlens array. The main setup of the pre-experiment consisted of the MBAS, a laser hologage, a tilt stage, a rotary stage, and two *XY*-platforms. The workpiece is centered with respect to the axis of rotation; the autocollimator (MBAS) is aligned such that the horizontal measuring axis and the optical axis of the MBAS lie in the workpiece plane. A tilt stage is mounted between the rotary stage and workpiece, which can be used to adjust the workpiece plane so that it reflects the beam of the MBAS at defined angles.

The resulting pattern (in Fig. 9) is observed and recorded by a CMOS camera mounted along the vertical axis. Table 1 shows the specifications of the devices in Fig. 8. By using the intensity

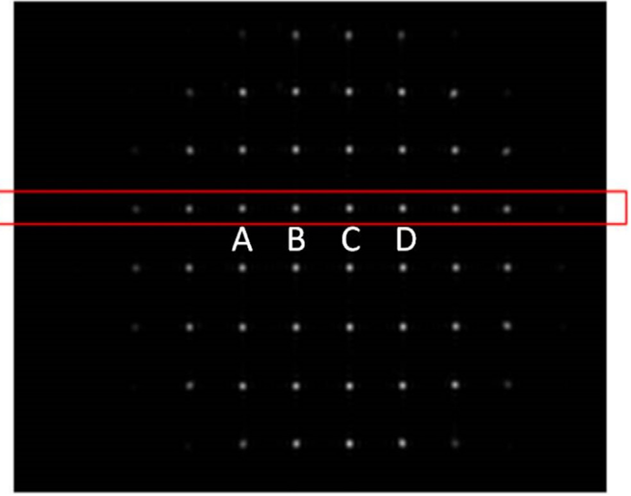

Fig. 9. Image from the CMOS.

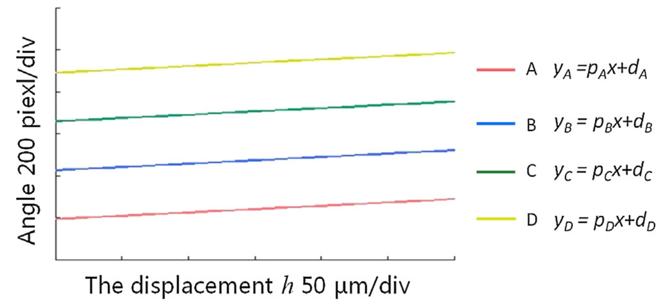

Fig. 10. The displacement of the spot in a measurement range of ±150 μm in steps of 10 μm.

distribution, the angle difference data can be calculated (Chen et al., 2015a).

3.2. Experiment of the plane mirror

In the following, the displacement of the spot (averaged over three measurement series) results for the autocollimator will be discussed. As a measure of reproducibility, Fig. 10 shows the standard average value of 30 single values of the autocollimator for a calibration over a measurement range of ±150 μm in measurement steps of 10 μm. The ratio of the output and displacement of the tilt stage at different points (A, B, C, and D in Fig. 10) is compared, where the ratio is the displacement of the spot on average.

According to the principle in Section 2.3.1 and the results shown in Fig. 10, the sensitivity W_{AB} between points A and B is 47.084. Similarly, we can obtain the sensitivity W for other points, as shown in Table 2.

The theoretical value of the sensitivity of the autocollimator S_0 (in μrad/pixel) can be denoted as:

$$S_0 = \frac{d_s}{2f} \tag{24}$$

Here the sensitive area of the CMOS d_s is 2.2 μm and the focal length of microlens array f is 46.7 mm. From Eq. (24), we can calculate the theoretical value of the sensitivity of the autocollimator S_0 = 23.55 μrad/pixel.

Assuming that the σ_h (the standard deviation of h) is 0.01, from Eq. (21), we can calculate the ratio between standard deviation of the function σ_s and the sensitivity of the autocollimator s = 0.5%;

Table 2
Summary of the results for the measurement of plane mirror.

Type	Estimate/pixel	Coefficient	Estimate/(mm/pixel)	Component	Estimate/mm
p_A	3.176	$\frac{ld_s}{2h}$	14.520	f_A	46.120
p_B	3.168	$\frac{ld_s}{2h}$	14.520	f_B	45.994
$d_A - d_B$	232.340	d_s	0.0022	d_{AB}	0.511
				$W_{AB}/(\text{mm}^2) = 47.084$	

	AB	BC	CD
Sensitivity W/mm^2	47.084	46.826	46.890

Table 3
Specifications of the cylindrical plano-convex lens.

Parameters	Values
Size	30 mm × 30 mm
Focal length	1000 mm
Edge thickness	4.8 mm
Center thickness	5 mm
Radius of curvature	519 mm

Table 4
Summary of the results for the measurement of cylindrical plano-convex lens.

Type	Estimate/mm	Coefficient	Estimate/mm
Δd_{AB}	0.0747	$R + 2k$	630
		$W_{AB}/(\text{mm}^2) = 47.082$	

	AB	BC	CD
Sensitivity W/mm^2	47.082	46.847	46.930

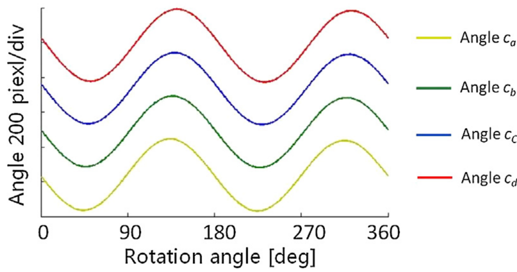

Fig. 11. Measured angle data at points A, B, C, and D.

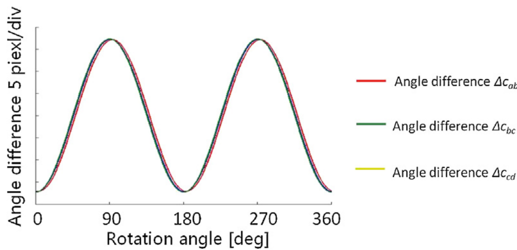

Fig. 12. Measured angle difference data for a cylindrical plano-convex lens measured by the MBAS.

similarly, when the σ_p is 0.01 pixel, the ratio is 1.5%; when the σ_l is 1 mm, the ratio is 0.75%.

3.3. Experiment of the cylindrical plano-convex lens

In the experiment, cylindrical plano-convex lenses were used as specimens. Table 3 shows the specifications of the workpiece; the cylindrical plano-convex lens has a convex curvature in the vertical direction and has no curvature in the horizontal direction.

Fig. 11 shows the angle data c_a, c_b, c_c, and c_d measured by the MBAS system for a cylindrical plano-convex lens. The horizontal axis is the rotation angle and the vertical axis is the angle data value. The angles of the specimen at points A, B, C, and D are 414.2, 411.0, 413.3, and 419.5 (in pixel), respectively.

According to the principle in Section 2.3.2 and the measured angle difference data in Fig. 12, the sensitivity W_{AB} between points A and B is 47.082. Similarly, we can obtain the sensitivity W for other points, as shown in Table 4.

Despite the simplicity of the proposed method, the calibration data analysis results (Table 2) agree well with the measurement results of the cylindrical plano-convex lens data (Table 4), which verified the feasibility of the calibration for the sensitivity of the MBAS using cylindrical plano-convex lens.

3.4. Uncertainty budget for the sensitivity of MBAS from two experiments

To evaluate the developed methodology based on the calibration method using real datasets, the measurement uncertainties were also analyzed. Table 5 shows a list of all relevant uncertainty components for the calibration of the MBAS of the type, and states the estimates, the sensitivity coefficient function, and the resulting uncertainty contribution as standard uncertainty of the sensitivity (from Eq. (22)).

Explanations regarding the uncertainty components are:

(σ_{f_A}, σ_{f_B} and $\sigma_{d_{AB}}$) Calculation of the standard deviation of the mean value of typically 3–5 repeat measurements.

($f_A + f_B$ and d_{AB}) The sensitivity coefficient of the MABS according to Section 3.2 (Fig. 10).

($\sigma_{W_{AB}}$) According to Eq. (22), the total uncertainty contributions for the calibration of the sensitivity $\sigma_{W_{AB}}$ is $\pm 0.0270\,\text{mm}^2$, we find the biggest function standard deviation error is $\sigma_{d_{AB}}$.

Similarly, we can obtain uncertainty of the sensitivity for other points, as shown in Table 5.

Table 6 shows a list of all relevant uncertainty components for the cylindrical plano-convex lens measurement of the type, and states the estimates, the sensitivity coefficient function, and the resulting uncertainty contribution as standard uncertainty of the sensitivity (from Eq. (23)).

Explanations regarding the uncertainty components are:

(σ_R, σ_k, and $\sigma_{\Delta d_{AB}}$) Calculation of the standard deviation of the mean value of typically 3–5 repeat measurements. To evaluate the standard deviation for the radius of curvature R of the cylindrical plano-convex lens, an experiment was developed using conventional high-precision machines (MITUTOYO FALCIO707) to measure the same cylindrical plano-convex lens. It has a radius of curvature of 519.084 mm (the uncertainty of the measured radius $_R$ is 0.816 mm). Here, the indication accuracy of the MITUTOYO FALCIO707 is $(1.9 + 4L/1000)$ µm.

(Δd_{AB}) The sensitivity coefficient of the MABS according to Section 3.3 (Fig. 12).

($R + 2k$) Calculation of the mean value of typically 5–10 repeat measurements. The standard average value of the distance between the lens and aspheric surface k is 55.5 (in mm). Here, as shown in

Table 5
Uncertainty budget of the MBAS for plane mirror measurement (from Eq. (22)).

Type	Uncertainty component	Estimate/mm	Sensitivity coefficient	Estimate/mm	Uncertainty contribution/mm
σ_{f_A}	Standard deviation of the focal distance in point A	0.0000476	d_{AB}	0.511	0.0000243
σ_{f_B}	Standard deviation of the focal distance in point B	0.0000460	d_{AB}	0.511	0.0000235
$\sigma_{d_{AB}}$	Standard deviation of the lens spacing	0.0000293	$f_A + f_B$	92.114 $\sigma_{W_{AB}}/(\mathrm{mm}^2) = \pm 0.0270$	0.0270

Type	Uncertainty component	AB	BC	CD
$\sigma_W/(\mathrm{mm}^2)$	The standard deviation of the sensitivity	47.084 ± 0.0270	46.826 ± 0.0740	46.890 ± 0.0808

Table 6
Uncertainty budget of the MBAS for cylindrical plano-convex lens measurement (from Eq. (23) and the radius of curvature of the workpiece is 519 mm).

Type	Uncertainty component	Estimate/mm	Sensitivity coefficient	Estimate/mm	Uncertainty contribution/mm
σ_R	Standard deviation of the radius of curvature	0.816	Δd_{AB}	0.0747	0.0609
σ_k	Standard deviation of the distance between lens and workpiece surface	0.1	Δd_{AB}	0.0747	0.00747
$\sigma_{\Delta d_{AB}}$	Standard deviation of the differential spacing	0.00000169	$R+2k$	630 $\sigma_{W_{AB}}/(\mathrm{mm}^2) = \pm 0.0628$	0.00106

Type	Uncertainty component	AB	BC	CD
$\sigma_W/(\mathrm{mm}^2)$	The standard deviation of the sensitivity	47.082 ± 0.0628	46.847 ± 0.0624	46.930 ± 0.0626

Table 7
Uncertainty budget of the MBAS for cylindrical plano-convex lens measurement (from Eq. (23) and the radius of curvature of the workpiece is 363.3 mm).

Type	Uncertainty component	AB	BC	CD
$\sigma_W/(\mathrm{mm}^2)$	The standard deviation of the sensitivity	47.091 ± 0.0628	46.872 ± 0.0624	46.935 ± 0.0625

Table 3, the radius of curvature R of the cylindrical plano-convex lens is 519 (in mm).

($\sigma_{W_{AB}}$) According to Eq. (23), the same order of magnitude can be assigned to the bounds on the uncertainty of the sensitivity in $\pm 0.0628\ \mathrm{mm}^2$, where in the cylindrical plano-convex lens measurement, the biggest function standard deviation error is σ_R.

The uncertainty of the sensitivity is also measured for different curvature radii. Table 7 shows the uncertainty budget of the MBAS for the cylindrical plano-convex lens measurement when the radius of curvature of the workpiece is tuned to 363.3 mm. When the radius of curvature decreased, the uncertainty of the sensitivity decreased by several nanometers. Therefore, the calibration for the sensitivity of the MBAS can use cylindrical plano-convex lenses with different curvature radii.

Comparison of the two methods confirms that the second method (using cylindrical plano-convex lens) is more adapted for measurement with ultra high level of uncertainty. Further, the second method is simple, corresponding to a direct calculate in the sensitive parameters aiming to minimize the cost.

4. Conclusion

The results of this paper are summarized as follows:

(1) A high accuracy micro aspheric measuring machine (micro-AMM) for accurate measurement of the small aspheric profile has been proposed in this paper. The schematic of the micro-AMM includes three main parts: a multi-beam angle sensor (MBAS), a rotary unit, and a bearing system. The MBAS was developed to detect the differential of the local slope components (angle difference) of a point on the mirror surface and using Fourier series, we can obtain the profile data from the angle difference.

(2) To achieve the absolute accuracy of the flatness measurement under several tens nanometer, the sensitivity of MBAS should less than 0.5%. Therefore, for the determination of the sensitivity of MBAS, two independent calibration methods can be applied using plane mirror and cylindrical plano-convex lens has been proposed to measure the sensitivity of the MBAS. The measurement data analysis results using plane mirror agree well with the measurement results of the cylindrical plano-convex lens data, which verified the feasibility of the calibration for the sensitivity of MBAS using cylindrical plano-convex lens.

(3) To evaluate the developed methodology based on the calibration method using real datasets, the measurement uncertainties was also analyzed. We evaluated sensitivity for each lens-array; afterwards we investigated the influence of the function standard deviation error on the calibration measurement using plane mirror and the cylindrical plano-convex. The biggest function standard deviation errors are σ_d and σ_R in the calibration experiment and the cylindrical plano-convex lens measurement, respectively. Therefore, the precision of the radius of curvature (cylindrical plano-convex lens) may be the main reason for the calibration for the sensitivity of the MBAS.

Comparison of the two methods confirms that the second method (using cylindrical plano-convex lens) is more adapted for measurement with ultra high level of uncertainty. Further, the second method is simple, corresponding to a direct calculate in the sensitive parameters aiming to minimize the cost.

The uncertainty budget for the sensitivity of MBAS results is less than 0.5%, which also imply that the MBAS can measure flatness with repeatability under 50 nm.

References

Bručas, D., Giniotis, V., 2009a. Creation of multi-reference-angle comparator. Opt. Eng. 48 (3), 033602-1-4.

Bručas, D., Giniotis, V., 2009b. The construction and accuracy analysis of the multireference equipment for calibration of angle measuring instruments. In: Proceedings of XIX IMEKO World Congress, Fundamental and Applied Metrology, Lisbon, Portugal, pp. 1823–1837.

Bručas, D., Giniotis, V., 2010. Calibration of precision polygon/autocollimator measurement system. J. Phys. Conf. Ser. 2388, 1–7.

Chen, M.Y., Ueda, S., Takahashi, S., Takamasu, K., 2014. Measurement of surface roundness using a multi-beam angle sensor. In: 11th Laser Metrology for Precision Measurement and Inspection in Industry 2014, September 02–05, Tsukuba, Japan.

Chen, M.Y., Ueda, S., Takahashi, S., Takamasu, K., 2015a. Development of high-precision micro-roundness measuring machine using a high-sensitivity and compact multi-beam angle sensor. Precis. Eng. 42, 276–282.

Chen, M.Y., Takahashi, S., Takamasu, K., 2015b. Precision flatness measurement by an optical multi-beam angle sensor (1st report)—experimental verification of flatness measurement. JSPE Fall Conference, 133–134.

Chen, M.Y., Takahashi, S., Takamasu, K., 2016. Precision flatness measurement by an optical multi-beam angle sensor (2nd report)—calibration of the sensor and cylindrical surface measurement. JSPE Spring Conference, 47–48.

Chetwynd, D.G., Siddall, G.J., 1976. Improving the accuracy of roundness measurement. J. Phys. E: Sci. Instrum. 9, 537–544.

Clifford, A.A., 1973. Multivariate Error Analysis: a Handbook of Error Propagation and Calculation in Many-parameter Systems. John Wiley & Sons.

Ennos, A.E., Virdee, M.S., 1982. High accuracy profile measurement of quasi-conical mirror surfaces by laser autocollimation. Precis. Eng. 4, 5–8.

Ennos, A.E., Virdee, M.S., 1983. Precision measurement of surface form by laser autocollimation. Proc. SPIE Ind. Appl. Laser Technol. 0398 (October), 252.

Gao, Wei, Kiyono, Satoshi, 1997. Development of an optical probe for profile measurement of mirror surfaces. Opt. Eng. 36 (12), 3360–3366 http://dx.doi.org/10.1117/1.601563.

Gao, W., Huang, P.S., Yamada, T., Kiyono, S., 2002. Compact and sensitive two-dimensional angle probe for flatness measurement of large silicon wafers. Precis. Eng. 26, 396–3404.

ISO/IEC Guide 98-3:2008. Uncertainty of measurement—part 3: guide to the expression of uncertainty in measurement.

Just, A., Krause, M., Probstan, R., Wittekopf, R., 2003. Calibration of high-resolution autocollimators against an angle comparator. Metrologia 40, 288–294.

Just, A., Krause, M., Probst, R., Bosse, H., Haunerdinger, H., Spaeth, Ch., Metz, G., Israel, W., 2009. Comparison of angle standards with the aid of a high-resolution angle encoder. Precis. Eng. 33, 530–533, http://dx.doi.org/10.1016/j.precisioneng.2009.02.004.

Ku, H.H., 1966. Notes on the use of propagation of error formulas. J. Res. Natl. Bur. Stand. 70C (October (4)), 262, http://dx.doi.org/10.6028/jres.070c.025, ISSN 0022-4316 (retrieved 3.10.12.).

Probst, R., 2008. Self-calibration of divided circles on the basis of a prime factor algorithm. Meas. Sci. Technol. 19, 015101.

Probst, R., Wittekopf, R., Krause, M., Dangschat, H., Ernst, A., 1998. The New PTB Angle Comparator Measurement Science Technology, 9. IOP Publishing, p. 1059–1066.

Vissiere, A., Nouira, H., Damak, M., Gibaru, O., David, J.-M., 2012. A newly conceived cylinder measuring machine and methods that eliminate the spindle errors. Meas. Sci. Technol. 23, 094015.

Whitehouse, D.J., 1974. The measurement and analysis of surfaces. Tribology, 249–259.

Whitehouse, D.J., 1976. Some theoretical aspects of error separation techniques in surface metrology. J. Phys. E: Sci. Instrum. 9, 531–536.

Xiao, M., Jujo, S., Takahashi, S., Takamasu, K., 2012. Nanometer profile measurement of large aspheric optical surface by scanning deflectometry with rotatable devices: uncertainty propagation analysis and experiments. Precis. Eng. 36, 91–96.

Yandayan, T., Ozgur, B., Karaboce, N., Yaman, O., 2011. High precision small angle generator for realization of SI unit of plane angle and calibration of high precision autocollimators. Proceedings of Macroscale.

Optics and Photonics Journal, 2016, 6, 8-13
Published Online August 2016 in SciRes. http://www.scirp.org/journal/opj
http://dx.doi.org/10.4236/opj.2016.68B002

Scientific Research Publishing

Is the Two-Color Method Superior to Empirical Equations in Refractive Index Compensation?

Dong Wei[1*], Kiyoshi Takamasu[2], Hirokazu Matsumoto[2]

[1]Department of Mechanical Engineering, Nagaoka University of Technology, Nagaoka City, Japan
[2]Department of Precision Engineering, The University of Tokyo, Tokyo, Japan
Email: *weidong@mech.nagaokaut.ac.jp

Received 6 April 2016; accepted 19 August 2016; published 25 August 2016

Abstract

The Edlén empirical equations and the two-color method are the commonly used approaches to converting a length measured in air to the corresponding length in vacuum to eliminate the influence of the refractive index of air. However, it is not well known whether the two-color method is superior to empirical equations in refractive index compensation. We investigated the uncertainties of these approaches via numerical calculations of their sensitivity coefficients of environmental parameters. On the basis of a comparison of their uncertainties, we found that in a 0% humidity environment, the two-color method had potential to provide greater measurement accuracy than the empirical equations.

Keywords

Two-Color Method, Length Measurement, Sensitivity Coefficient, Uncertainty, Empirical Equations

1. Introduction

Meter, the unit of length, is defined in vacuum. However, measurements of length are often carried out in air, which presents some problems. Let us assume that we want to compare two geometric distances G_1 and G_2. These two distances are measured in air as $L_1 = G_1 \times n_1$ and $L_2 = G_2 \times n_2$, where n_1 and n_2 are the refractive index of air (RIA). In the absence of a relationship between n_1 and n_2, it is not possible to determine which of G_1 and G_2 is greater only by judging the magnitude relationship between L_1 and L_2. To solve this problem, the influence of RIA must be eliminated.

One approach to obtaining the value of RIA is to use empirical equations [1]-[4]. With n obtained, an estimate of the geometric distance $G = L / n$ can be calculated. The estimated geometric distance can be used for comparison. The empirical equations are used to compensate for the RIA under two assumptions. First, environmental parameters (namely, temperature, pressure, and humidity) can be measured. Second, a measured environmental parameter is a good reproduction of that parameter along the optical path, meaning that a measured en-

*Corresponding author.

How to cite this paper: Wei, D., Takamasu, K. and Matsumoto, H. (2016) Is the Two-Color Method Superior to Empirical Equations in Refractive Index Compensation? *Optics and Photonics Journal*, **6**, 8-13.
http://dx.doi.org/10.4236/opj.2016.68B002

vironmental parameter is an average value over time and space. In other words, both the spatial distribution of environmental parameters and the time-delay of measurement equipment can be ignored. These assumptions are valid only if the measurement is performed in a closed environment (e.g., a well-controlled laboratory or underground tunnel with limited variation in environmental parameters).

Another approach to suppressing the influence of RIA is to apply the two-color method, which was first proposed by Bender and Owens [5] to compensate for the inhomogeneous disturbances of the RIA in an open environment. The core concept of the two-color method is to use a measured length difference between two colors (frequencies) to render length measurements less sensitive to changes in the RIA.

Recently, high-precision length measurements based on fem to second optical frequency comb (FOFC) have been carried out (e.g., [6] [7]). To compensate for the RIA, FOFC-based RIA measurements [8] [9] and FOFC-based two-color method experiments [10]-[12] have also been performed. Minoshima's group performed a two-color method experiment in a well-controlled environment and found an agreement between RIA compensation based on the empirical equations and that of two-color method with a standard deviation of 3.8×10^{-11} throughout hours [13]. They also suggested that the accuracy provided by the empirical equations may be improved by the two-color method.

One question arises naturally: theoretically, is the two-color method superior to the empirical equations in RIA compensation? We employed a numerical approach to investigate this possibility.

2. Methods

2.1. Refraction Index Compensation by Empirical Equations

The distance between two points measured in air is an optical distance L_{air}. An estimate of the geometric distance G_{est_λ} in vacuum and the optical distance has the following relationship.

$$G_{\text{est}_\lambda} = L_{\text{air}} / n \tag{1}$$

where n represents the RIA. By applying the law of propagation of uncertainty [14] [15] to Equation (1), we obtain the uncertainty of length in vacuum.

$$u(G_{\text{est}_\lambda})^2 = \{[u(n)/n] \times G_{\text{est}_\lambda}\}^2 + \{[u(L_{\text{air}_1})/L_{\text{air}_1}] \times G_{\text{est}_\lambda}\}^2 \tag{2}$$

where $u(x)$ denotes the uncertainty of variable x. The first and second terms of the right-hand side of Equation (2) are the uncertainty due to the refractive index and the length measurement, respectively. These two are defined as follows, respectively.

$$u_n(G_{\text{est}_\lambda}) = [u(n)/n] \times G_{\text{est}_\lambda} \tag{3}$$

$$u_L(G_{\text{est}_\lambda}) = [u(L_{\text{air}_1})/L_{\text{air}_1}] \times G_{\text{est}_\lambda} \tag{4}$$

The uncertainty of refractive index can be evaluated by the following equation [16] [17].

$$u(n) = \sqrt{K_{\text{T}_0}^2 u^2(T_0) + K_{\text{P}_0}^2 u^2(P_0) + K_{\text{H}_0}^2 u^2(H_0)} \tag{5}$$

where $u(T)$, $u(P)$, and $u(H)$ are the uncertainties of the instrument for measuring temperature T, barometric pressure P, and humidity H, respectively. K_{T}, K_{P}, and K_{H} are sensitivity coefficients and defined as follows.

$$K_{\text{T}_0} = (dn/dT)_{T_0}, K_{\text{P}_0} = (dn/dP)_{P_0}, K_{\text{H}_0} = (dn/dH)_{H_0} \tag{6}$$

where $(dn/dT)_{T_0}$ is the derivative of function $\text{y} = n(T, P, H)$ at $T = T_0$. The definitions are similar for $(dn/dP)_{P_0}$ and $(dn/dH)_{H_0}$.

2.2. Refraction Index Compensation by Two-Color Method

The distances between two points measured in air by using different wavelengths are optical distances L_{air_1} and L_{air_2}. An estimate of the geometric distance $G_{\text{est}_2\lambda}$ from these two optical distances can be obtained as follows:

$$G_{\mathrm{est_2}\lambda} = L_{\mathrm{air_2}} - A \times (L_{\mathrm{air_2}} - L_{\mathrm{air_1}}) \tag{7}$$

where A is the so-called A-factor defined as

$$A = [n(\lambda_{\mathrm{vac_2}}, T, P, H) - 1] / [n(\lambda_{\mathrm{vac_2}}, T, P, H) - n(\lambda_{\mathrm{vac_1}}, T, P, H)] \tag{8}$$

Equation (7) can be rewritten as follows.

$$G_{\mathrm{est_2}\lambda} = A \times L_{\mathrm{air_1}} + (1 - A) \times L_{\mathrm{air_2}} \tag{9}$$

By applying the law of propagation of uncertainty to Equation (9), we have

$$u(G_{\mathrm{est_2}\lambda})^2 = u(A \times L_{\mathrm{air_1}})^2 + u[(1 - A) \times L_{\mathrm{air_2}}]^2 \tag{10}$$

The uncertainties of the first and second terms of the right-hand side of Equation (10) are, respectively,

$$[u(A \times L_{\mathrm{air_1}}) / A \times L_{\mathrm{air_1}}]^2 = [u(A) / A]^2 + [u(L_{\mathrm{air_1}}) / L_{\mathrm{air_1}}]^2 \tag{11}$$

$$\{u[(1 - A) \times L_{\mathrm{air_2}}] / [(1 - A) \times L_{\mathrm{air_2}}]\}^2 = [u(1 - A) / (1 - A)]^2 + [u(L_{\mathrm{air_2}}) / L_{\mathrm{air_2}}]^2 \tag{12}$$

Because we have $u(1 - A)^2 = u(1)^2 + u(A)^2 = u(A)^2$, Equation (12) can be rewritten as follows.

$$\{u[(1 - A) \times L_{\mathrm{air_2}}] / [(1 - A) \times L_{\mathrm{air_2}}]\}^2 = [u(A) / (1 - A)]^2 + [u(L_{\mathrm{air_2}}) / L_{\mathrm{air_2}}]^2 \tag{13}$$

By substituting Equations (11) and (13) into Equation (10), we obtain

$$u(G_{\mathrm{est_2}\lambda})^2 = [u(A) \times L_{\mathrm{air_1}}]^2 + [u(L_{\mathrm{air_1}}) \times A]^2 + [u(A) \times L_{\mathrm{air_2}}]^2 + [u(L_{\mathrm{air_2}}) \times (1 - A)]^2 \tag{14}$$

The first and third terms of the right-hand side of Equation (14) are the uncertainty due to the A-factor, and the second and fourth terms are the uncertainty due to the length measurement. These two are defined as follows, respectively.

$$u_A(G_{\mathrm{est_2}\lambda}) = \sqrt{[u(A) \times L_{\mathrm{air_1}}]^2 + [u(A) \times L_{\mathrm{air_2}}]^2} \tag{15}$$

$$u_L(G_{\mathrm{est_2}\lambda}) = \sqrt{[u(L_{\mathrm{air_1}}) \times A]^2 + [u(L_{\mathrm{air_2}}) \times (1 - A)]^2} \tag{16}$$

The uncertainty of A-factor is as follows.

$$u(A) = \sqrt{K_{\mathrm{A_T_0}}^2 u^2(T_0) + K_{\mathrm{A_P_0}}^2 u^2(P_0) + K_{\mathrm{A_H_0}}^2 u^2(H_0)} \tag{17}$$

where $K_{\mathrm{A_T}}$, $K_{\mathrm{A_P}}$, and $K_{\mathrm{A_H}}$ are the sensitivity coefficients of the A-factor and are defined as follows.

$$K_{\mathrm{A_T_0}} = (dA / dT)_{T_0}, K_{\mathrm{A_P_0}} = (dA / dP)_{P_0}, K_{\mathrm{A_H_0}} = (dA / dH)_{H_0} \tag{18}$$

where $(dA/dT)_{T_0}$ is the derivative of function $y = A(T, P, H)$ at $T = T_0$. The definitions are similar for $(dA/dP)_{P_0}$ and $(dA/dH)_{H_0}$.

2.3. Comparison of Empirical Equations and Two-Color Method

In Equation (4), the uncertainty due to the length measurement is multiplied by the factor $G_{\mathrm{est_}\lambda} / L_{\mathrm{air_1}} = n \approx 1$. In Equation (16), the uncertainty due to the length measurement is multiplied by two factors, A and $1 - A$. Normally, their orders are several tens. If the two wavelengths used in the two-color method are 780 nm and 1560 nm, then $A \approx 141$ and $1 - A \approx -140$. By comparing the magnitudes of Equation (4) and Equation (16), we understand that only when the condition

$$[u_A(G_{\mathrm{est_2}\lambda})]^2 < [u_n(G_{\mathrm{est_}\lambda})]^2 \tag{19}$$

is satisfied, the two-color method can be shown to obtain measurements with a smaller error than that of the empirical equations. We performed numerical calculations to check whether Equation (19) is feasible.

3. Numerical Calculations

We used the following parameters for simulation. By referring to Ref. [18], we employed 780.0 nm and 1560.0

nm as the two wavelengths. We used the equations for the phase refractive index given in Ref. [4]. Because of the limit on the length of this paper, we only considered the Edlén empirical equations in this study. In the Edlén empirical equations [2]-[4], the RIA can be derived from the wavelength in vacuum λ, temperature *T*, barometric pressure *P*, and humidity *H* as $n = f(\lambda, T, P, H)$. The formula used to perform the calculations can be easily accessed via the internet [4]. In the following, we only consider the phase refractive index. The group refractive index can be treated in the same way.

On the basis of Equations (6) and (18), we calculated the change in the sensitivity coefficients when environmental parameters change in a realistic range ($T \in [10, 30]$ ˚C, $P \in [90,115]$ kPa, $H = 0\%$). The calculations of the derivative of each refractive index have been validated in Ref. [19]. The same procedure was used in this study for calculating the derivative of the *A*-factor. After obtaining an expression for the sensitivity coefficients by substituting numerical values, the values of sensitivity coefficients were calculated.

As shown in **Figure 1**, when $H = 0\%$, the sensitivity coefficient of the *A*-factor is smaller than that of the refractive indices. This result, *i.e.*, the *A*-factor can be considered as a function of just two wavelengths only when the humidity is 0%, is consistent with the results of previous studies [10] [11] [13] [20]-[24].

On the basis of Equations (3) and (15), we calculated the uncertainties due to the *A*-factor and refractive indices, respectively. The geometric distance *G* was set to 1 m. We assumed that $u(T) = 0.1^{\circ}\text{C}$ and $u(P) = 0.01\,\text{kPa}$ on the basis of using a thermometer (Testo 735, Testo) and a barometer (VR-18, Sunoh), respectively. These two are commercially available for us.

Figure 2 shows that $u_A(G_{\text{est_}2\lambda}) < u_n(G_{\text{est_}\lambda})$. This result means that in a 0% humidity environment, the two-color method has potential to provide greater measurement accuracy than the empirical equations. Note that the orders of values shown in **Figure 2** were affected by the sensitivity coefficients of environmental parameters and the uncertainties of the instrument for measuring environmental parameters. A detailed uncertainty analysis in an environment where the humidity is not 0% will be reported in another paper.

4. Conclusion

We analyzed the uncertainties of length conversion based on the Edlén empirical equations and the two-color

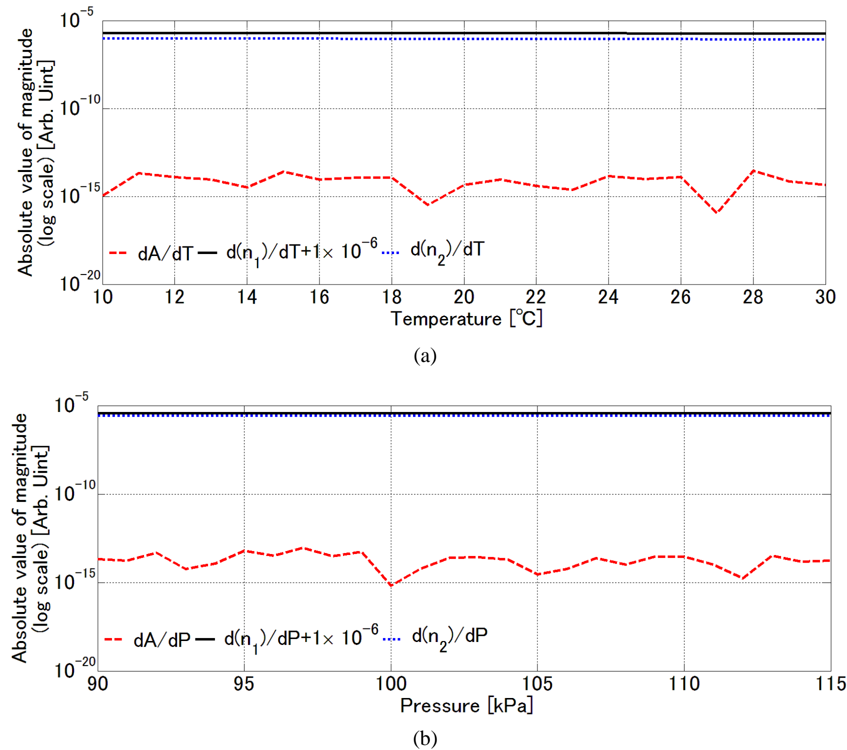

Figure 1. Change in sensitivity coefficients of *A*-factor and refractive indices with (a) temperature when $P = 101.325$ kPa and $H = 0\%$ and (b) pressure when $T = 20^{\circ}$C and $H = 0\%$.

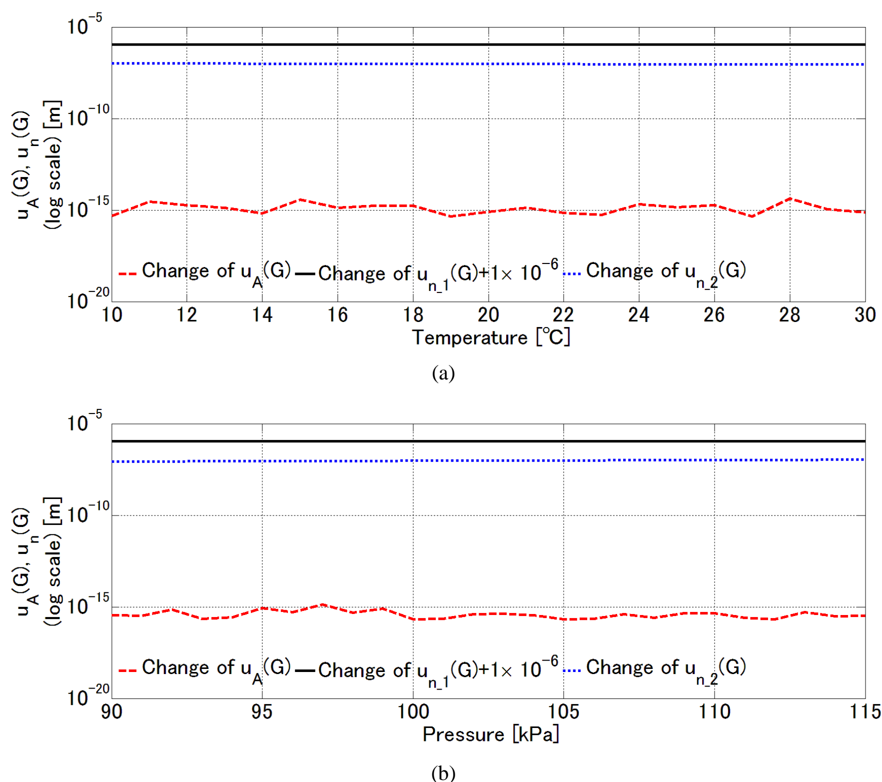

Figure 2. Change in uncertainties due to*A*-factor and refractive indices with (a) temperature when P = 101.325 kPa and H = 0% and (b) pressure when T = 20˚C and H = 0%.

method, in which the uncertainties due to length measurement and refractive index compensation were decomposed. Using numerical calculations of sensitivity coefficients of the *A*-factor and refractive indices of the environmental parameters, we found for the first time that in a realistic environmental parameter range ($T \in [10, 30]$ ˚C, $P \in [90, 115]$ kPa, $H = 0\%$), the uncertainty of the two-color method due to the *A*-factor was smaller than that of the empirical equations due to refractive indices. This result suggests that in a 0% humidity environment, the two-color method has potential to provide greater measurement accuracy than the empirical equations, with the cooperation of suppressing the uncertainties of length measurements (compared with uncertainties of refractive index compensation) to a negligible level. The findings of this study provide a better insight into the two-color method, and will create opportunities for further development of application of this method.

Acknowledgements

This research work was partially financially supported by a grant (R1501) from the Mitutoyo Association for Science and Technology.

References

[1] Ciddor, P.E. (1996) Refractive Index of Air: New Equations for the Visible and Near Infrared. *Appl. Opt*, **35**, 1566-1573. http://dx.doi.org/10.1364/ao.35.001566

[2] Birch, K.P. and Downs, M.J. (1993) An Updated Edlén Equation for the Refractive Index of Air. *Metrologia*, **30**, 155. http://dx.doi.org/10.1088/0026-1394/30/3/004

[3] Bengt, E. (1966) The Refractive Index of Air. *Metrologia*, **2**, 71. http://dx.doi.org/10.1088/0026-1394/2/2/002

[4] Stone, J.A. and Zimmerman, J.H. Refractive Index of Air Calculator. http://emtoolbox.nist.gov/Wavelength/Edlen.asp

[5] Bender, P.L. and Owens, J.C. (1965) Correction of Optical Distance Measurements for the Fluctuating Atmospheric Index of Refraction. *J. Geophys. Res*, **70**, 2461-2462. http://dx.doi.org/10.1029/JZ070i010p02461

[6] Coddington, I., Swann, W.C., Nenadovic, L. and Newbury, N.R. (2009) Rapid and Precise Absolute Distance Mea-

surements at Long Range. *Nat Photon*, **3**, 351-356. http://dx.doi.org/10.1038/nphoton.2009.94

[7] Lee, J., Kim, Y.-J., Lee, K., Lee, S. and Kim, S.-W. (2010) Time-of-Flight Measurement with Femtosecond Light Pulses. *Nat Photon*, **4**, 716-720. http://dx.doi.org/10.1038/nphoton.2010.175

[8] Zhang, J., Lu, Z.H. Menegozzi, B. and Wang, L.J. (2006) Application of Frequency Combs in the Measurement of the Refractive Index of Air. *Rev. sci. instrum*, **77**, 083104-083105. http://dx.doi.org/10.1063/1.2239036

[9] Zhang, J., Lu, Z.H. and Wang, L.J. (2007) Precision Measurement of the Refractive Index of Carbon Dioxide with a Frequency Comb. *Opt. Lett*, **32**, 3212-3214. http://dx.doi.org/10.1364/OL.32.003212

[10] Minoshima, K. and Matsumoto, H. (2000) High-Accuracy Measurement of 240-m Distance in an Optical Tunnel by use of a Compact Femtosecond Laser. *Appl. Opt*, **39**, 5512-5517. http://dx.doi.org/10.1364/AO.39.005512

[11] Meiners-Hagen, K. and Abou-Zeid, A. (2008) Refractive Index Determination in Length Measurement by two-Colour Interferometry. *Meas. Sci. Technol*, **19**, 084004. http://dx.doi.org/10.1088/0957-0233/19/8/084004

[12] Kang, H.J., Chun, B.J., Jang, Y.-S., Kim, Y.-J. and Kim, S.-W. (2015) Real-Time Compensation of the Refractive Index of Air in Distance Measurement. *Opt. Express*, **23**, 26377-26385. http://dx.doi.org/10.1364/OE.23.026377

[13] Wu, G., Arai, K., Takahashi, M., Inaba, H. and Minoshima, K. (2013) High-Accuracy Correction of Air Refractive Index by Using Two-Color Heterodyne Interferometry of Optical Frequency Combs. *Meas. Sci. Technol*, **24**, 015203. http://dx.doi.org/10.1088/0957-0233/24/1/015203

[14] Coleman, H.W. and Steele, W.G. (1999) Experimentation and Uncertainty Analysis for Engineers, A Wiley Interscience publication. Wiley.

[15] Walter, B. Maurice, G.C. and Peter, M.H. (2006) Evolution of the "Guide to the Expression of Uncertainty in Measurement". *Metrologia*, **43**, S161. http://dx.doi.org/10.1088/0026-1394/43/4/S01

[16] Kevin, H. (2013) Handbook of Optical Dimensional Metrology, Series in Optics and Optoelectronics. Taylor & Francis.

[17] Ellis, J.D. (2014) Field Guide to Displacement Measuring Interferometry, The Field Guide Series. SPIE, Bellingham. http://dx.doi.org/10.1117/3.1002328

[18] Wu, G., Takahashi, M., Arai, K., Inaba, H. and Minoshima, K. (2013) Extremely High-Accuracy Correction of Air Refractive Index Using Two-Colour Optical Frequency Combs. *Sci. Rep*, **3**.

[19] Wei, D. and Aketagawa, M. (2015) Uncertainty in Length Conversion due to Change of Sensitivity Coefficients of Refractive Index. *Opt. Commun*, **345**, 67-70. http://dx.doi.org/10.1016/j.optcom.2015.01.070

[20] Ishida, A. (1989) Two-Wavelength Displacement-Measuring Interferometer Using Second-Harmonic Light to Eliminate Air-Turbulence-Induced Errors. *Jpn. J. Appl. Phys*, **28**, L473. http://dx.doi.org/10.1143/jjap.28.l473

[21] Matsumoto, H. and Honda, T. (1992) High-Accuracy Length-Measuring Interferometer Using the two-Colour Method of Compensating for the Refractive Index of Air. *Meas. Sci. Technol*, **3**, 1084. http://dx.doi.org/10.1088/0957-0233/3/11/011

[22] Matsumoto, H., Zhu, Y., Iwasaki, S. and Oishi, T. (1992) Measurement of the Changes in Air Refractive Index and Distance by Means of a Two-Color Interferometer. *Appl. Opt*, **31**, 4522-4526. http://dx.doi.org/10.1364/AO.31.004522

[23] Golubev A.N. and Chekhovsky, A.M. (1994) Three-Color Optical Range Finding. *Appl. Opt*, **33**, 7511-7517. http://dx.doi.org/10.1364/AO.33.007511

[24] Minoshima, K., Arai, K. and Inaba, H. (2011) High-Accuracy Self-Correction of Refractive Index of Air Using Two-Color Interferometry of Optical Frequency Combs. *Opt. Express*, **19**, 26095-26105. http://dx.doi.org/10.1364/OE.19.026095

Submit or recommend next manuscript to SCIRP and we will provide best service for you:

Accepting pre-submission inquiries through Email, Facebook, LinkedIn, Twitter, etc.
A wide selection of journals (inclusive of 9 subjects, more than 200 journals)
Providing 24-hour high-quality service
User-friendly online submission system
Fair and swift peer-review system
Efficient typesetting and proofreading procedure
Display of the result of downloads and visits, as well as the number of cited articles
Maximum dissemination of your research work

Submit your manuscript at: http://papersubmission.scirp.org/

DOI: 10.1007/s12541-016-0133-6 ISSN 2234-7593 (Print) / ISSN 2005-4602 (Online)

Multi-Beam Angle Sensor for Flatness Measurement of Mirror using Circumferential Scan Technology

Meiyun Chen[1,#], Satoru Takahashi[2], and Kiyoshi Takamasu[1]

1 Faculty of Engineering, Department of Precision Engineering, The University of Tokyo, 7-3-1 Hongo, Bunkyo-ku, Tokyo, 113-8656, Japan
2 Research Center for Advanced Science and Technology, The University of Tokyo, 4-6-1 Komaba, Meguro-ku, Tokyo, 153-8904, Japan
Corresponding Author / E-mail: chenmeiyun@nanolab.t.u-tokyo.ac.jp, TEL: +81-03-5841-6472, FAX: +81-03-5841-6472

KEYWORDS: Micro-FMM, Multi-beam angle sensor, Flatness, Autocollimator, Stage-independence

Flatness tolerance of mirror is usually determined for a particular manufactured product based on the user's requirement. To help meet this requirement, we here propose a high-accuracy microscale flatness-measuring machine (micro-FMM) that consists of a multi-beam angle sensor (MBAS). We review the techniques and the sensors predominantly used in the industry to quantify flatness. Compared with other methods, the MBAS can eliminate zero-difference error by circumferential scan and automatically eliminates the tilt error caused by the rotation of a workpiece. Our optical probe uses the principle of an autocollimator, and the flatness measurement of the mirror comprises two steps. First, the MBAS is designed to rotate around a circle with a given radius. The workpiece surface profile along this trajectory is then measured by the micro-FMM. Experimental results, confirming the suitability of the MBAS for measuring flatness are also presented.

Manuscript received: January 21, 2016 / Revised: May 2, 2016 / Accepted: May 3, 2016

1. Introduction

Surface flatness of mirror is a critical feature in many industrial and commercial devices and instruments. A flat surface often serves as a reference against which to inspect other workpieces. The ISO 1101[1] standard for flatness tolerance quantifies flatness in terms of the space bounded by two parallel planes separated by *t*. This distance must meet application-specific requirements.[2]

Surface flatness of mirror can be assessed in various ways, some similar to straightness. A traditional approach involves sweeping the test surface in several places with a straight edge and observing where and how much light leaks through the contact region. This method suffers from any deviation in the straightness of the edge and from the diffraction of any light transmitted through even a very small gap. The edge must also be rotated on the surface to ensure true planarity.[3] Other techniques of measuring flatness such as coordinate-measuring machines (CMM) , the least-square arithmetic was applied in flatness based on CMM,[4] but there is a discrepancy in assessment the uncertainty, such as in referents.[5-7] Optical measurement methods have also been reported,[8-10] some based on interferometry.[11,12] However, interferometry technique is viable and does produce, under certain conditions, absolute values. Yokoyama proposed a novel interferometric measurement method using two heterodyne shearing interferometers.[13] Although this technique is robust and precise under general environment, the measurement curvature-range is limited, as the variation of curvature is not allowed to be too high.

Another technique, involving the use of an autocollimator,[14-17] yields notoriously high resolution and accuracy. When applied to a large work piece, many sensors are normally used to determine position coordinates. The scanning multi-probe system, consisting of two probe units of the three-probe method, whose straightness profile was evaluated with an accuracy of approximately 0.4 μm over a measurement length of 600 mm.[18] This widely used technique face the problem of the zero difference error; they carried out an accurate zero-adjustment by two probe-units (six sensors). This poses a problem that the probe non-linearity error (the main error sources) will generate in the zero-adjustment.[18]

Ikumatsu proposed the circumferential scan technique (used three displacement sensors) to measure the flatness, which verified can automatically reduce the zero-difference error.[19,20] However he only shows results of this study through theoretical analysis.

We therefore designed and built a simple but accurate small-angle generator using a multi-beam angle sensor (MBAS). Its dimensions are 125(L) mm × 130(W) mm × 90(H) mm. The flatness measurement of

© KSPE and Springer 2016 Springer

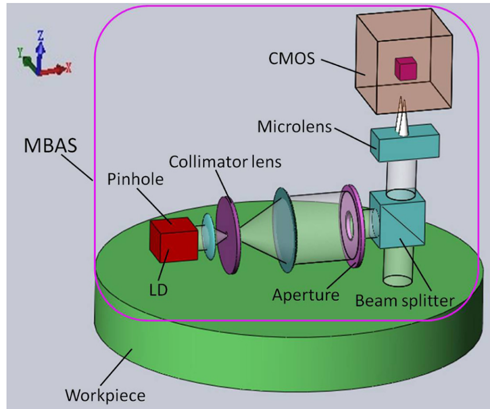

Fig. 1 Construction of the MBAS

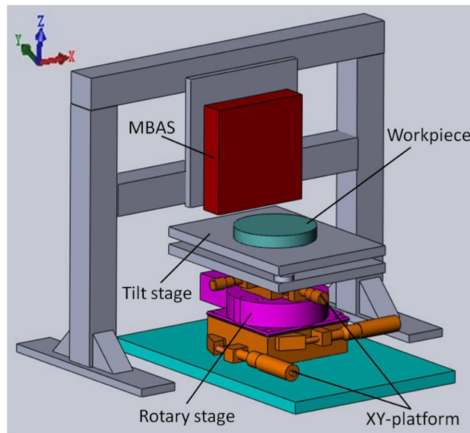

Fig. 2 Schematic of the micro-FMM: multi-beam angle sensor (MBAS), tilt stage, rotary unit, XY-platforms, and a support structure for holding the MBAS

the mirror comprises two steps. First, the MBAS is designed to rotate around a circle with a given radius. The workpiece surface profile along this trajectory is then measured by the micro-FMM. Compared with other methods, the MBAS can eliminate zero-difference error by circumferential scan and automatically eliminates the tilt error caused by the rotation of a workpiece. Experimental results, confirming the suitability of the MBAS for measuring flatness are also presented.

2. Micro-FMM Configuration

An autocollimator is an optical instrument that performs non-contact angle measurements at a reflecting surface. The MBAS is based on a multi-autocollimator system using microlenses to measure deflections in an optical system. It works by projecting an image onto a beam splitter, and measuring the deflection of the light reflected from the surface. The deflection of the light reflected at several points on the surface can be measured with a sensor. Then, the sensor is scanning the workpiece while it is rotating.

Fig. 1 illustrates the MBAS optical system. The laser beam from a

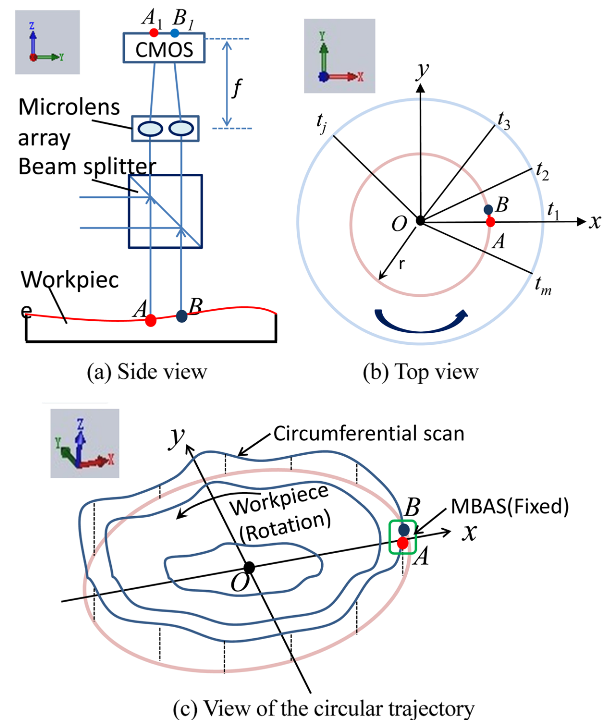

Fig. 3 Profile measurement along the circumference of a circle of radius r: the multi-beam angle sensor is fixed onto the support structure and scanning the workpiece while it is rotating. (a) Side view. (b) Top view. (c) Overall view of the measurement scans on concentric circles

laser diode (LD) passes through a pinhole and is collimated by a collimator lens. The beam is then reflected by a beam splitter and projected onto the workpiece surface. All of the beam reflected from the workpiece surface traverses the beam splitter to reach the microlens. After being focused by the microlens, it is split into several beams. The resulting pattern is observed and recorded by a CMOS camera oriented vertically, and the imaging can be observed on a TV monitor. Further processing of the pattern is carried out on a PC.

We used an MBAS to construct the experimental system shown in Fig. 2. A workpiece was placed on the tilt stage and the rotary platform was mounted between two XY-platforms. Thus, the rotary table acts as a small-angle generator and serves to set the reference position for the angle measurements. The MBAS was arranged to rotate around the circumference of a circle from the rotational center point. We then measured the workpiece surface profile along the circle by rotating the workpiece in increments.

3. Principle of the MBAS

3.1 Measurement of the angle difference *c*

The measurement of the angle difference involves two steps. First, the MBAS is placed so as to rotate around the circumference of a circle of radius r centered on point O on the workpiece surface. Then, the workpiece surface profile is measured along the circumference by rotating the workpiece in increments, as shown in Fig. 3. The workpiece flatness is determined in these two steps by the proposed algorithm.

Further details will be given in Section 4. One commonly used method for assessing surface flatness uses three sensors[18] that can measure distances relative to a fixed internal reference plane. However, this method is susceptible to tilt error and zero-difference error, i.e., discrepancies between the zero values of each sensor. The MBAS was designed to address this problem by eliminating the significance of the zero-difference error (Fig. 3) and automatically eliminating the significance of the tilt error that originates from the rotation of the workpiece (Fig. 5).

The MBAS uses a CMOS to capture the spot pattern produced by a microlens. See Fig. 3(a) for a schematic of the side view of the flatness measurement system. Here, *f* is the focal distance of the microlens and r the radius of measurement.

In the XY plane (Fig. 3(b)), the workpiece is rotated in angular increments of *è*, with the MBAS initially oriented perpendicular to the *x* axis. Flatness is then measured along the straight line passing through the center of rotation, *O*. Fig. 3(c) illustrates how the two points *A* and *B* in the circumference of the circle of radius *r* are carried out by rotating the workpiece step by step.[19] The workpiece flatness is calculated by applying the autocollimator principle of the angle difference at each of these two angles on the workpiece. The angle difference can be calculated from the intensity distribution of the spots on the CMOS.[21] Then, the specimen profile at each location on the circle can be determined accurately. This procedure is repeated for circular scans of different radii, to yield the overall shape of the surface.

In the flatness measurement, the profile *P* can be denoted as the second order integration of the angle differential output *c* (the mathematical algorithm is shown in section 3.2), if the zero difference error c_0 is zero (the difference between the zero-value of the two angles will generate an offset c_0 in the angle differential output). However, if the c_0 is not equated zero, the second order integration of the offset c_0 will yield a quadratic curve in the profile evaluation. Generally known is the use of the three sensors for the purpose of determining the flatness of a surface. This widely used technique also face this problem, they carried out an accurate zero-adjustment by two probe-units (six sensors). This poses a problem that the probe non-linearity error (the main error sources) will generate in the zero-adjustment.[18]

In order to circumvent the problem of the zero-difference error mentioned in the last paragraph, we proposed the circumferential scan technique. Through one circumferential scanning (rotate 360 degree), suppose the first and last position is the same one, by the proposed algorithm (Fourier transform), which can automatically reduce the influence of zero-difference error. Ikumatsu also proposed the circumferential scan technique (used three displacement sensors) to measure the flatness, which verified can automatically reduce the zero-difference error.[19]

Fig. 4 outlines the principle of the angle-difference measurement by the MBAS. A_1 and B_1 are representative points on the workpiece at the rotation angle t_1 (as shown in the Fig. 3(b)), and c_{a1} and c_{b1} are the corresponding angles. Then, c is the angle difference between points A_1 and B_1. Here, A_0 and B_0 represent predetermined surface location of the points A_1 and B_1, and c_{a0} and c_{b0} are the corresponding angles. When the separation between A_1 and B_1 changes from x_0 to x_1, the relationship between the surface gradient in the Y direction and the reflected beams must be determined.

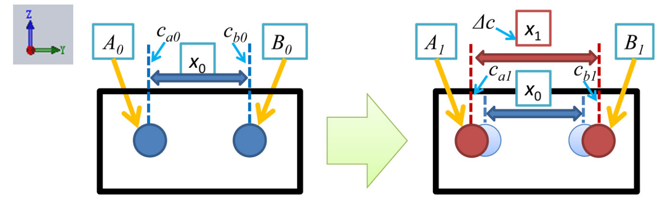

Fig. 4 Calculation of the angle difference from the intensity distribution of the center of the overall intensity distribution

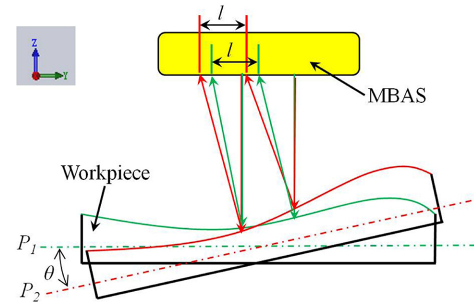

Fig. 5 Relation between surface curvature in the *Y* direction and the reflected beams: the green and red lines denote, respectively, the reference and the actual plane, tilted by angle *è* and the distance between the two reflected laser beams from P_1 plane is *l*

The MBAS is based on the autocollimator principle. An autocollimator measuring the distance between two reflected beams, which provides a measure of the angle difference of the workpiece. Assume that, as shown in Fig. 5, the green and red beams originate from planes P_1 and P_2, respectively. The distance between the two reflected laser beams from P_1 plane is *l*. When the surface tilts in the *Y* direction by an angle θ from plane P_1 to P_2, the positions of the two reflected beams from plane P_2 also changes. Relative to the reference plane P_1, plane P_2 is tilted by an angle θ, but the distance between the two reflected beams remains equal to *l*. Similar to autocollimators, the distance *l* provides a measure of the angle difference. Thus, the angle difference is unchanged by a change in gradient in the *Y* direction. The tilt error caused by the rotation is therefore negligible and the specimen profile can be measured accurately on each concentric circle.

3.2 Calculating the profile P from the angle difference *c*

Fig. 6 outlines the measurement algorithm. The profile *P* of a workpiece at a location *t* can be expressed as a Fourier series, given by

$$P(t_j) = a_0 + \sum_{i=1}^{n}(a_i \cos t_j i + b_i \sin t_j i) \qquad t_j = \frac{2\pi(j-1)}{m} \tag{1}$$

$$(j = 1, 2, \ldots, m)$$

where a_i and b_i are the Fourier series coefficients, *n* the maximum iterations of the Fourier series, and *m* the number of sample points. Here, the angle difference *c* can be measured by the sensor, and can also be expressed as the second order differential of the profile data *P*, given by

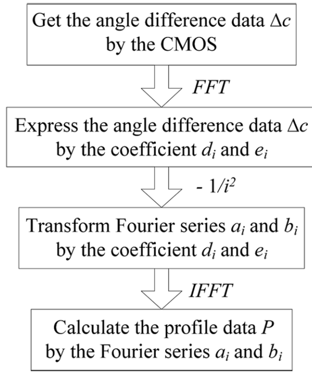

Fig. 6 Measurement flowchart: from the angle difference c to the profile data P via Fourier series

$$\Delta c(t_j) = P''(t_j) = -\sum_{i=1}^{n} i^2 (a_i \cos t_j i + b_i \sin t_j i) \tag{2}$$

Then, using a Fourier transformation, we can also transform the angle difference c to coefficients d_i and e_i, given by

$$c_j = \sum_{i=1}^{n} (d_i \cos t_j i + e_i \sin t_j i) = P''(t_j) \tag{3}$$

We note that the relationship between the Fourier series (a_i and b_i) and coefficients (d_i and e_i) can be denoted as

$$a_i = -\frac{d_i}{i^2},\quad b_i = -\frac{e_i}{i^2} \tag{4}$$

Consequently, the profile P can be denoted as a Fourier series by using an inverse Fourier transform.

The characteristics of the algorithm can be estimated from its transfer function, which defines the relationship between the angle difference c and the profile data P.

Some simulation examples demonstrate how to calculate the roundness by using Fourier transform.[21] The simulation results also imply that the MBAS can measure roundness with repeatability under 10 nm if the random angle error is less than 0.8 μrad.

4. Pre-Experiment

4.1 Configuration of the pre-experiment

The pre-experimental arrangement is shown in Fig. 7. It consists of the MBAS (multi-autocollimator system with a microlens), two XY-platforms, a rotary platform, a tilt stage, and a support structure. We used a stage controller to move the rotary platform, controlled by Labview software on a PC, and recorded the MBAS output signals at each position.

Fig. 8 shows the constructed MBAS. A 650-nm-wavelength laser beam from a LD passes through a pinhole of diameter 400 μm and is collimated by the collimator lens. The beam is then reflected by a beam splitter and projected onto the workpiece surface. The reflected beam from the workpiece surface passes totally through the beam splitter and focuses it on the microlens, which divides the beams into several

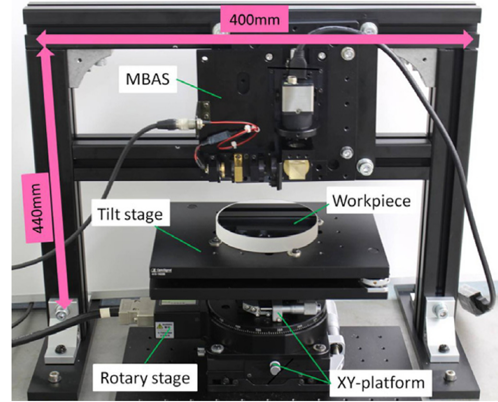

Fig. 7 Microscale flatness measurement setup, consisting of the MBAS, two XY platforms, a rotary platform, a tilt stage, and a supporting structure for the MBAS

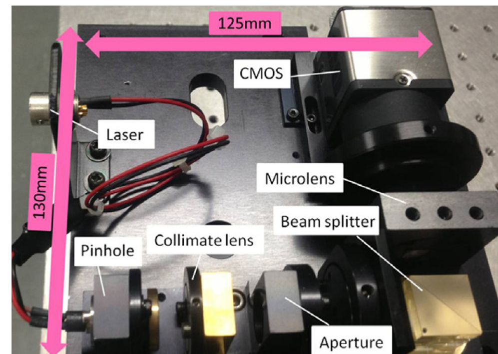

Fig. 8 Construction of the multi beam angle sensor: the MBAS is based on a multi-autocollimator system using a microlens

Table 1 Multi-beam angle sensor specifications (Fig. 8)

Laser Diode	Output power : 35 mW (CW) Wavelength : 658 nm
Pinhole	Diameter : 400 μm
Aperture	Diameter : 4 mm
Microlens	Focal distance : 46.7 mm (f) Pitch of the array : 500 μm
CMOS	Size : 5.6 mm × 4.2 mm Pixel size : 2.2 μm × 2.2 μm

beams. Finally, the CMOS tracks the position of 8¥8 focal spots. The pitch of the microlens is 500 μm.

The resulting pattern is observed and recorded by the CMOS camera, oriented vertically. Table 1 lists the device specifications. The angle difference can be calculated from the intensity distribution.[21]

4.2 MBAS stability

To verify the standard deviation of the MBAS measurements taken in a real environment, we measured the stability of the angles and the angle difference over two hours. Fig. 9 plots the angle measurements at points A and B, while the workpiece was not rotating. MBAS stability is then expressed as the standard deviation of the autocollimator output.

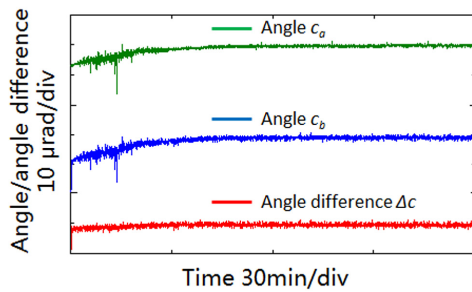

Fig. 9 MBAS stability: the angles and the angle difference were measured over two hours

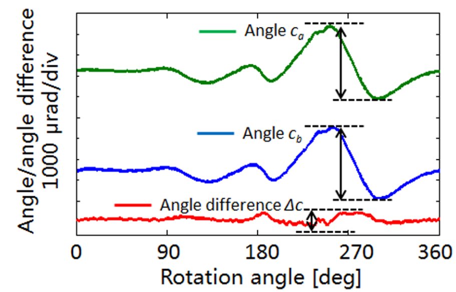

Fig. 10 Measured angles at points A and B and angle difference data for a PVC plate

Table 2 Experimental conditions

Parameters	Values
Radius of measurement	10 mm
Sample points	360
Rotation increment	1 degree

The experimental setup is mounted on a table in a basement. In Fig. 9, the long measurement time reveals a large thermal drift. The standard deviation for ca is 2.45 µrad, but that of c is 0.79 µrad. Here, the standard deviation c is the stability of the MBAS. We note that the fluctuation in the stability of c is small because it eliminates thermal drift. We therefore only consider the differential output to measure flatness.

Our stability testing demonstrates that a simple optical-path design makes the setup insensitive to environmental fluctuations.

4.3 Pre-experiment results

Mirrors were used as specimens in the experiment. Table 2 shows the experimental conditions. The workpiece is polyvinyl chloride (PVC) mirror coated with aluminum. The flatness of the coated PVC plate is of the order of several dozen micrometers.

Fig. 10 plots c_a, c_b, and c for the PVC plate, measured by the MBAS system, as functions of the rotation angle. The range of angle and angle difference of the rotation angle over 360 degree for the specimen are 3550 and 390 µrad, respectively. Measurements plotted in Fig. 11(a) show that the average flatness, measured over five trials, was 54.32 µm with average standard deviation of 52 nm (Fig. 11(b)).

To evaluate the MBAS method using real datasets, an experiment was developed using conventional high-precision machines (MITUTOYO FALCIO707) to measure the same PVC plate. Its flatness profile is plotted in Fig. 12 and has a flatness of 56.4 µm. Here, the indication accuracy of the MITUTOYO FALCIO707 is (1.9+4L/1000) µm, L is the measuring length (mm).

Fig. 12 shows the profile of the same workpiece obtained by two separate measurement methods. The flatness derived by the MBAS method and CMM are 54.32 and 56.4 µm, respectively. The MBAS measurement was done without any temperature control or vibration isolation.

From the results, it can be clearly seen that the MBAS measuring results follow the CMM very well in the whole. However, there is a slight difference in the measurements especially in some point elements (e.g. peaks, pits, saddle points) compared the two measuring results for

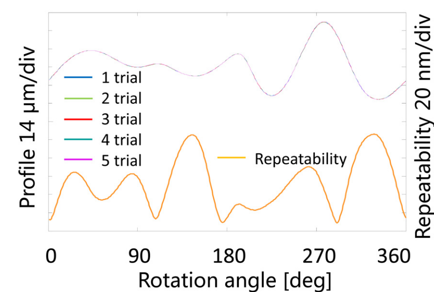

Fig. 11 Profile data (five trials) and repeatability (average standard deviation of five trials) test for a PVC plate measured with the MBAS

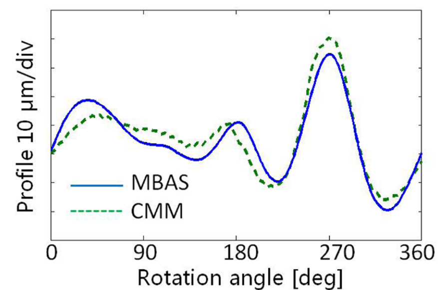

Fig. 12 Comparison of MBAS with CMM measurements

the following reasons: (1) the accuracy of the CMM is over 1.9 µm for limited range; (2) although we have measure the same PVC plate, the measuring position is not exactly same; and (3) MBAS is an optical instrument for non-contact measurement of angles, however, the CMM is using the contact sensor for measurement. Therefore, the measuring spot of the MBAS is larger than CMM.

To confirm the repeatability of the MBAS measurements, we repeated the experiment using a very flat mirror, with a flatness of several dozen nanometers.

Fig. 13 plots c_a and c_b for this mirror. The range of angle and angle difference of the rotation angle over 360 degree for the specimen are now 13.02 and 1.57 µrad, respectively. Profile data of the mirror are 76 nm with an average standard deviation 12 nm over four trials (Fig. 14).

The pre-experiment results (Table 3) confirm the suitability of the MBAS for measuring flatness. Future work will be necessary to

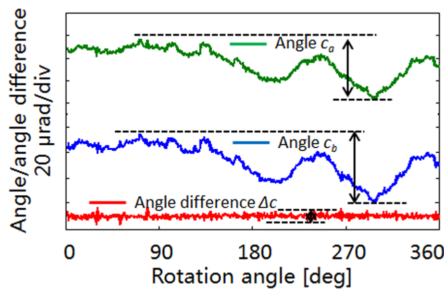

Fig. 13 Measured angles at points A and B, and the angle difference for the mirror

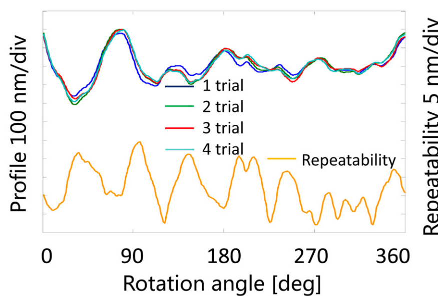

Fig. 14 MBAS profile data (four trials) and repeatability (standard deviation of four trials) test for the mirror

Table 3 Experimental results

Parameters	Plastic	Mirror
Flatness	54.32 μm	76 nm
Average STD	52 nm	12 nm

analyze the factors that influence the measurement accuracy and to find ways to assess and calibrate the MBAS.

5. Conclusions

We presented a new accurate microscale flatness-measuring machine (micro-FMM). This method uses only one probe, named the MBAS, to realize the precision flatness measurements. We verified that the MBAS can eliminate zero-difference error by circumferential scan and automatically eliminates the tilt error caused by the rotation of the workpiece when detecting angles. The MBAS can maintain high sensitivity with miniaturized size.

An MBAS system for measuring flatness was constructed. The optical probe is based on the principle of an autocollimator and has a stability of 0.79 μrad (the standard deviation of the angle difference).

The performance of the probe was confirmed experimentally. The flatness of a coated PVC plate was assessed by both the MBAS and CMM techniques, yielding 54.32 μm and 56.4 μm, respectively. Owing to the accuracy of the CMM, the discrepancy between the two techniques was 2.08 μm. Experimental results confirm the suitability of the MBAS for measuring flatness. To verify its repeatability, another experiment was done using a very flat mirror. This yielded a flatness of 76 nm with average standard deviation 12 nm, which hence verified the repeatability of the flatness measurements by MBAS.

A new experiment has been designed, which is planned to perform flatness measurement and analyze flatness measurement uncertainties. Although the repeatability of the MBAS is good enough, the flatness measurement and calibration the sensitivity of the MBAS will also be the future plan to execute.

ACKNOWLEDGEMENT

This research work was supported by the JSPS KAKENHI Grant number 26249006 and the program of China Scholarships Council (CSC).

REFERENCES

1. ISO 1101, “Geometrical Product Specifications (GPS) - Geometrical Tolerancing - Tolerances of Form, Orientation, Location and Run-Out,” 2012.

2. ISO 17450, “Geometrical Product Specifications (GPS) - General Concepts - Part 1: Model for Geometrical Specification and Verification,” 2011.

3. Whitehouse, D. J., “Handbook of Surface Metrology,” CRC Press, 1994.

4. Huang, M. F., Wang, Q. Y., Zhong, Y. R., Kuang, B., and Li, X. Q., “On the Flatness Uncertainty Estimation based on Data Elimination,” Applied Mechanics and Materials, Vols. 16-19, pp. 347-351, 2009.

5. Cui, C., Fu, S., and Huang, F., “Research on the Uncertainties from Different Form Error Evaluation Methods by Cmm Sampling,” The International Journal of Advanced Manufacturing Technology, Vol. 43, No. 1-2, pp. 136-145, 2009.

6. Choi, W. and Kurfess, T. R., “Uncertainty of Extreme Fit Evaluation for Three-Dimensional Measurement Data Analysis,” Computer-Aided Design, Vol. 30, No. 7, pp. 549-557, 1998.

7. Bachmann, J., marc Linares, J., Sprauel, J. M., and Bourdet, P., “Aide in Decision-Making: Contribution to Uncertainties in Three-Dimensional Measurement,” Precision Engineering, Vol. 28, No. 1, pp. 78-88, 2004.

8. Kolivand, H. and Sunar, M. S., “An Overview on Base Real-Time Shadow Techniques in Virtual Environments,” TELKOMNIKA (Telecommunication Computing Electronics and Control), Vol. 10, No. 1, pp. 171-178, 2012.

9. Kiyono, S., Asakawa, Y., Inamoto, M., and Kamada, O., “A Differential Laser Autocollimation Probe for On-Machine Measurement,” Precision Engineering, Vol. 15, No. 2, pp. 68-76, 1993.

10. Bünnagel, R., Oehring, H.-A., and Steiner, K., “Fizeau

Interferometer for Measuring the Flatness of Optical Surfaces," Applied Optics, Vol. 7, No. 2, pp. 331-335, 1968.

11. Hariharan, P., "Interferometric Testing of Optical Surfaces: Absolute Measurements of Flatness," Optical Engineering, Vol. 36, No. 9, pp. 2478-2481, 1997.

12. Kim, W. J., Shimizu, Y., Kimura, A., and Gao, W., "Fast Evaluation of Period Deviation and Flatness of a Linear Scale by using a Fizeau Interferometer," Int. J. Precis. Eng. Manuf., Vol. 13, No. 9, pp. 1517-1524, 2012.

13. Yokoyama, T., Yokoyama, S., Yoshimori, K., and Araki, T., "Sub-Nanometre Double Shearing Heterodyne Interferometry for Profiling Large Scale Planar Surfaces," Measurement Science and Technology, Vol. 15, No. 12, pp. 2435-2443, 2004.

14. Yoder, P., Schlesinger, E. R., and Chickvary, J., "Active Annular-Beam Laser Autocollimator System," Applied Optics, Vol. 14, No. 8, pp. 1890-1895, 1975.

15. Ennos, A. and Virdee, M., "High Accuracy Profile Measurement of Quasi-Conical Mirror Surfaces by Laser Autocollimation," Precision Engineering, Vol. 4, No. 1, pp. 5-8, 1982.

16. Schuda, F. J., "High-Precision, Wide-Range, Dual-Axis, Angle Monitoring System," Review of Scientific Instruments, Vol. 54, No. 12, pp. 1648-1652, 1983.

17. Luther, G. G., Deslattes, R. D., and Towler, W. R., "Single Axis Photoelectronic Autocollimator," Review of Scientific Instruments, Vol. 55, No. 5, pp. 747-750, 1984.

18. Gao, W., Yokoyama, J., Kojima, H., and Kiyono, S., "Precision Measurement of Cylinder Straightness using a Scanning Multi-Probe System," Precision Engineering, Vol. 26, No. 3, pp. 279-288, 2002.

19. Fujimoto, I., Nishimura, K., Takatsuji, T., and Pyun, Y.-S., "A Technique to Measure the Flatness of Next-Generation 450mm Wafers using a Three-Point Method with an Autonomous Calibration Function," Precision Engineering, Vol. 36, No. 2, pp. 270-280, 2012.

20. Fujimoto, I., Takatsuji, T., Nishimura, K., and Pyun, Y.-S., "An Uncertainty Analysis of Displacement Sensors with the Three-Point Method," Measurement Science and Technology, Vol. 23, No. 11, Paper No. 115102, 2012.

21. Chen, M., Takahashi, S., and Takamasu, K., "Development of High-Precision Micro-Roundness Measuring Machine using a High-Sensitivity and Compact Multi-Beam Angle Sensor," Precision Engineering, Vol. 42, pp. 276-282, 2015.

IOPscience iopscience.iop.org

Home Search Collections Journals About Contact us My IOPscience

Non-contact precision profile measurement to rough-surface objects with optical frequency combs

This content has been downloaded from IOPscience. Please scroll down to see the full text.

2016 Meas. Sci. Technol. 27 124002

(http://iopscience.iop.org/0957-0233/27/12/124002)

View the table of contents for this issue, or go to the journal homepage for more

Download details:

IP Address: 133.11.77.52
This content was downloaded on 16/05/2017 at 08:51

Please note that terms and conditions apply.

You may also be interested in:

Absolute distance measurement system using a fs laser as a modulator
Nicolae R Doloca, Karl Meiners-Hagen, Martin Wedde et al.

Absolute Measurement of Baselines up to 403 m Using Heterodyne Temporal Coherence Interferometer with Optical Frequency Comb
Hirokazu Matsumoto, Xiaonan Wang, Kiyoshi Takamasu et al.

Absolute distance measurement by dual-comb interferometry with multi-channel digital lock-in phase detection
Ruitao Yang, Florian Pollinger, Karl Meiners-Hagen et al.

Measurement of optical frequencies and frequency ratios
Harald Schnatz

High-accuracy correction of air refractive index by using two-color heterodyne interferometry of optical frequency combs
Guanhao Wu, Kaoru Arai, Mayumi Takahashi et al.

Development of a prototype compact fibre frequency synthesiser for mobile femtosecond optical clocks
V S Pivtsov, B N Nyushkov, I I Korel' et al.

brightrecruits WEBINAR

Studentship opportunities with the UK's
National Quantum Technology Hubs

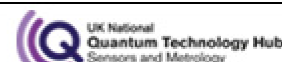

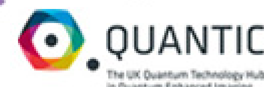

IOP Publishing

Measurement Science and Technology

Meas. Sci. Technol. **27** (2016) 124002 (7pp)

doi:10.1088/0957-0233/27/12/124002

Non-contact precision profile measurement to rough-surface objects with optical frequency combs

Taro Onoe, Satoru Takahashi, Kiyoshi Takamasu and Hirokazu Matsumoto

The University of Tokyo, Hongo 7-3-1, Bunkyo-ku, Tokyo, 113-8656, Japan

E-mail: onoe@nanolab.t.u-tokyo.ac.jp, takahashi@nanolab.t.u-tokyo.ac.jp, takamasu@pe.t.u-tokyo.ac.jp and hi.matsumoto@nanolab.t.u-tokyo.ac.jp

Received 31 December 2015, revised 24 June 2016
Accepted for publication 29 July 2016
Published 14 October 2016

Abstract

In this research, we developed a new method for the high precision and contactless profile measurement of rough-surfaced objects using optical frequency combs. The uncertainty of the frequency beats of an optical frequency comb is very small (relative uncertainty is 10^{-10} in our laboratory). In addition, the wavelengths corresponding to these frequency beats are long enough to measure rough-surfaced objects. We can conduct high-precision measurement because several GHz frequency beats can be used if the capability of the detector permits. Moreover, two optical frequency combs with Rb-stabilized repetition frequencies are used for the measurement instead of an RF frequency oscillator; thus, we can avoid the cyclic error caused by the RF frequency oscillator. We measured the profile of a wood cylinder with a rough surface (diameter is approximately 113.2 mm) and compared the result with that of coordinate measuring machine (CMM).

Keywords: profile measurement, optical frequency comb, non-contact measurement, rough surface measurement

(Some figures may appear in colour only in the online journal)

1. Introduction

Machining accuracy is ensured by measurement accuracy, thus high-precision measurement method is necessary for improvement of manufacturing. Since 2009, optical frequency combs have become the national standard for the measurement of length in Japan because of its high precision interval of pulses (relative uncertainty is 10^{-14}). Until now, many measurement methods with optical frequency combs such as interferometer are realized. One of them is realized by changing the optical path length with linear stage [1] and another interferometer is realized by shifting the repetition frequency of optical frequency comb [1–3]. Two wavelength interferometer stabilized with optical frequency comb is also used [4, 5]. Time of flight is also applied with optical frequency comb [6]. The beat signals are obtained when the beam of the optical frequency comb is detected. This kind of signal is also used for measurement [7–10].

Recently, a high-precision non-contact measurement method for rough surface objects became more important in factories. For example, in factories which produce airplanes, we usually measure the whole surface of airplanes with a large CMM. However, it takes a long time to measure whole surface. Thus, a non-contact measurement method to rough surface is necessary to decrease the time cost of the measurement. The aim of this research is to develop a non-contact precision absolute measurement system that can also measure the profile of rough-surfaced objects without cyclic error.

So far, many kinds of distance measurement methods for this purpose have been invented in previous investigations. Fujima's group invented a distance measurement system with He–Ne laser modulated by 28 GHz and the standard deviation was 1 μm [11]. However, this measurement system needs correction of the cyclic error to the measured distance. An ordinary electronic distance meter also has cyclic error [12]. Minoshima's group developed a distance measurement

 © 2016 IOP Publishing Ltd Printed in the UK

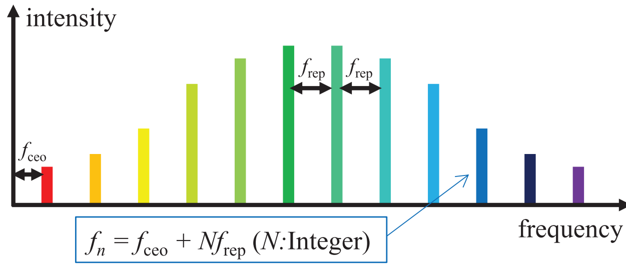

Figure 1. Spectrum of optical frequency comb. The interval of each frequency is called repetition frequency.

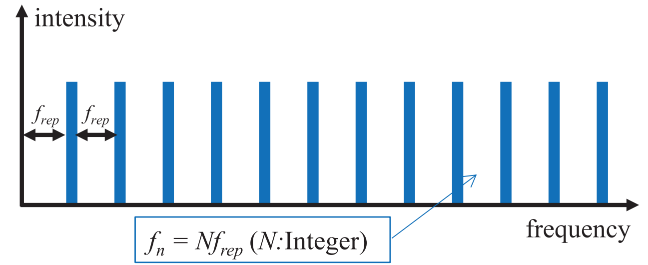

Figure 2. Spectrum of self-beat signals which are obtained when the beam is detected.

system with frequency beats of the optical frequency comb and the measured distance was up to 240 m [7]. The relative uncertainty was about 8 ppm. In this system, the frequency used for measurement was 1 GHz and the component of the measurement system was made to be simple. Thus, in this measurement system, no cyclic error was observed. In our past research, we used an optical frequency comb and RF oscillator to apply frequency beats of higher frequencies than 1 GHz. However, cyclic error was observed because of using the RF oscillator. Thus, we used the beat signals of two optical frequency combs instead of using the signal of RF oscillator [13]. However, the measurement accuracy is poor because of the use of the signal of frequency synthesizer as the reference signal directly. In this paper, optical frequency combs and AOM are used to improve the signal processing, and we utilize the characteristics of the optical frequency combs to achieve our objective, and we explain the principle of the proposed measurement system with optical frequency combs and an experiment of measuring the profile of a cylinder with a rough surface (Ra > 10 μm).

2. Measurement principle with an optical frequency comb

An optical frequency comb is a pulse laser, and the relative uncertainty of the pulse interval is very small (the relative uncertainty of the comb used in our lab is 10^{-10}). Because the pulse envelop is periodic, many frequency modes are observed in the frequency domain. The frequency difference between each mode corresponds to the pulse interval. This frequency difference is called the repetition frequency (f_{rep}). In our lab, the relative uncertainty of the repetition frequency is also 10^{-10}. The frequency of nth mode signal is represented as $f_{ceo} + nf_{rep}$ (figure 1). f_{ceo} is called carrier envelop offset whose relative uncertainty is the same as the frequency of laser diode. When a beam of an optical frequency comb is detected by a detector, the beat signals between each frequency are obtained. Thus, the frequency of the detected signal is represented as Nf_{rep} where N is an integer (figure 2). The frequencies of these signals are in the range of several tens of GHz and are limited by the detector. Hereafter, we refer these signals as self-beat signals.

In the time domain, the electrical field of the beam of an optical frequency comb $e(t)$ is represented as

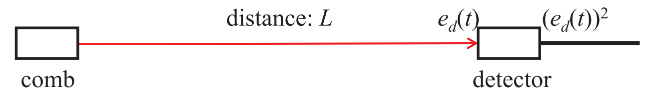

Figure 3. Beam from the comb enters the detector. L is the distance and $e_d(t)$ represents the electrical field of the incident beam.

$$e(t) = \sum_i \cos(2\pi f_i t + \theta_i) \qquad \theta_i - \theta_{i-1} = \text{const} \tag{1}$$

Here, f_i and θ_i are the frequency and the phase of the ith mode signal, respectively and n is refractive index. In figure 3, the beam from the comb enters the detector. The distance between the comb and the detector is L. The detected beam $e_d(t)$ is represented as

$$e_d(t) = \sum_i \cos\left(2\pi f_i t + \theta_i + \frac{2\pi f_i nL}{c}\right) \tag{2}$$

Here, c is the velocity of light. The detected signal is represented as $(e_d(t))^2$. Thus, the jth mode of a self-beat signal ($s_j(t)$) is represented as

$$s_j(t) = \sum_i \frac{1}{2} \sin\left(2\pi(f_{i+j} - f_i)t + \theta_{i+j} - \theta_i + \frac{2\pi(f_{i+j} - f_i)nL}{c}\right) \tag{3}$$

In the proposed method, the phases of the self-beat signals are used for distance measurement. If the optical path length to the detector is changed by ΔL, the phase change of the jth mode of the self-beat signal ($\Delta\varphi_j$) can be represented by

$$\Delta\varphi_j = \frac{2\pi(f_{i+j} - f_i)n\Delta L}{c} = \frac{2\pi j f_{rep} n\Delta L}{c} \tag{4}$$

Thus, if $\Delta\varphi_j$ is measured, the change in the optical path length ΔL can be calculated.

$$\Delta L = \frac{c\Delta\varphi_j}{2\pi j f_{rep} n} + \frac{mc}{j f_{rep} n} \tag{5}$$

Here, m is an integer. The wavelengths of the self-beat signals range from several tens of millimeters up to several meters. Thus, we can measure rough-surfaced objects because the wavelength is longer than the roughness. In equation (5), if ΔL is longer than the wavelength, m is not zero and is determined using a coincidence method with some other frequencies of the self-beat signals.

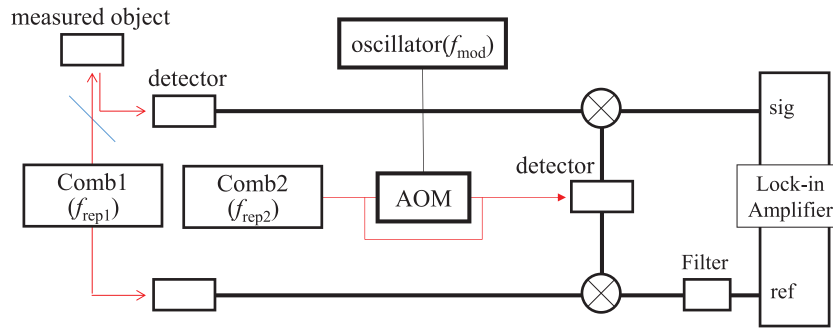

Figure 4. Signal processing of the proposed measurement system. We compare the phase of the beam from the measured object with that of the reference beam by using a lock-in amplifier (0.5 Hz–200 kHz, 5610B, NF-corporation).

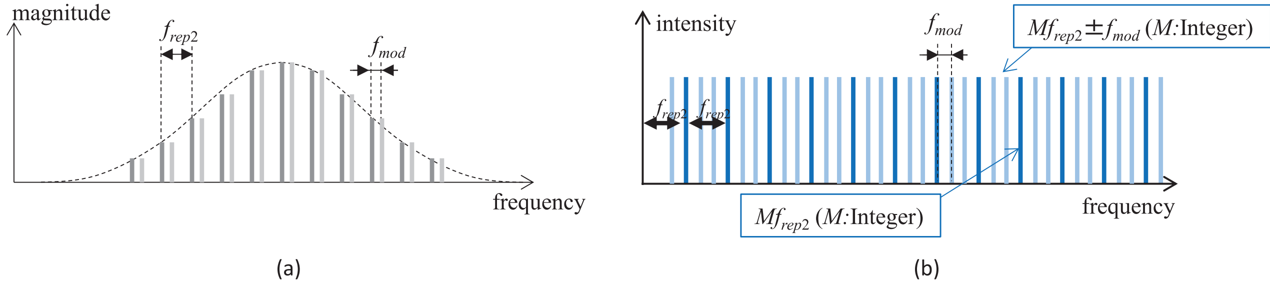

Figure 5. Frequency of the beam which goes through the AOM is shifted by f_{mod} and the spectrum of the beam at the detector is as the left side of the figure (a). Thus, the frequencies of detected self-beat signals are shifted by $\pm f_{mod}$ (b).

3. Measurement of the phase change of self-beat signals

If the frequency of the self-beat signal is very low, it is easy to detect the change in phase. However, the frequencies of self-beat signals are high (radio frequency (RF)). Hence, we cannot use a phase comparator and lock-in amplifier, and the detection of the phase change becomes difficult.

In the proposed measurement system, we used two optical frequency combs (f_{rep1} is 100 MHz and f_{rep2} is 58.417 MHz), an acoustic optical modulator (AOM (30–70 MHz)), and a frequency mixer are used to reduce the frequency without a phase change. The signal processing of the proposed measurement system is shown in figure 4. The beam of comb2 is split before the AOM. One of the beams goes through the AOM and the other doesn't pass the AOM. These two beams are gathered and go into the detector. The detected self-beat signal of comb2 in frequency domain is shown in figure 5. The frequency of the beam which goes through the AOM is shifted by f_{mod}. Thus, the frequencies of detected self-beat signals are shifted by $\pm f_{mod}$.

In order to obtain the phase change, we compare the phase of the beam from the measured object with that of the reference beam by using a lock-in amplifier (0.5 Hz–200 kHz, 5610B, NF-corporation). In addition, we use a frequency mixer to minimize the frequency without a phase change. Moreover, we have to remove the unnecessary signals, which are obtained after mixing. In order to do that, we used an AOM for changing the frequency of the self-beat signal by $\pm f_{mod}$, and the frequency of the signal after mixing is set to a frequency which is same as that of the filter (10 kHz). Thus, only the necessary signals can be used. In the case of measurement with the frequency of 3.6 GHz, the modulate frequency is set to 36.553 MHz. In our research, we used the self-beat signals of another optical frequency comb instead of an RF oscillator and the modulate frequency is low (about 50 MHz) so that the phase noise of the signal from the oscillator does not cause cyclic error. Thus, we can decrease the effect of the cyclic error caused by the RF oscillator as reported in previous research.

4. Measurement uncertainty of the proposed measurement system

In figure 2, if the optical path length changes by ΔL and the detected phase changes by $\Delta\varphi$, the measured distance can be represented as follows.

$$\Delta L = \frac{mc}{fn} + \frac{c\Delta\varphi}{2\pi fn} \tag{6}$$

Here, m is an integer, c is the speed of light, f is the frequency of the ith mode self-beat signal, and n is the refractive index of air. The measurement uncertainty of the proposed measurement system is represented as follows.

$$\sigma_{\Delta L} = \sqrt{\left(\frac{c}{nf}\right)^2\left(\frac{\sigma_{\Delta\varphi}}{2\pi}\right)^2 + \Delta L^2\left(\frac{\sigma_f}{f}\right)^2 + \Delta L^2\left(\frac{\sigma_n}{n}\right)^2} \tag{7}$$

Here, $\sigma_{\Delta L}$ is the uncertainty of ΔL, $\sigma_{\Delta\varphi}$ is the uncertainty of $\Delta\varphi$, σ_f is the uncertainty of f, and σ_n is the uncertainty of n. The relative uncertainty of f is the same as the repetition frequency of the optical frequency comb, which is approximately 10^{-10} in this research, and the relative uncertainty of n is approximately 10^{-6} for a 1 °C change in temperature. ΔL is about several meters to several tens of meters. Thus, the

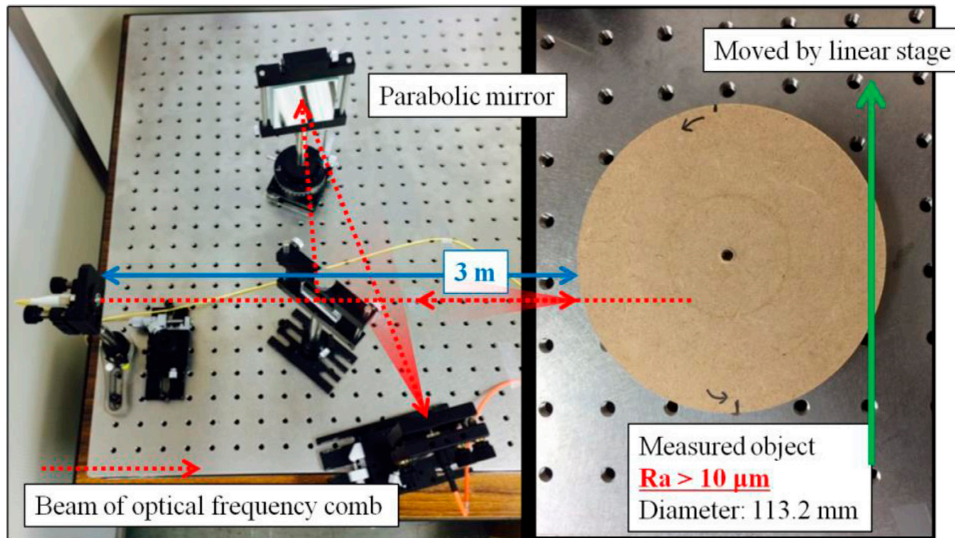

Figure 6. Setup of the proposed measurement system. The size of the cylinder is 113.2 mm, and it is moved by 120 mm. Surface profile is measured by a change in the optical path length.

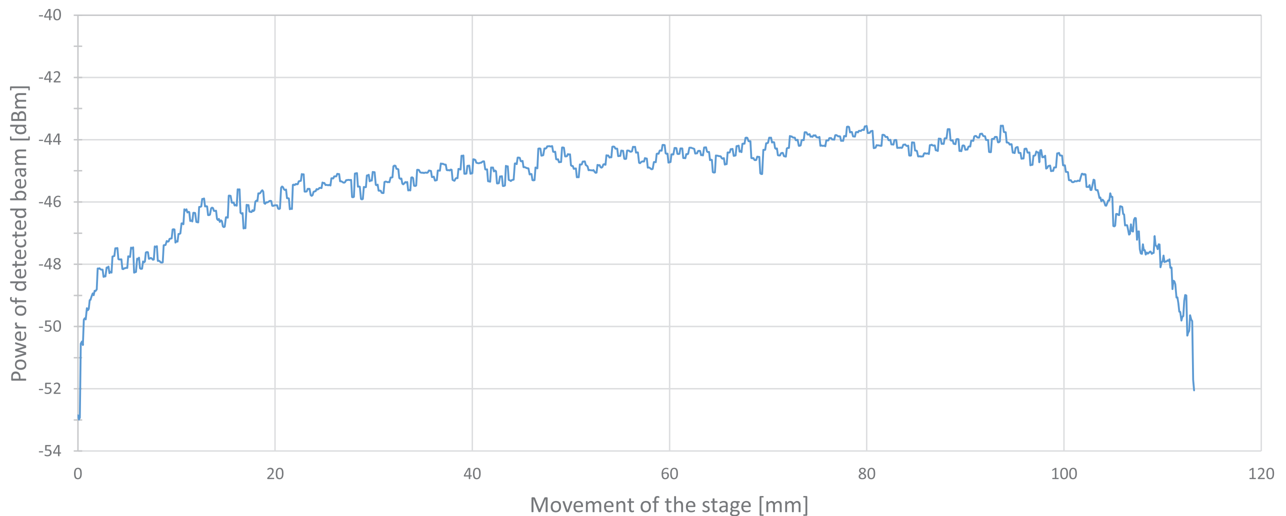

Figure 7. Power of the detected beam from measured object. In a wide range, the power is lower than −44 dBm (approximately 30 nW).

uncertainty of f and n does not have much effect on $\sigma_{\Delta L}$ if the measurement distance and the time of measurement are short. In this case, $\sigma_{\Delta L}$ is represented as

$$\sigma_{\Delta l} = \frac{c}{nf}\left(\frac{\sigma_{\Delta\varphi}}{2\pi}\right) \quad (8)$$

Thus, the uncertainty of the measurement is obtained by f and $\sigma_{\Delta\varphi}$. $\sigma_{\Delta\varphi}$ depends on the quality of the detected signal. $\sigma_{\Delta\varphi}$ is represented as follows.

$$\sigma_{\Delta\varphi} = \frac{kv_{\rm n}}{v_{\rm s}} \quad (9)$$

Here, k is a constant value of the measurement system determined by the equipment used in our system, $v_{\rm n}$ is the amplitude of noise in our measurement system, and $v_{\rm s}$ is the amplitude of the signal used to measurement. Thus, this value k does not change if the equipment used in the research is the same. Also, the main source of $v_{\rm n}$ is thermal noise in the circuit. If the temperature (300 K) is changed by 1 °C, the amplitude of $v_{\rm n}$ is changed by 0.3%. Thus, measurement uncertainty can be calculated with the amplitude of the signal if $kv_{\rm n}$ is already known. $kv_{\rm n}$ can be calculated with value of $\sigma_{\Delta\varphi}$ and $v_{\rm s}$ which are experimentally obtained by a lock-in amplifier.

5. Measurement of the cylinder with a rough surface

As we explained, the wavelength of the self-beat signals of an optical frequency comb is longer than the roughness of the surface. Thus, the profile of rough-surfaced objects can be measured. In this paper, we measured a cylinder which has a rough surface (Ra > 10 μm). The experimental system is shown in figure 6. The beam of the optical frequency comb comes from the collimator and hits on the measured surface. The reflected beam is concentrated by a parabolic mirror. The measured cylinder is placed on the linear stage and is moved

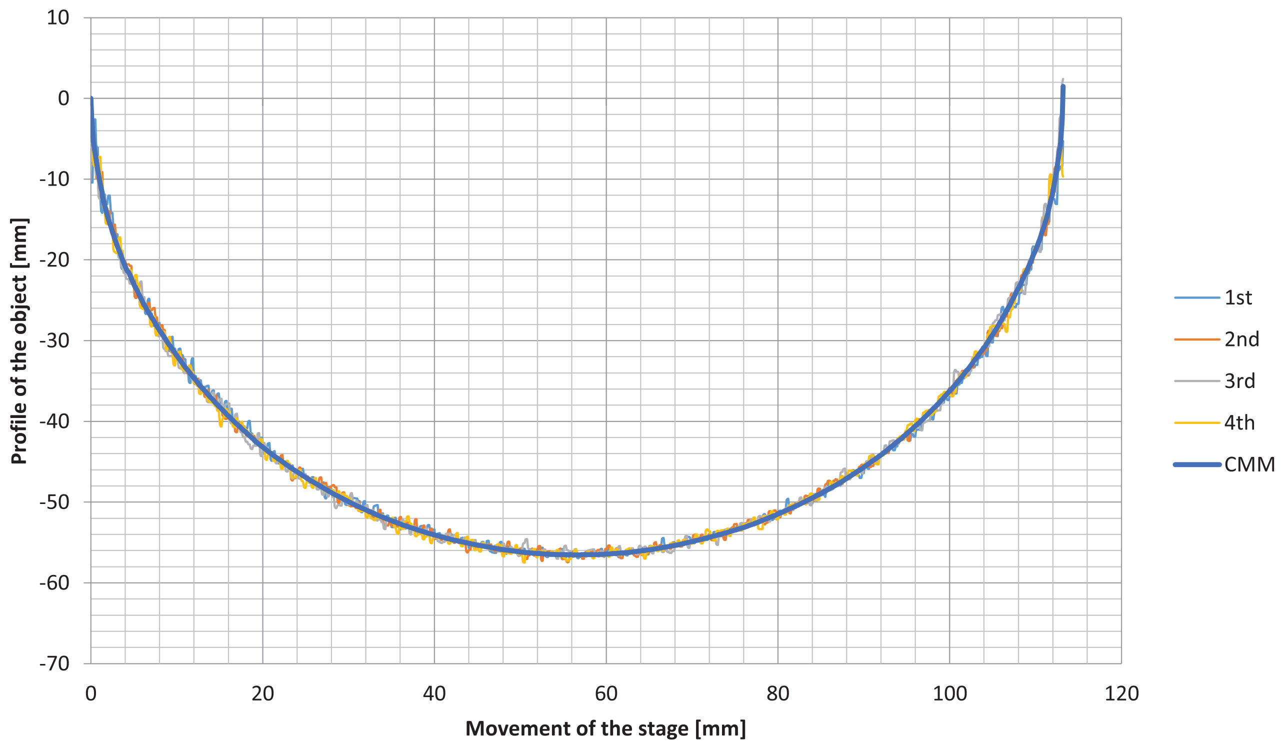

Figure 8. Profile of the measured object. The profile can be measured from one side to the other side. The result of the proposed system and that of the CMM is almost the same.

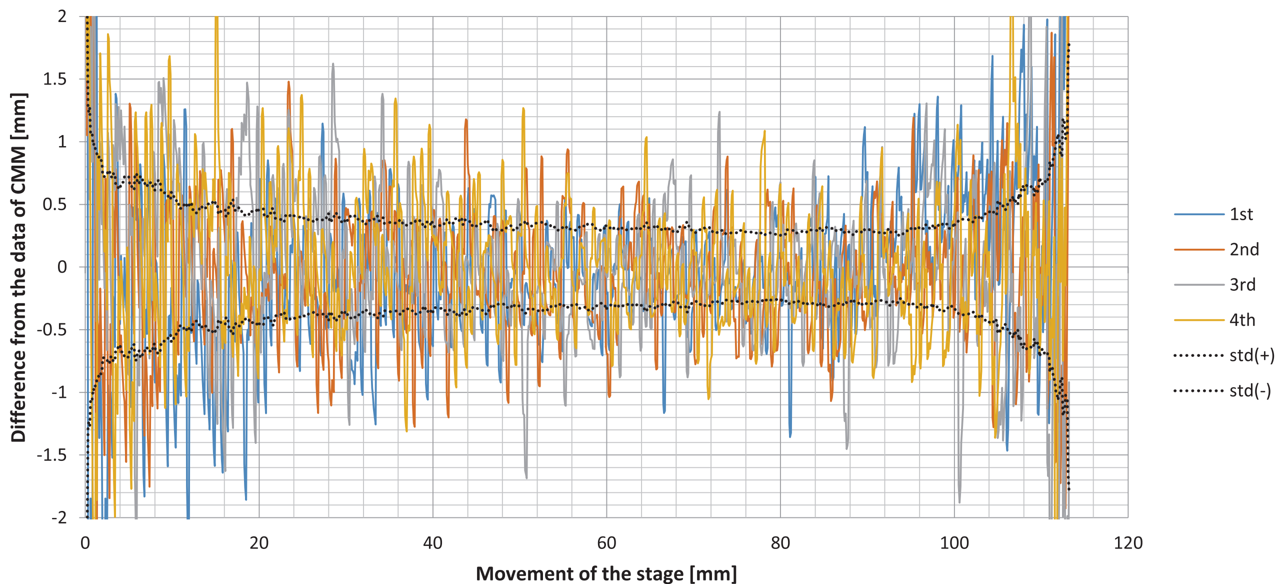

Figure 9. Difference between the result of the proposed measurement system and that of the CMM. The black dotted line represents the uncertainty predicted using (8) and (9). In a wide range, the measurement uncertainty is approximately 400 μm.

by 120 mm. As the measured cylinder moves, the optical path length to the measured surface changes. Thus, the profile of the cylinder can be measured by measuring the change in the optical path length. Even if the phase difference exceeds 2π, phase-unwrapping process can be applied because the measured surface is continuous. The experimental conditions are as following. The experimental conditions are as following. The distance from the collimator to the rough surface is approximately 3 m. The frequency of the self-beat signal is 3.6 GHz (wavelength is 83.275 68 mm). The time constant of the lock-in amplifier is 100 ms. We measure the profile of the surface four times. The power of the detected beam is shown in figure 7. The experimental results are shown in figures 8 and 9. We measure the profile of the surface four times. The profile is laso measured with a CMM (uncertainty is 2 μm).

As shown in figure 7, the power of the detected beam is lower than −44 dBm in a wide range. However, we could measure the surface from one side to the other side (figure 8). The measurement result obtained by using the proposed system is almost the same as that of the CMM, and the standard

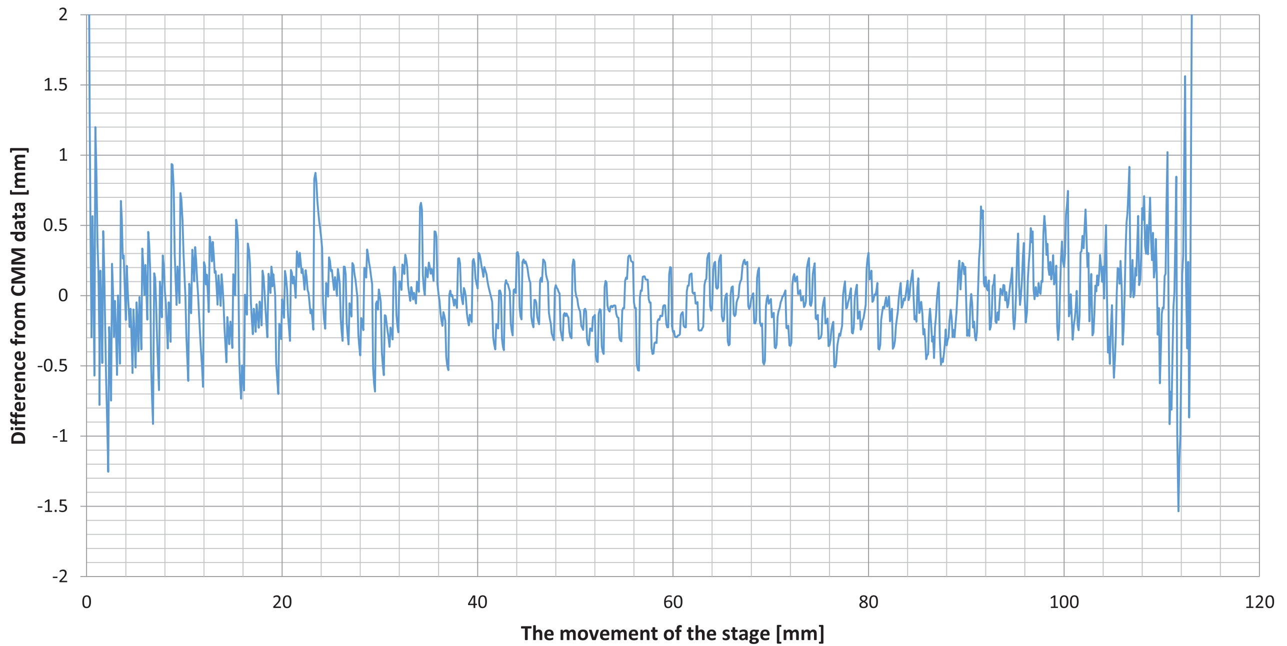

Figure 10. Difference between the averages of four measurement results obtained by the proposed measurement system and that of the CMM. In a wide range, the measurement uncertainty approximately 200 μm.

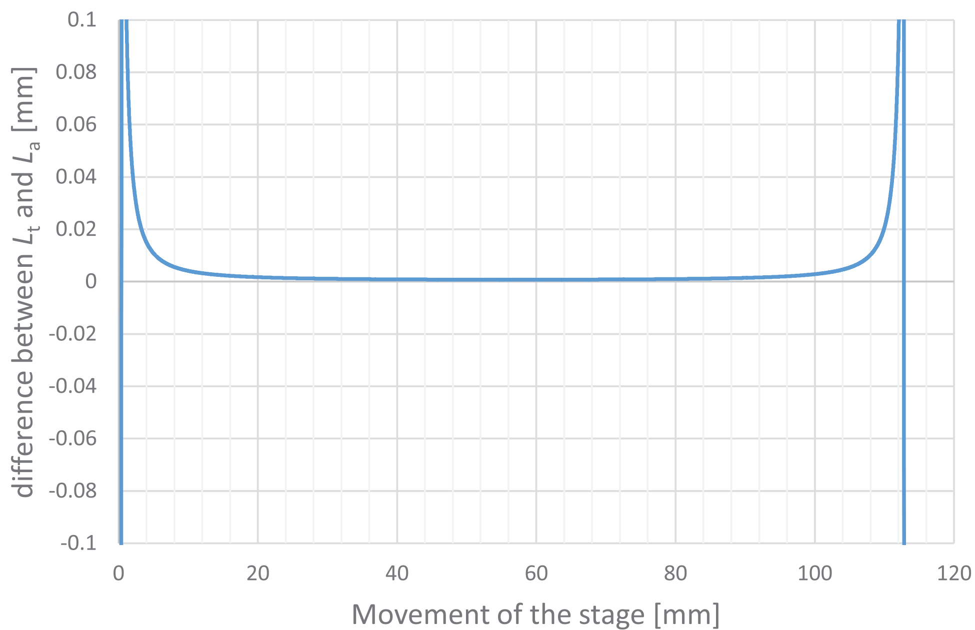

Figure 11. We have simulated the difference of the measurement with beam diameter of 1 mm (L_a) and with that of infinitesimal (L_t). In wide range, the difference from actual value (L_t) is smaller than 0.02 mm.

deviation of the difference is approximately 0.4 mm in a wide range (figure 9). The uncertainty in the measurement is due to the weak power of the reflected beam (< -44 dBm) which is scattered by rough surface. Thus, in order to improve the accuracy of the measurement, we need to increase the power of the detected signal or improve the signal processing. As shown in figure 9, almost all the errors are random errors. If we use the average of the four data, the difference between the result of the proposed method and that of the CMM becomes smaller (figure 10).

6. Discussion

In our experiment, we measured the curved surface and beam diameter is about 1 mm on the measured surface. Thus, the result of the measurement is the average distance on the beam spot. We have simulated the difference of the measurement with beam diameter of 1 mm (L_a) and with that of infinitesimal (L_t) as shown in figure 11. The diameter of measured cylinder is set to 113.2 mm. At the side of the measured object, the difference from actual value (L_t) is larger than 0.02 mm.

However, in wide range, the difference from actual value (L_t) is smaller than 0.02 mm. Thus, in our measurement of the cylinder with the diameter of 113.2 mm, the beam diameter has not much effect in wide range of the cylinder.

In the research done by Minoshima's group, just up to 1 GHz signal can be used because mixing to decrease the frequency of signal is not applied [7]. In our method, many self-beat signals can be used because the frequency of each signal is decreased by mixing (less than 30 MHz). If we process more of the self-beat signals simultaneously, the measurement uncertainty becomes much better. For example, we have simulated using 25 signals simultaneously and the measurement uncertainty will be about 40 μm to the rough surface of Ra $>$ 10 μm. Also, absolute measurement can be conducted with this method.

7. Summary

In this paper, we explained the measurement principle of optical frequency combs with the self-beat signals. The wavelengths corresponding to these self-beat signals are long enough to measure rough-surfaced objects. In addition, we can conduct high-precision measurements because several tens of GHz frequency beats can be used depending on the capability of the detector. Moreover, two optical frequency combs with Rb-stabilized repetition frequencies are used for the measurement instead of an RF frequency oscillator, thus, we can avoid the cyclic error caused by the RF frequency oscillator.

We measured the profile of a rough-surfaced cylinder four times, and we confirmed that the result of the proposed measurement system and that of the CMM is almost the same. The difference between the average data of the proposed system and that of the CMM is approximately 200 μm. However, the power of the beam reflected from the measured surface is very weak, and that becomes the main reason for uncertainty in the measurement. If we process all of the self-beat signals simultaneously, the measurement uncertainty becomes much better. For example, if we use 25 signals simultaneously, the measurement uncertainty will be about 40 μm to the rough surface of Ra $>$ 10 μm. Also, absolute measurement can be conducted with this method.

References

[1] Matsumoto H *et al* 2012 Absolute measurement of baselines up to 403 m using heterodynetemporal-coherence interferometer with optical frequency comb *Appl. Phys. Express* **5** 046601

[2] Joo W D *et al* 2013 Femtosecond laser pulses for fast 3D surface profilometry of microelectronic step-structures *Opt. Express* **21** 13

[3] Choi S *et al* 2012 Multi-gigahertz frequency comb based interferometry using frequency-variable supercontinuum generated by optical pulse synthesizer *Opt. Express* **20** 27820–9

[4] Schuhler N *et al* 2006 Frequency-comb-referenced twowavelength source for absolute distance measurement *Opt. Lett.* **31** 3101–3

[5] Hyun S *et al* 2010 Absolute distance measurement using the frequency comb of a femtosecond laser *Ann. CIRP* **59** 555–8

[6] Lee J *et al* 2010 Time-of-flight measurement with femtosecond light pulses *Nat. Photon.* **4** 716–20

[7] Minoshima K and Matsumoto H 2000 High-accuracy measurement of 240 m distance in an optical tunnel by use of a compact femtosecond laser *Appl. Opt.* **39** 5512–17

[8] Yokoyama S *et al* 2009 A distance meter using a terahertz intermode beat in an optical frequency comb *Opt. Express* **17** 17324–37

[9] Pham Q D *et al* 2013 Optical frequency comb interference profilometry using compressive sensing *Opt. Express* **21** 19003–11

[10] Yasui T *et al* 2014 Phase-slope and phase measurements of tunable CW-THz radiation with terahertz comb for wide-dynamic-range high-resolution distance measurement of optically rough object *Opt. Express* **22** 17349–59

[11] Fujima I *et al* 1998 High-resolution distance meter using optical intensity modulation at 28 GHz *Meas. Sci. Technol.* **9** 1049–52

[12] Rueger J 1990 *Electronic Distance Measurement* (Berlin: Springer)

[13] Onoe T *et al* 2012 Development of a non-contact precision measurement technique using optical frequency combs *Key Eng. Mater.* **523–4** 877–82